Rejuvenating aged osteoprogenitors for bone repair

Joshua Reeves[1,2], Pierre Tournier[1*], Pierre Becquart[1*], Robert Carton[2], Yin Tang[3,4], Alessandra Vigilante[2], Dong Fang[3,4] and Shukry J Habib[1]

[1]Department of Biomedical Sciences, University of Lausanne, Lausanne, Switzerland.
[2]Centre for Gene Therapy and Regenerative Medicine King's College London, London, UK.
[3]Zhejiang Provincial Key Laboratory for Cancer Molecular Cell Biology, Life Sciences Institute Zhejiang University, Hangzhou, Zhejiang 310058, China.
[4]Department of Ministry of Education, The Second Affiliated Hospital, Zhejiang University School of Medicine, Hangzhou, Zhejiang, China

* Contributed equally to this work.
Corresponding author: shukryjames.habib@unil.ch

Abstract

Aging is marked by a decline in tissue regeneration, posing significant challenges to an increasingly older population. Here, we investigate age-related impairments in calvarial bone healing and introduce a novel two-part rejuvenation strategy to restore youthful repair. We demonstrate that aging negatively impacts the calvarial bone structure and its osteogenic tissues, diminishing osteoprogenitor number and function and severely impairing bone formation. Notably, increasing osteogenic cell numbers locally fails to rescue repair in aged mice, identifying the presence of intrinsic cellular deficits. Our strategy combines Wnt-mediated osteoprogenitor expansion with intermittent fasting, which leads to a striking restoration of youthful levels of bone healing. We find that intermittent fasting improves osteoprogenitor function, benefits that can be recapitulated by modulating NAD+ dependent pathways or the gut microbiota, underscoring the multifaceted nature of this intervention. Mechanistically, we identify mitochondrial dysfunction as a key component in age-related decline in osteoprogenitor function and show that both cyclical nutrient deprivation and Nicotinamide mononucleotide rejuvenate mitochondrial health, enhancing osteogenesis. These findings offer a promising therapeutic avenue for restoring youthful bone repair in aged individuals, with potential implications for rejuvenating other tissues.

Introduction

Flat bones like the sternum, scapula, pelvic bones, and skull bones play crucial roles in the body, including protecting organs and anchoring muscles. Their thin structure makes them prone to fractures(Huelke and Compton, 1983), leading to pain, disability, and complications like internal bleeding or organ damage(Ren et al., 2020). As individuals age, flat bones become more brittle, increasing the risk of fractures(Beedham et al., 2019). Skull fractures, common in head injuries at any age(Carson, 2009), carry a higher mortality rate even when considering trauma severity(Tsai et al., 2022). Aging affects the shape and fragility of calvarial bones(Cotofana et al., 2018)(Torimitsu et al., 2014), but the impact on osteogenic tissues supporting bone repair, such as the calvarial periosteum and suture mesenchyme remains elusive.

In the calvaria, bones form and repair through intramembranous ossification(van den Bos et al., 2008). Osteoblasts which deposit pre-mineralized bone tissue(Bianco and Robey, 2015) arise from CD90$^+$ osteoprogenitor populations(Chan et al., 2015, 2013; Kim et al., 2016), which are derived from heterogeneous populations of skeletal stem cells (SSCs)(Chan et al., 2015, 2013; Kim et al., 2016). Osteoprogenitors reside in soft tissues alongside endothelial and other cell types that interface with mineralized bone tissue. The two

main described osteoprogenitor niches are the periosteum, which overlays all flat bones(Debnath et al., 2018), and the suture mesenchyme, only present in the skull, between calvarial bones(Wilk et al., 2017). Localized Wnt ligands (Wnts) play crucial roles in regulating osteogenesis, influencing stem cells, progenitors, and mature osteoblasts(Garcin and Habib, 2017; Liu et al., 2009; Lowndes et al., 2016; Matsushita et al., 2020; Okuchi et al., 2021). We recently showed that the Wnt3a-bandage, a transplantable polymer that harbors covalently immobilized Wnt3a proteins, combined with an engineered human osteogenic tissue, can promote bone repair in adult immunodeficient mice(Okuchi et al., 2021).

In this study, using a clinically relevant immunocompetent mouse model, we examined how aspects of the periosteum and suture mesenchyme change with age, how they respond to injury, and the influence of localized Wnts throughout aging.

Young mice achieve almost complete bone repair of calvarial defects considered 'critical sized' in adults, which have limited self-healing ability. We found that age-related changes in bone tissue begin to manifest during adulthood, including increased bone porosity, altered cellular mechanobiology, and declines in mitochondrial activity, vascularity, and the proportion and function of CD90+ osteoprogenitor cells within the periosteum and suture mesenchyme. While Wnt bandage increases CD90+ cells at the defect site regardless of age, this increase only sufficiently promotes repair comparable to young animals in adult mice, not aged mice. Our study characterized a more pronounced decline in osteogenic compartments in aged mice, encompassing reduced CD90+ cell proportion, function, and mitochondrial bioenergetics, alongside other contributing factors. This multifaceted decline leads to severe age-related bone repair deficiency, only partially alleviated by the Wnt3a-bandage, underscoring the need for combinatorial approaches.

To counteract age-related decline in bone repair, we combined localized Wnt3a stimulation with systemic metabolic interventions. In aged mice with critical-size defects, alternating-day intermittent fasting restored osteogenic compartment health, improving CD90+ cell function as well as bone remodelling and significantly enhanced bone repair to levels comparable to younger animals. This effect was recapitulated by even shorter-term supplementation of the gut bacteria Akkermansia muciniphila or nicotinamide mononucleotide (NMN – an NAD+ precursor) in aged mice, highlighting the multifaceted mechanisms of action of intermittent fasting. We further identify mitochondrial dysfunction as a key component in age-related decline in osteoprogenitor function and show that both cyclical nutrient deprivation or NMN rejuvenate mitochondrial health and enhance osteogenesis in vitro.

In summary, our findings highlight that aging tissues retain the potential for health improvements through interventions. Our data reveals an intriguing avenue of research where metabolic and microbiome interventions can be repurposed to treat tissue damage in aged repair-deficient individuals.

Results:

Parietal bone structure deteriorates with aging

Initially, we analyzed the changes that occur in calvarial bone of female C57BL6/J mice during aging at the macro-structure. Young mice (6 weeks) are within the period of fastest bone formation and growth, Adult mice (13 weeks) at healthy homeostasis, and Aged mice (> 88 weeks) correspond to declining skeletal health as a model of >70 year old humans(Dutta and Sengupta, 2016). We evaluated the calvaria of these animals using micro-computed tomography (microCT). The proportion of the total bone volume taken up by mineralized bone tissue (Bone Volume/Total Volume, BV/TV) significantly decreased with age (**Fig. 1a-b**). Cortical bone mineral density (Ct.BMD), the measure of the density of the mineralized bone tissue alone, showed that Aged mice have similar mineral density to Young and Adult mice (nonsignificant differences). The overall thickness

from outer surface to inner surface of the parietal bone significantly increased with age (**Supplementary Fig. 1a-d**).

As parietal bone formation and maintenance is regulated by the cells within the periosteum and suture mesenchyme(Debnath et al., 2018; Li et al., 2021; Maruyama et al., 2016), we next defined the changes that occur within these compartments during aging.

Age-related changes in vascularization, mechanobiology, and osteoprogenitor proportions in osteogenic compartments

We aimed to characterize blood vessels, nuclear and cytoskeletal morphology, and the proportion of osteoprogenitors within the periosteum and suture mesenchyme. Initially, we established that 97% endothelial cells in the periosteum and the suture mesenchyme (osteogenic compartments) express Endomucin and CD31 (**Supplementary Figure 1e, f**). We found that the proportion of Endomucin-positive ($Emcn^{+}$) blood vessels in the periosteum significantly decreases with age (**Fig. 1c-d, Supplementary Fig. 1g-j**). Further vascular histomorphometry shows that, in the periosteum, blood vessel lumen area is consistent throughout aging, indicating that it is the decrease in the blood vessel number per area of tissue that drives the declining blood vessel density. In addition, we find that the thickness of the periosteum itself also decreases rapidly with age (**Supplementary Fig. 1k, l**). Taking increased periosteum thickness and density of blood vessels into account, the estimated blood supply (vessel density multiplied by periosteum thickness) of the whole Young periosteum is over 12-fold higher than that of Aged periosteum. In the suture mesenchyme, blood vessels are larger than in the periosteum, and overall, the vascularization remains stable throughout aging (**Supplementary Fig. 2a, b**).

Vascular phenotypes can result from tissue mechanobiology(Xie et al., 2018). Therefore, we aimed to measure mechanically-driven aspects of cellular morphology in periosteal and suture mesenchymal cells during aging. Nuclear shape is a product of intracellular(Dahl et al., 2008) and extracellular factors, such as the stiffness of the surrounding matrix(Lovett et al., 2013). Morphologically and confirmed by the mean Nuclear Aspect Ratio (NAR, long axis length divided by short axis length) we found significant elongation of nuclei in Aged mice periosteum and to a lesser extent, in the suture mesenchyme (**Fig. 1e-f**).

Nuclear morphology is frequently interlinked with actin cytoskeleton organization, influencing cell migration, proliferation(Ambriz et al., 2018) and response to mechanical force imparted on them through the extracellular matrix(Fletcher and Mullins, 2010; Stricker et al., 2010). We quantified filamentous actin (F-actin) using fluorescent-Phalloidin staining in periosteum and suture mesenchyme (**Fig. 1g-h, Supplementary Fig. 2h**). Aging led to a progressive increase of F-actin, peaking at a 2.5-fold rise between young and Aged mice in suture mesenchyme.

Beyond morphological and cytoskeletal changes, we questioned whether aging periosteal cells experience changes to their cellular energy supply. Adenosine triphosphate (ATP) generation, crucial for cell function, relies largely on mitochondrial membrane potential(Zorova et al., 2018). This can be measured by determining the intensity of Tetramethylrhodamine, methyl ester (TMRM), which accumulates in active mitochondria with intact membrane potentials in live cells(Creed and McKenzie, 2019). *Ex vivo* TMRM intensity was significantly higher in freshly-harvested samples of Young mouse periosteum, than in Adult and Aged mice (**Fig. 1i-j**). This finding is unlikely to be an artefact of differential ECM densities interfering with diffusion as performing the same experiment in explanted cells (i.e. without ECM, **Supplementary Fig. 2c, d**) gave a similar trend of results. We also confirmed equal Hoechst diffusion and staining throughout the *ex vivo* tissue experiment (**Supplementary Fig. 2e, f**).

Given these age-related differences in the osteogenic compartments, we aimed to elucidate changes to the CD90$^+$ osteoprogenitors (Chan et al., 2015, p. 2; Kim et al., 2016, p. 2), (**Supplementary Fig. 2g**). Using in situ immunofluorescence, we found that the proportion of CD90$^+$ in the periosteum and the suture mesenchyme significantly decreases with age, with only around one third retained in Aged mice in each compartment (**Fig. 1k-l**).

These tissue and cell-level changes indicate a significant and multifaceted age-related decline in the calvarial osteogenic compartments. The periosteum and the suture mesenchyme also serve as the primary sources of cells that contribute to osteogenesis during calvarial bone repair(Jeffery et al., 2022; Wilk et al., 2017). Hence, we next characterized how calvarial bone repair is affected by age and how the nearby cells respond to the Wnt3a-bandage.

Wnt3a-bandages increase CD90$^+$ cells in repair areas of Aged and Adult mice and enhance bone repair

Critical-sized calvarial bone defects, challenging to heal without intervention, serve as models to quantitatively evaluate bone repair. Our prior work demonstrated that applying a Wnt3a-bandage and cellular osteogenic construct to the defect site significantly enhances bone repair in adult immunocompromised mice(Okuchi et al., 2021). Considering the crucial role of the immune system in bone healing(Loi et al., 2016) and the prevalence of bone fractures in immunocompetent individuals, we assessed bone repair in female wildtype (C57BL6/J) mice of varying ages. Mice underwent bilateral critical-sized (2 mm) full-thickness calvarial defect surgery in the parietal bones and were treated with one active Wnt3a-bandage and one chemically-inactivated Wnt3a control bandage. Wnt3a-bandage activity was confirmed *in vitro* (**Supplementary Fig. 3a-c**) before transplantation.

We assessed bone repair by measuring the area percentage of re-mineralized tissue within the defect site using microCT after 10 weeks. Interestingly, Young mice exhibited robust bone healing even without intervention, highlighting the natural regenerative capacity of bone in young mice. (**Fig. 1o-p, supplementary table 1**). In adult mice, Wnt3a-bandage treatment significantly enhanced bone repair compared to the control bandage, achieving levels comparable to those observed in young mice. Aged mice exhibited severely impaired repair with both bandages, though Wnt3a-bandage showed a modest but significant increase. New bone formed under Wnt3a-bandage displayed improved lamellar structure (striations) akin to mature undamaged bone (**Supplementary Fig. 3d**).

To uncover cellular mechanisms behind the improved healing, we examined CD90$^+$ osteoprogenitor cells in the defect site. The proportion of CD90$^+$ cells was significantly increased by the Wnt3a-bandage across age groups, compared to control bandages (**Fig. 1m-n**). Wnt3a-bandages locally increase CD90$^+$ cells, but despite similar numbers across ages, the effect of the Wnt3a-bandage on bone repair in Aged mice was limited. We hypothesized, therefore, that the functionality of CD90$^+$ cells, rather than their number alone, may drive age-related differences in bone repair outcomes.

To investigate this, we initially examined the influence of the Wnt-bandage on CD90$^+$ cells across various age groups in terms of Wnt/β-catenin signaling. The proportion of nuclear β-catenin (**Supplementary Fig. 4a-c**), indicative of Wnt/β-catenin signaling activation(Archbold et al., 2012), was significantly increased in CD90$^+$ cells near the active Wnt3a-bandage compared to the inactive bandage. Importantly, the proportion of nuclear β-catenin remained similar regardless of age, suggesting the Aged CD90$^+$ have the capacity to activate the pathway similar to younger CD90$^+$ cells.

We then explored the effects of the Wnt3a-bandage on CD90$^+$ cell proliferation and migration near the bandage. Our results demonstrate that the proportion of CD90$^+$ stained with the proliferation marker Ki67 or MMP2, a Type IV collagenase enzyme linked to migration(Ries et al., 2007) and ECM remodeling in

bones(Zhong-Sheng et al., 2022), appeared increased in CD90$^+$ near Wnt3a-bandage. While this increase was not statistically significant compared to inactive control bandage groups in Aged mice, it was statistically significant in Adult mice (**Supplementary Fig. 4b-e**).

Considering that CD90$^+$ cells inside the defect are ultimately derived from cells that are harbored in the nearby periosteum and suture mesenchyme, we next analyzed the transcriptomes of CD90$^+$ to glean insights into their functional differences during aging.

Transcriptional shifts occur in calvarial CD90$^+$ cells with aging

Single-cell RNA sequencing (scRNAseq) was performed on live cells immediately following dissection and tissue digestion from the periosteum and suture mesenchyme in Young, Adult, and Aged mice, with data processing to deplete immune (CD45$^+$) cells. CD90$^+$ subpopulations of cells (cluster 0, 1 and 3 in the periosteum; cluster 10 in the suture mesenchyme) were identified within both tissues (**Supplementary Fig. 5a-h**), with high transcriptomic similarity to cells expressing Prrx1,Cathepsin K (Ctsk) and Ddr2(Bok et al., 2023; Debnath et al., 2018) (**Supplementary Fig. 6**), markers of periosteal and suture SSCs(Duchamp de Lageneste et al., 2018; Wilk et al., 2017). We also found that the CD90$^+$ population includes minor subsets of cells that express other SSC/progenitor markers including CD200/CD51 (Cd200/Itgav)(Menon et al., 2021), Gli1(Zhao et al., 2015), Axin2(Maruyama et al., 2016) and α-SMA (Acta2)(Ortinau et al., 2019). Therefore, based on functional studies(Kim et al., 2016; Nusspaumer et al., 2017) and our transcriptomic analysis, the CD90$^+$ population encompasses a heterogeneous group of cells that are capable of osteogenic differentiation. Next, we will describe selected transcriptomic changes in CD90$^+$ cells during aging. For Gene ontology number, comparisons and statistics, please see **Supplementary Table 2**.

Comparing Young CD90$^+$ cells with Aged CD90$^+$ cells in the periosteum (**Supplementary Fig. 7a**), 542 genes were significantly upregulated. Of these, 38 corresponded to Gene Ontology (GO) term 'Cytosolic ribosome', linked to increased 'Collagen-containing extracellular matrix'. Similarly in Young vs Aged suture CD90$^+$ cells (**Supplementary Fig. 7b**), 879 significantly upregulated genes are enriched for 'Structural constituent of ribosome' and 'Extracellular matrix structural constituent'. Young mice at 6 weeks of age undergo significant skeletal growth(Jilka, 2013), hence this data closely corroborates the increase in collagenous matrix deposition (both soft and bone tissue) observed in histological sections of bone defects in Young mice.

Given the effect of the Wnt3a-bandage on the Aged bone repair environment, we next probed the differentially expressed genes for components of the Wnt/β-catenin pathway. The transcript's expression of Wnt2 ligand, often implicated in the Wnt/β-catenin pathway(Goss et al., 2009; Jung et al., 2015), was significantly downregulated with age in suture CD90$^+$ cells (**Supplementary fig. 7b,d**). Further, Wnt co-receptor Lrp6 expression significantly declined with age in periosteal CD90$^+$ cells (**Supplementary fig. 7a**). Collectively, this suggests compromised Wnt signaling in the periosteum and suture mesenchyme during aging.

At the Adult and Aged timepoints, bone is at healthy and declining homeostasis, respectively. We compared Adult and Aged CD90$^+$ cells in the periosteum (**Supplementary Fig. 7c**). Here, the 637 genes significantly upregulated in Adult vs Aged were vastly enriched for GO terms 'NADH dehydrogenase complex assembly', 'NADH dehydrogenase (ubiquinone) activity' and 'Oxidative phosphorylation'. Likewise, in the suture mesenchyme (**Supplementary Fig. 7d**), the 610 genes significantly upregulated in Adult vs Aged CD90$^+$ cells were also enriched for 'Mitochondrial ATP synthesis coupled proton transport' and 'Oxidative phosphorylation'. Using the UCell method(Andreatta and Carmona, 2021), we found significantly reduced Complex I gene scoring with age in the suture mesenchyme and the periosteal CD90$^+$ cells (**Supplementary Fig. 7e-f**). These results, coupled with live measurements of mitochondrial membrane potential (**Fig. 1i-j**), indicate an age-

related decline in mitochondrial metabolism and electron transport chain (ETC) complexes within CD90$^+$ cells of the whole periosteum and suture mesenchyme. Importantly, we did not observe distinct changes in the signature of Glycolysis or lipid metabolism across age groups in CD90$^+$ cells in the osteogenic compartments (**Supplementary Fig 7g-j**).

Analysis with the CellChat package(Jin et al., 2021) shows inferred signaling heterogeneity within the periosteal CD90$^+$ population (**Supplementary Fig. 8a**). Cells within the smaller CD90$^+$ cluster (cluster 3, **Supplementary Fig. 5a-d**) receive incoming Wnt-signals and also Periostin-signalling, which upregulates Wnt/β-catenin pathway activity in osteogenesis(Lv et al., 2015; Zhang et al., 2017). This cluster is significantly upregulated for markers of osteogenic differentiation such as Runx2, Mme (Osteonectin/CD10)(Ding et al., 2020; Granéli et al., 2014), Bgn(Ye et al., 2012), Mgp(Zhang et al., 2019), Gas6(Shiozawa et al., 2010), and Igbp7(Zhang et al., 2018), and is hereby termed the P1 CD90$^+$ population. Cells within the larger cluster (clusters 0 & 1) both send and receive Periostin and Wnt-signals, and is significantly upregulated for markers associated with stemness, such as Klf4 and Aldh1a3(Wanandi et al., 2018), and negative regulators of osteogenic differentiation such as Bmp3(Kokabu et al., 2012), and Ccn3(Matsushita et al., 2013). Hereby these cells were termed P2 CD90$^+$.

The periosteal P2 CD90$^+$ cell population shifts with age between two categories, named 'Igf1^{high}' and 'Igf1^{low}' in relation to their differential expression of Igf1 (**Fig. 2a-c**). Igf1 is linked to bone anabolism through its dual roles in enhancing Wnt-signaling and exerting metabolic effects(Locatelli and Bianchi, 2014). Young P2 CD90$^+$ cells were restricted to the Igf1^{high} grouping (92.0%), while Aged CD90$^+$ cells were predominantly in the Igf1^{low} grouping (66.3%) (**Fig. 2a-b**). Adult CD90$^+$ cells were more evenly split (56.8% Igf1^{high}, 43.2% Igf1^{low}). Igf1^{low} cells were significantly upregulated for 85 genes (**Fig. 2c**), linked 'Cell motility', driven by genes such as Mmp14(Almalki and Agrawal, 2016) and Itgb7(Novoseletskaya et al., 2020). Igf1^{high} cells were significantly upregulated for 204 genes linked to 'Collagen-containing extracellular matrix', 'Oxidative phosphorylation' and 'Respiratory chain complex'. The enrichment is driven by significantly upregulated genes such as NADH dehydrogenase genes (mt-Nd1 & mt-Nd2), Col1a1, Sparc.

Likewise, in the suture mesenchyme, analysis of inferred cellular state and function (**Fig. 2d-e**) revealed a distinct subpopulation of CD90$^+$ cells. This group of cells was significantly upregulated for 855 genes linked to 'Mitotic cell cycle' and 'ATP-dependent activity'. In Young mice, this population, termed 'Proliferating' cells, represented 48.72% of the CD90$^+$ population, whereas it markedly declined to around 8% in both Adult and Aged mice (**Fig. 2d-e**).

When comparing CD90$^+$ cell populations between every two age stages, several genes are conserved in all three comparisons (**Supplementary Fig. 8b, c**), including: Cavin1(Volonte and Galbiati, 2020), S100a4(Wagner et al., 2009), Vcan(S. Li et al., 2019), Mmp14(Haage et al., 2014), and Nsg1(Wiese et al., 2019). Each of these genes has been identified as being involved in senescence or the cellular response to aging tissues. Likewise, in the suture CD90$^+$ cells, conserved aging-related genes included senescence-related genes Pim1(Yang et al., 2017), Pdcd4(Kang et al., 2002); and the senescence-associated secretory profile (SASP) gene Ccl6(Gillispie et al., 2021). Further comprehensive senescence signature confirms the significant increase associated with age in CD90$^+$ cells (**Supplementary Fig. 8d**). Also conserved were: pro-bone resorption Mmp9(Zhu et al., 2020), and adipogenesis-related genes ApoD(Provost et al., 1991) and Slc16a3 (MCT4)(Petersen et al., 2017).

Aging calvarial CD90$^+$ cells undergo a decline in energy supply, proliferation, Wnt/β-catenin, and ECM remodeling capacity

Next, we aimed to investigate the transcriptionally-identified decline in energy supply, proliferation, Wnt/β-catenin pathway, and migration in CD90$^+$ cells at the protein level through immunofluorescent staining of marker proteins.

The catalytic beta subunit of ATP synthase (ATPB), an essential component of the mitochondrial ATP synthesis machinery, serves as a marker for assessing energy-related mitochondrial function(H.-S. Li et al., 2019). Cellular ATPB levels in suture mesenchyme CD90$^+$ cells is similar across age groups, but in the periosteal CD90$^+$ cells, ATPB level is lower in Aged mice compared to Adults (**Fig. 2f, l**). Phosphorylated AMPK (phospho-AMPK), a sensor of ATP depletion(Gowans and Hardie, 2014), exhibits a negative correlation with energy availability. In both periosteum and suture CD90$^+$ cells, mean phospho-AMPK was significantly higher in Aged mice (**Fig. 2g, l**). Taken together, these findings suggest a potential deficiency in oxidative phosphorylation machinery in CD90$^+$ cells with age.

Ki67 marks active proliferation, while cyclin-dependent kinase inhibitors p16 is involved in various cellular functions and is linked to senescence and aging in several tissues(Safwan-Zaiter et al., 2022; Stein et al., 1999, p. 199). Calvarial CD90$^+$ cells were assessed for nuclear expression of the two markers. Ki67$^+$ CD90$^+$ cells were observed in the periosteum of both Young and Adult mice but not in Aged mice. In the suture, the proportion of Ki67$^+$ CD90$^+$ was significantly higher in Young than in Adult mice with none detected in Aged mice (**Fig. 2h, l**). The proportion of p16$^+$ CD90$^+$ cells appeared to increase with Age (**Fig. 2i, l**). Together, nuclear p16 expression and a lack of Ki67 expression suggests that Aged CD90$^+$ cells are not actively proliferating, corroborating inferred findings from transcriptomics.

Next, we assessed the level of nuclear β-catenin, an indicator of Wnt/β-catenin pathway activation. Aged CD90$^+$ cells in both periosteum and suture mesenchyme showed significantly reduced nuclear localization of β-catenin compared to Young (**Fig. 2j, l**). Only Adult CD90$^+$ cells in the periosteum had significantly higher nuclear β-catenin when compared to Aged mice.

Finally, in both periosteum and suture mesenchyme, Aged CD90$^+$ cells expressed the lowest amounts of MMP2 (**Fig. 2k-l**). While MMP2 is a secreted protein, only intracellular protein was quantified, to enable the analysis to be restricted to MMP2 expressed by CD90$^+$ cells alone. It corroborates the downregulation of genes associated with migration in the transcriptomic analysis.

Overall, our protein-level analysis largely aligns with the transcript-level findings, insinuating that age-related alterations in periosteum and suture mesenchyme, and consequently bone repair, could be considerably impacted by metabolic differences within the CD90-expressing population.

Given that increasing the number of CD90$^+$ cells inside the defect alone produced only a minor improvement to Aged bone repair, we developed a systemic approach to target cellular metabolism. We aimed to combine this systemic approach with the use of the Wnt3a-bandage to ultimately facilitate the supply of competent osteogenic cells for bone repair.

Intermittent Fasting improves bone health and bone repair in Aged mice

Intermittent Fasting (IF) can improve metabolic control by various measures(Longo et al., 2021) and bone mineral density in adult animals (Veronese and Reginster, 2019). We produced critical-sized calvarial defects in Aged mice, treated them with Wnt3a-bandages and inactive controls. These mice were then maintained on

330 an alternating-day diet of self-limited feeding and complete fasting, hereby termed the intermittent fasting (IF)
331 diet. Importantly, over the course of a week, mice intake the same amount of food during the IF diet as during
332 the self-limited feeding controls (*ad libitum*, AL) diet (**Supplementary Fig. 9a**), and is therefore distinct from
333 an overall reduction in calories (i.e., caloric restriction).
334
335 Remarkably, Aged mice subjected to the IF diet repaired 59.24% of the defect within 10 weeks under the
336 inactive bandage, higher even than that of Adult mice + inactive bandage (**Fig. 1o-p**). With the addition of the
337 Wnt3a-bandage, bone repair area was increased to 67.10%. This combination approach of the local Wnt3a-
338 bandage and post-fracture IF results in Aged calvarial bone repair rivaling that of Young mice. The IF diet also
339 significantly increased the solid bone proportion (BV/TV) (**Fig. 3a-b**), making it similar to the much younger
340 Adult bone.
341
342 **Intermittent Fasting reverses aspects of cellular and tissue aging in the periosteum and suture**
343 **mesenchyme**
344 Compared to Aged mice, in Aged + IF, Emcn$^+$ vascularity in the periosteum was significantly increased (**Fig.**
345 **3c-d**). Additionally, in the suture mesenchyme, actin cytoskeleton staining was markedly decreased (**Fig. 3e-**
346 **f**), along with a significant reduction in age-related nuclear elongation both in the suture and periosteum (**Fig.**
347 **3g-h**). The IF diet appeared to elevate the proportion of CD90$^+$ cells in the periosteum while in the suture, it
348 significantly increased compared to ad libitum (**Fig. 3i-j**).
349
350 To gain a deeper understanding of how IF affects Aged CD90$^+$ cells, we conducted further scRNAseq analysis.
351 We maintained Adult and Aged mice on the alternating-day IF diet for 10 weeks before performing scRNAseq
352 on the periosteum and suture mesenchyme.
353
354 Comparing CD90$^+$ cells of Aged periosteal post IF diet with Aged AL diet controls revealed 98 significantly
355 upregulated genes (**Fig. 4a**). These were enriched mainly for 'Response to cytokine' and similar GO terms.
356 Of the genes upregulated with the IF diet, 10 were individually statistically significant when adjusting for false
357 discovery rate ($q < 0.05$). Ccl11 and Duox2 are involved in osteogenic stem cell migration(Smith et al., 2012;
358 Tyurin-Kuzmin et al., 2016), Tnfaip6 and Ccl7 in immunomodulation(Li et al., n.d.; Rafei et al., 2008), Ptx3 is
359 involved in both processes(Cappuzzello et al., 2016), and Actg1 in cytoskeletal structure(Dugina et al., 2009;
360 Simiczyjew et al., 2014). Zbtb16, encoding transcription factor PLZF, regulates osteogenesis by acting
361 upstream of master osteoblast transcription factor Runx2 (**Supplementary Fig.9b**)(Agrawal Singh et al.,
362 2019; Liu and Lee, 2013).
363
364 In the suture mesenchyme, analysis of 297 significantly upregulated genes in Aged CD90$^+$ cells during the IF
365 diet compared to Aged AL control (**Fig. 4b**) showed enrichment in 'Mitotic cell cycle' and 'Protein
366 phosphorylation'. Notably, the proliferation marker Mki67 is significantly upregulated, with a threefold increase
367 in Aged periosteum CD90$^+$ cells during intermittent fasting compared to ad libitum diet.
368
369 In **Fig. 2a**, a shift in the periosteal CD90$^+$ was noted with aging. Aged AL had relatively fewer osteogenic
370 Igf1^{high} cells, and more of Igf1^{low} cells. Contrary, Aged + IF CD90$^+$ cells were split 70.3% Igf1^{high}, 29.7% Igf1^{low}
371 (**Fig. 4c-d**), positioning them between Young and Adult distributions. 2 of the 14 genes identified as conserved
372 markers of periosteal CD90$^+$ cell aging (**Supplementary Fig. 8b**), Vcan, Mmp14, were significantly
373 downregulated in Aged +IF. The proportion of 'proliferating' CD90$^+$ suture cells increased in Aged + IF (**Fig.**
374 **4e-f**). Further, 1 of the 32 conserved genes of the aging suture (**Supplementary Fig. 8c**), actin-associated
375 Tpm1(Li et al., 2022), was significantly downregulated in Aged + IF. Wnt2, found to be downregulated with

aging, is significantly upregulated in the suture CD90$^+$ population of Aged + IF (source data_RNAseq table 10).

To validate diet-induced changes in CD90$^+$ cells, we conducted immunostaining for protein markers in histological sections. ATPB, marker of ATP synthase, appeared elevated in periosteum and significantly increased in suture mesenchyme CD90$^+$ cells following IF (**Fig. 4g-m**). This suggests an increase in cellular ATP levels, which is supported by decreases in ATP-deficiency sensor phospho-AMPK in periosteal and suture CD90$^+$ cells (**Fig. 4h, m**). While proliferating cells were absent in Aged mice, we observed Ki67$^+$ cells in samples of the periosteum of 3 out of 5 Aged + IF mice and in 4 out of 5 Aged + IF mice for suture mesenchyme (**Fig. 4i, m**). Conversely, p16 was similar in periosteum and suture mesenchyme (**Fig. 4j, m**). Wnt/βcatenin pathway activity, as measured by the relative nuclear localization of β-catenin, was significantly increased within the CD90$^+$ cells of both the periosteum and suture (**Fig. 4k, m**). Lastly, expression of the motility marker MMP2 in CD90$^+$ cells was markedly increased over Aged controls in the periosteum, and just under statistical significance in the suture mesenchyme (**Fig. 4l, m**).

Together, this data suggests that during IF, CD90$^+$ cells, despite being Aged, are more capable of ECM modulation and migration, and are pro-osteogenesis.

Short term metabolic approaches rejuvenate the calvarial osteogenic compartments of Aged mice and promote bone repair

IF diet likely enhances energy supply to CD90$^+$ cells and their function through various mechanisms. We next aimed to determine if specific underlying mechanisms alone could replicate the effects of IF on aged bone repair. Our analysis revealed that both aging and IF affect the NAD$^+$ biosynthesis pathway and gut microbiota. Thus, we targeted these aspects to investigate their potential to enhance aged bone repair.

NMN supplementation improves bone repair in Aged mice

NAD$^+$ is a multifunctional enzyme co-factor with roles including protein deacetylation, histone modification, intracellular signaling, and redox reactions (Covarrubias et al., 2021). It is also crucial in oxidative phosphorylation(Stein and Imai, 2012), cycling between oxidized and reduced forms (NAD$^+$/NADH) in the mitochondria as part of the electron transport chain. Our analysis of inferred NAD$^+$-dependent pathway activity (**Supplementary Fig.7e,f**), live mitochondrial activity (**Fig. 1i-j**), and markers of cellular energy levels (**Fig. 2f, g, l**) demonstrated distinct changes to metabolism with age. Yet, little is known about the effect of NAD$^+$-coupled cellular metabolism on the composition of aging calvarial periosteum and suture mesenchyme and its influence over Aged bone repair.

To increase cellular levels of NAD$^+$ systemically, we orally dosed Aged mice with nicotinamide mononucleotide (NMN), an immediate precursor to NAD$^+$ in the 'salvage' pathway(Yang and Sauve, 2016). During a pilot study involving oral NMN supplementation (600 mg/kg, 3 times within 1 week) in Adult mice, the mitochondrial membrane potential, as measured by TMRM staining, within the cells of the periosteum was significantly increased (**Fig. 5a, b**). NMN was then administered to Aged mice for the 2 weeks prior and 2 weeks following calvarial defect surgery.

Parietal bone BV/TV was significantly increased in Aged animals that received NMN (Aged + NMN) (**Fig. 5c-d**). Remarkably, Aged bone repair was significantly increased to 54.32% with NMN with inactive bandages (**Fig. 1o-p**), marking a three-fold improvement over control Aged mice. Adding Wnt3a-bandage increased

423 Aged + NMN repair to 71.18%, resulting in over 2.71 times greater area of new bone compared to Aged
424 controls + Wnt3a-bandage, akin to repair in Adult mice + Wnt3a-bandage.
425
426 Next, we probed how NMN affects $CD90^+$ cells in the osteogenic compartments. In the suture mesenchyme,
427 NMN treatment significantly increased CD90+ cells compared to Aged control (**Fig. 5e-f**). In the periosteum,
428 CD90+ populations were unchanged. Additionally, compared to Aged controls, NMN supplementation
429 significantly increased the vascularity of the periosteum (**Fig. 5g-h**), and approximately halved actin
430 cytoskeletal staining intensity in the suture mesenchyme (**Fig. 5i-j**). Nuclei in the suture and periosteum were
431 rounder and less elongated than Aged controls (**Fig. 5k-m**), making them morphologically resemble Adult
432 nuclei.
433 Taken together, NMN treatment increased periosteal vascularity, impacted aspects of the mechanobiology of
434 the periosteum and suture mesenchyme, leading to a significant improvement in bone repair in Aged mice.

435 *Cyclical nutrient deprivation and NMN enhance mitochondrial function in osteogenic cells in vitro*

436 Next, we aimed to model aspects of the effects of intermittent fasting and NMN supplementation on osteogenic
437 cells, employing a cyclical nutrient deprivation regimen or NMN supplementation *in vitro* to elucidate aspects
438 of their mechanisms of action. While this approach allows us to study specific cellular responses, it is crucial
439 to recognize that it cannot fully replicate the complex systemic effects of *in vivo* intermittent fasting.
440 We investigated the impact of these interventions on mitochondrial function in the MC3T3 calvarial
441 osteoblastic cell line, a model commonly utilized to study osteogenesis *in vitro* and known for its ability to
442 contribute to bone formation *in vivo*(Horowitz et al., 1994; Paine et al., 2018; Wang et al., 1999) .
443
444 Alternating serum deprivation every hour (cyclical nutrient deprivation) in glucose-free medium induced the
445 expression of genes related to mitochondrial biogenesis, fusion, mitophagy, and the unfolded protein response
446 (**Fig. 6a**). This was accompanied by increased mitochondrial filament length and membrane potential,
447 indicating enhanced mitochondrial function(McCarron et al., 2013; Westermann, 2012) (**Fig. 6b-e**). These
448 findings are consistent with *in vivo* observations of improved mitochondrial function in animals subjected to
449 intermittent fasting. While cyclical nutrient deprivation enhanced mitochondrial membrane potential, it also
450 reduced overall cellular ATP levels. However, inhibiting mitochondrial ATP production with oligomycin (a
451 Complex V inhibitor)(Devenish et al., 2000) further diminished ATP levels, suggesting that mitochondrial
452 respiration is a primary source of ATP in these cells (**Fig. 6f**).
453 Recognizing the role of mitochondrial dysfunction in aging, we investigated the impact of NMN on MC3T3
454 cells challenged with oligomycin and cultured in glucose and pyruvate-free medium. NMN treatment mitigated
455 oligomycin-induced ATP loss and ROS production, enhanced cell proliferation, and prevented the loss of
456 mitochondrial membrane potential (**Fig. 7a-c**). Holotomography microscopy revealed that NMN preserved the
457 "rod-like/filament" morphology of mitochondria in oligomycin-treated cells (**Fig. 7d-e**). Furthermore, NMN
458 restored the expression of genes related to mitochondrial biogenesis and dynamics, the unfolded protein
459 response, and mitophagy, which were adversely affected by oligomycin (**Fig. 7f**). Ultimately, NMN enhanced
460 the growth and differentiation potential of oligomycin-treated cells, as evidenced by increased ALP activity
461 and mineralization (**Fig. 7g**).
462
463 In summary, our findings suggest that both cyclical nutrient deprivation and NMN supplementation can
464 enhance mitochondrial function in osteogenic cells. NMN appears to protect against mitochondrial dysfunction
465 induced by Complex V inhibition, highlighting its potential in mitigating the decline in osteogenic cell function.
466
467 *Akkermansia muciniphila supplementation improves bone repair in Aged mice*

468 The ‘gut-bone axis’ links food intake, gut microbiome and bone metabolism via circulating metabolites(Villa et
469 al., 2017). Bacteria in the genus *Akkermansia* appeared to be elevated during Aged + IF compared to the AL
470 control diet (**Fig. 5n**), consistent with previous studies that found similar results in young mice and human(Li
471 et al., 2020; Özkul et al., 2019).
472
473 *Akkermansia muciniphila* is an anaerobic gut bacterium responsible for mucin turnover(Derrien et al., 2008),
474 and a regulator of the intestinal mucus environment(Reunanen et al., 2015). The *Akkermansia* population
475 exerts wider effects on the gut microbiome, and has been studied for its roles in metabolic health(Dao et al.,
476 2016; Leite et al., 2021). We cultured *Akkermansia muciniphila* (Akk) under anaerobic conditions and
477 calculated the viability of cryopreserved aliquots. Doses of live Akk (2 x 10^8 C.F.U.) were given by oral gavage
478 three times per week in Aged mice for the 2 weeks prior and 6 weeks following calvarial defect surgery.
479
480 Our metagenomic analysis reveals that Firmicutes:Bacteroides ratio, indicator of microbiome
481 composition(Magne et al., 2020), is significantly increased in Aged mice with *Akkermansia* supplementation
482 (Aged + Akk) (**Supplementary Fig. 10a)**. Furthermore, the proportion of gut bacteria belonging to family
483 *Lachnospiraceae,* indicative of the capacity of the gut bacteria to produce short chain fatty acids (SCFAs), is
484 significantly elevated in Aged + Akk (**Supplementary Fig. 10b**). SCAFs enter the host bloodstream and exert
485 epigenetic effects primarily through histone modification, which might have implication on cell function and
486 differentiation(Licciardi et al., 2011).
487
488 Similar to NMN treatment, parietal bone BV/TV was significantly increased Aged +Akk (**Fig. 5c-d**). Aged bone
489 repair was significantly increased to 43.76% with Akk and inactive bandages (**Fig. 1o-p**). In combination with
490 the Wnt3a bandage effect, bone repair in Aged + Akk further increased to 64.84%. This level of bone repair is
491 similar to that of Young mice with Wnt3a-bandage (**Supplementary Table 1**). Aged + Akk also produced
492 striated bone, similar in structure to Young mice, under both Wnt3a and control bandages (**Supplementary
493 Fig. 3d**).
494
495 Aged + Akk led to a significant increase in $CD90^+$ cells in the periosteum and suture mesenchyme (**Fig. 5e-f**)
496 and a threefold increase in the $Emcn^+$ vascularity area of the periosteum (**Fig. 5g-h**). Compared to Aged
497 controls, in Aged + Akk, actin cytoskeletal staining intensity appeared reduced (not significant) in the suture
498 mesenchyme (**Fig. 5i-j**), and nuclei in both the suture and periosteum appeared rounder and less elongated
499 (**Fig. 5k-m**). Accordingly, the nuclear morphology of Aged + Akk cells resembles that of younger mice.

500 **Elevated osteoclast activity associated with enhanced bone health in Aged mice following
501 interventions**

502 To investigate the impact of age and interventions on bone remodeling, we assessed osteoclast activity across
503 different age groups (Young, Adult, and Aged) and compared aged animals who underwent either IF or Akk
504 or NMN interventions to untreated controls. The tartrate-resistant acid phosphatase (TRAP) assay(Yang et
505 al., 2019) results revealed an expected increase in osteoclast activity with age (**Supplementary Fig. 10c-d**).
506 Interestingly, Aged mice treated with IF, NMN, or Akk exhibited significantly higher TRAP activity compared
507 to the untreated aged control group. This finding suggests that these interventions not only enhance bone
508 formation but also promote the removal of old or damaged bone by stimulating osteoclast activity. This
509 coordinated increase in both bone formation and resorption likely contributes to a more youthful and efficient
510 remodeling process, ultimately leading to improved bone health and repair in aged mice.

In summary, we have revealed a multifaceted decline in CD90$^+$ cells with aging, which can be locally counteracted by a Wnt3a-bandage or systemically enhanced through an IF diet. Moreover, systemic interventions, acting via the gut and on shorter terms, can improve CD90$^+$ populations, osteogenic compartments, and significantly enhance bone repair in Aged mice. Combining the Wnt3a-bandage with systemic interventions targeting cellular energy supply, proliferation, migration, and Wnt signaling presents coordinated and clinically relevant approaches, promising rejuvenation of Aged bone repair comparable to younger individuals.

Discussion

Here we report on systemic interventions that can reverse aspects of the aging osteogenic tissue to promote effective calvarial bone repair (**Supplementary Fig. 11**).

While extensive research focuses on long bones(Yates et al., 2007), there is a significant gap in understanding aging in flat bones. Our study on the calvaria demonstrates a clear decline in both bone structure and healing capacity with age. Focusing on osteogenic tissues, we observed a progressive decline in periosteal blood vessel density beginning in adulthood. Microvascular rarefaction is increasingly recognized as a driver, rather than merely a consequence, of hallmarks of cellular aging, such as cellular senescence(Goligorsky, 2010; Lähteenvuo and Rosenzweig, 2012). Indeed, previous studies inducing vasculature loss in young animals accelerates cellular aging(Chen et al., 2021), while mitigating this vascular decline preserves tissue health and delays aging(Grunewald et al., 2021).

Aging bone tissues are inherently more hostile and pro-apoptotic(Almeida, 2012), leading to limited success with cell-based repair approaches in aged individuals(Hirata et al., 2022; Liu et al., 2018). Stiffness increases with aging in various tissues(Ferrari and Pesce, 2021; Lim and Ito, 2022; Segel et al., 2019), impacting cytoskeletal configuration(Khan et al., 2020; Pongkitwitoon et al., 2016) and significantly affecting osteogenic differentiation and senescence *in vitro*(Liu et al., 2022). Our study shows increased actin expression and elongated nuclear shape in aging osteogenic compartments, alongside elevated levels of Mmp9 and Mmp14, linked to stiffer osteogenic tissues(Tang et al., 2013; Zhu et al., 2020). These changes are associated with a decline in both the number and function of osteoprogenitors, including impaired proliferation, mitochondrial energy metabolism, Wnt/β-catenin pathway activation, migration, and ultimately, bone defect repair. While Wnt-bandage treatment increases the number of osteoprogenitors in the defect site across all age cohorts, it only modestly enhances bone repair in aged animals compared to the healing observed in adult mice.

We show that interventions improving whole-body energy metabolism can enhance aged bone health and repair. While IF is effective in delaying aging in adult flies, animals need to switch back to ad libitum feeding at older ages(Catterson et al., 2018), and increased protein intake is suggested for optimizing health span and longevity in aged mice and humans(Levine et al., 2014). Our findings, however, reveal a distinct paradigm for IF in aged bone repair. Specifically, short-term IF initiated post-injury robustly enhances bone healing in aged animals, comparable to younger counterparts.

Mechanistically, IF exerts its effects through several pathways, including enhanced stress resistance, increased reliance on lipid fuel utilization, and activation of proteostatic mechanisms, all contributing to delayed aging(Longo and Anderson, 2022). Although we did not observe distinct changes in overall signature of lipid metabolism or glycolysis in osteogenic tissues during aging or IF, we did find a decline in mitochondrial function and ATP supply with age. Our *in vitro* studies showed that alternating cycles of serum deprivation and supply in osteogenic cells induced genes related to the unfolded mitochondrial protein response, mitophagy and mitochondrial fission associated with increased mitochondrial membrane potential and mitochondrial fission, indicating improved function(McCarron et al., 2013; Westermann, 2012).

Our transcriptomic analysis shows that Mmp14 is reduced during IF in the periosteum. In the suture mesenchyme, Piezo1, a gene known to mediate mechanically induced aging(Ren et al., 2022; Segel et al., 2019), was also significantly reduced in aged mice undergoing IF. Along with the reversal of nuclear cell

558 morphology and levels of F-actin, these results indicate that IF also impacts the mechanobiology of the tissue,
559 making it resemble that of younger animals.
560 IF also led to beneficial shifts in gut microbiota composition, including elevated levels of Akkermansia
561 muciniphila and increased expression of genes involved in NAD^+ biosynthesis. Subsequently, we show that
562 short-term supplementation with Akkermansia muciniphila or NMN in aged mice significantly improve
563 periosteal blood vessel density, osteoprogenitor number and function, osteoclast activity and enhance bone
564 health and repair.
565 Although IF, Akk or NMN can act through many pathways and cellular processes, previous studies highlighted
566 their beneficial effect on metabolism particularly their influence on NAD-dependent pathways. Mechanistically,
567 our *in vitro* studies using calvarial osteogenic cells revealed that NMN protects against mitochondrial damage,
568 often associated with aging, promotes healthy mitochondrial morphology and function, and enhances
569 osteogenesis.
570 The effects of the three metabolic approaches on bone health and repair have not been studied in the context
571 of already-aged individuals. NMN shows protective effects against bone health decline, but in long-term
572 studies that begin dosing well before old age(Kim et al., 2021; Mills et al., 2016; Song et al., 2019). The impact
573 of Akkermansia muciniphila on bone health or healing has only been investigated in young adult models with
574 subcritical defects(Lawenius et al., 2020; Liu et al., 2020). IF diet has been investigated for skin wounding(Luo
575 et al., 2020) in young animals but not for bone repair. We present key progress in developing three clinically
576 relevant approaches for bone tissue regeneration in elderly patients. First, we describe the effects of NMN or
577 Akkermansia dosing, or IF diet on bone tissues in aged animals that have already experienced severe skeletal
578 decline. Second, our rejuvenation protocols are applied for shorter terms, and even post-injury with IF diet.
579 This study offers valuable insights into bone aging and rejuvenation strategies. However, future research
580 should address several limitations. Further investigation is needed on the mechanisms of action of IF, NMN,
581 and Akkermansia, optimal intervention timing and duration, and synergistic effects of combined approaches.
582 While this study focused on a common osteoprogenitor, investigating the roles of specific skeletal stem cell
583 populations and other cells within the osteogenic compartments (including immune cells) in flat bones
584 represents a compelling frontier.
585 Our findings suggest broader implications beyond bone health, with these rejuvenation strategies potentially
586 translating to other aging organs and injuries. Rigorous investigation of dosage, safety, and long-term effects
587 will be essential for human applications.
588

Figure and Legends

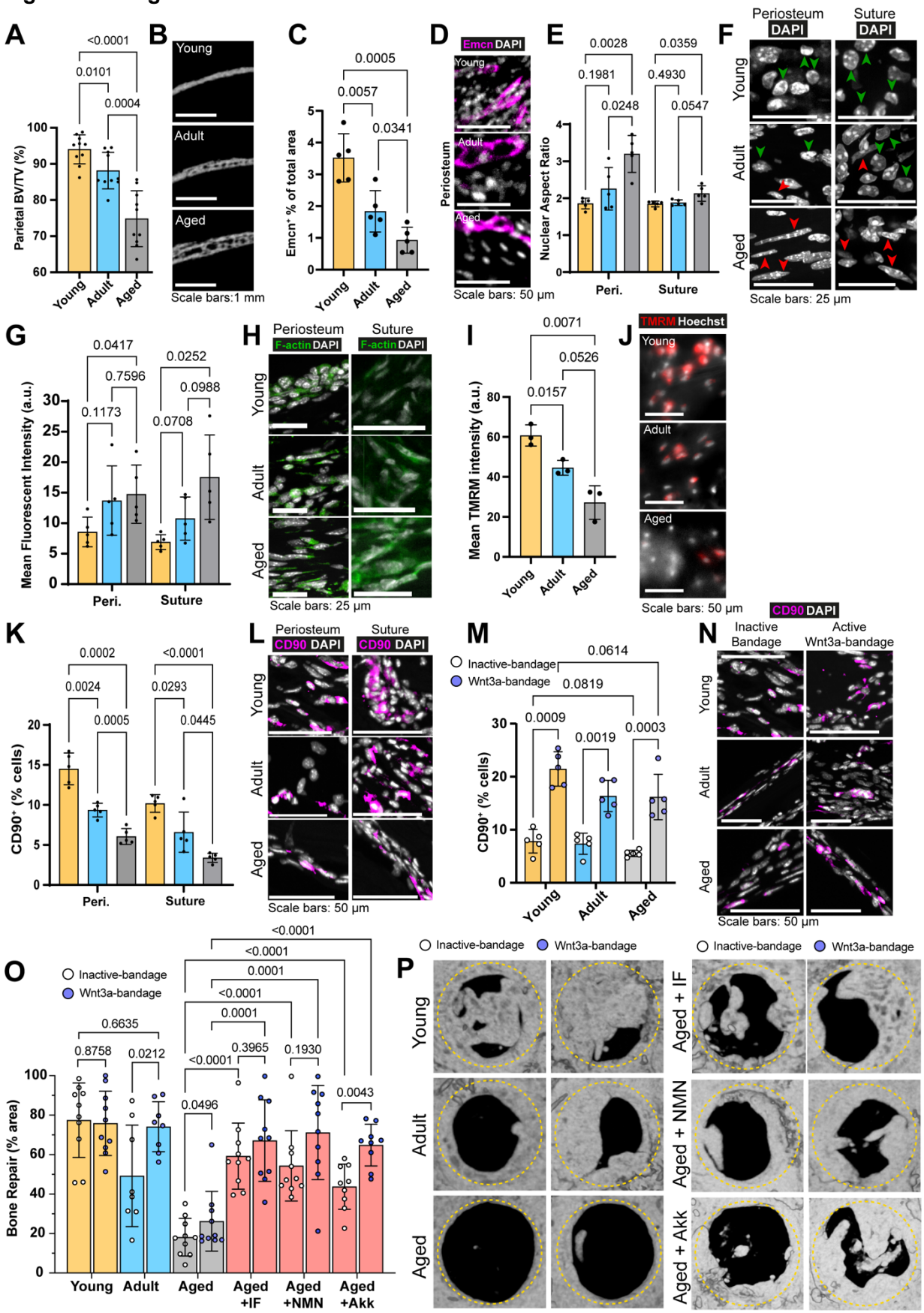

591 **Figure 1 Changes to the calvarial bone, periosteum and suture mesenchyme, and bone repair with**
592 **aging and interventions**
593 (**A**) Parietal Bone Volume/Total Volume (BV/TV) and (**B**) representative transverse micro computed
594 tomography (microCT) sections in Young, Adult, and Aged mice. Statistical analysis: Welch's test in n = 10
595 mice per condition. (**C**) Mean cross sectional area taken up by Endomucin (Emcn)-positive vascular cells and
596 (**D**) representative immunofluorescence staining of Emcn (magenta) and DAPI (grey) in Young, Adult, and
597 Aged mouse periosteum. Statistical analysis: Welch's tests in n = 5 mice per condition. (**E**) Nuclear aspect
598 ratio (long axis divided by short axis) of cells within the periosteum and suture mesenchyme and (**F**)
599 representative DAPI-stained nuclei in Young, Adult, and Aged mice. Statistical analysis: Welch's tests in n =
600 5 mice per condition. Green and red arrows highlight rounded and elongated nuclei, respectively. (**G**) Mean
601 Phalloidin-488 fluorescence intensity and (**H**) representative images for filamentous actin (F-actin, green) and
602 DAPI (grey) in Young, Adult, and Aged mouse periosteum and suture mesenchyme. Statistical analysis:
603 Welch's tests in n = 5 mice per condition. (**I**) Mean intensity and (**J**) representative images of live TMRM
604 staining (red) and Hoechst (grey) in Young, Adult, and Aged mouse periosteum *ex vivo*. Statistical analysis:
605 Welch's tests in tissue from n = 3 mice per condition. (**K**) Percentage of $CD90^+$ cells within the periosteum
606 and suture mesenchyme, expressed relative to the total cellular number ($DAPI^+$) in Young, Adult, and Aged
607 mice. Representative images (**N**) show CD90 immunostaining (magenta) and DAPI (grey). Statistical analysis:
608 Welch's tests in n = 5 mice per condition. (**M**) Percentage of $CD90^+$ cells within calvarial defects treated with
609 Wnt3a-bandages (blue points) or inactive controls (white points), expressed relative to the total cellular
610 number ($DAPI^+$) in Young, Adult, and Aged mice. (**N**) Representative images show CD90 immunostaining
611 (magenta) and DAPI (grey). Statistical analysis: ratio-paired two-tailed t tests in n = 5 mice per condition. (**O**)
612 Percentage of repair and (**P**) representative top-down microCT images within calvarial defects treated with
613 Wnt3a-bandages (blue points) or inactive controls (white points). Statistical analysis within age groups: ratio-
614 paired two-tailed t tests; between age groups and Aged mice following the IF protocol or NMN or Akk
615 supplementation: Welch's tests; Young, Aged, Aged + IF, Aged + NMN, n = 10 mice; Aged + Akk, n = 9; Adult,
616 n = 8. Complete statistical analysis between aged groups and treatments can be found in **Supplementary**
617 **Table 1**. The yellow dashed circle highlights the 2 mm diameter defect size.
618

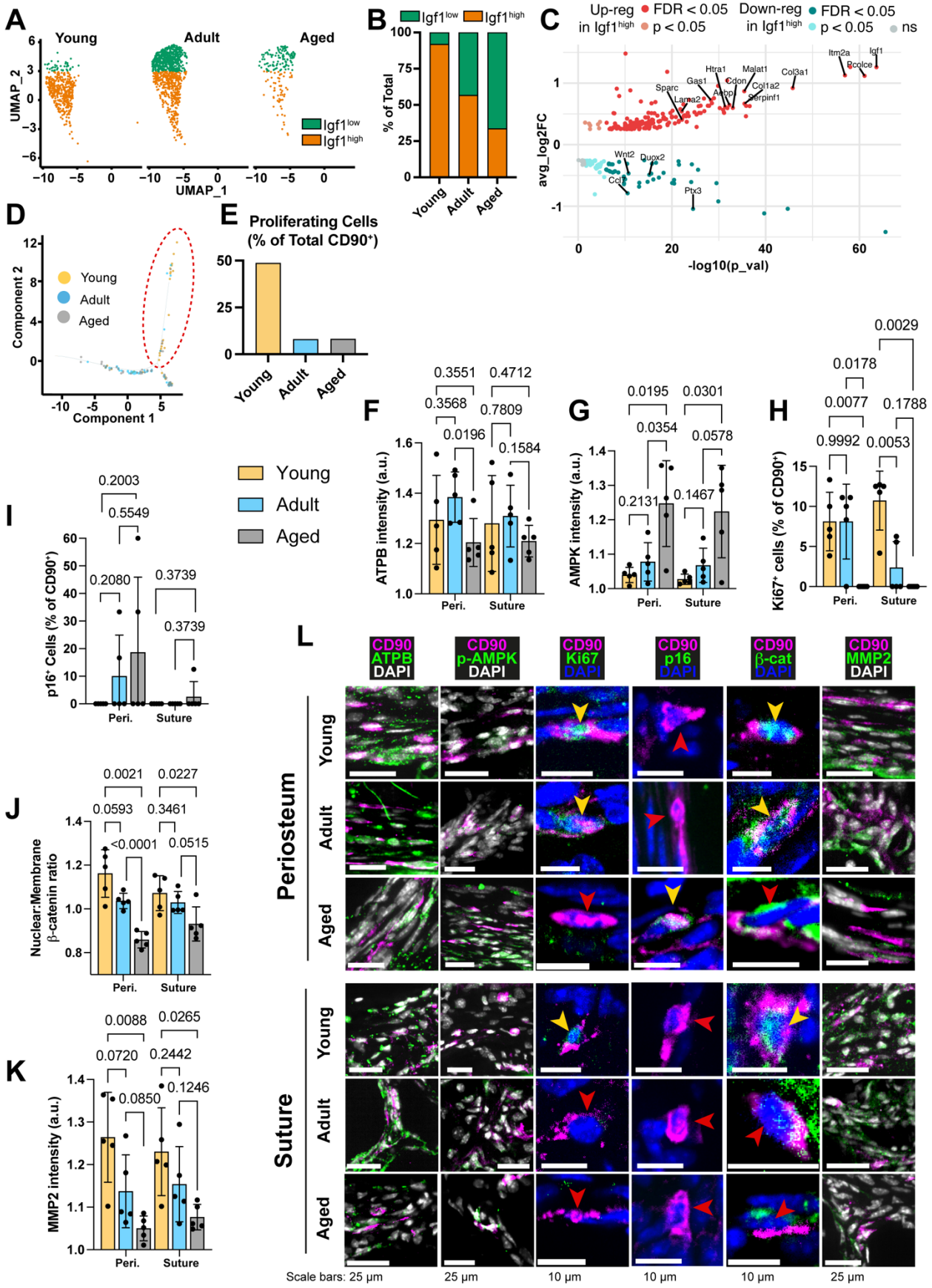
A
Young
Adult
Aged
UMAP_2
UMAP_1
Igf1low
Igf1high
B
% of Total
C
Up-reg in Igf1high
FDR < 0.05
p < 0.05
Down-reg in Igf1high
ns
avg_log2FC
-log10(p_val)
D
Component 2
Component 1
E
Proliferating Cells (% of Total CD90+)
F
ATPB intensity (a.u.)
G
AMPK intensity (a.u.)
H
Ki67+ cells (% of CD90+)
I
p16+ Cells (% of CD90+)
J
Nuclear:Membrane β-catenin ratio
K
MMP2 intensity (a.u.)
Peri.
Suture
L
CD90 ATPB DAPI
CD90 p-AMPK DAPI
CD90 Ki67 DAPI
CD90 p16 DAPI
CD90 β-cat DAPI
CD90 MMP2 DAPI
Periosteum
Suture
Scale bars: 25 µm
25 µm
10 µm
10 µm
10 µm
25 µm

619

Figure 2 Transcriptomic and protein expression characterization of CD90$^+$ cells during aging

(**A**) UMAP-plot showing the distribution of a subpopulation of CD90$^+$ periosteal cells with aging, categorized as Igf1^{high} (orange) and Igf1^{low} (green). (**B**) Percentage of the total CD90$^+$ subpopulation categorized as either Igf1^{high} or Igf1^{low}. Young: Igf1^{high} (n = 425 cells), Igf1^{low} (n = 37); Adult: Igf1^{high} (n = 553), Igf1^{low} (n = 421); Aged: Igf1^{high} (n = 61), Igf1^{low} (n = 120). (**C**) Volcano plot showing differentially-expressed genes in the comparison of all Igf1^{high} cells (n = 1039) against all Igf1^{low} cells (n = 578). Statistical analysis: Wilcoxon Rank Sum test via the FindMarkers function in the Seurat R package; upregulated (pink: $p < 0.05$; red: False discovery rate (FDR) -adjusted $p < 0.05$), downregulated (cyan: $p < 0.05$; teal: FDR-adjusted $p < 0.05$), and non-significant (ns) genes are displayed on axes of log fold expression (Igf1^{high} over Igf1^{low}) (y, avg_log2FC) against p transformed as its negative log value. (**D**) Dimensional reduction plot (Monocle package(Trapnell et al., 2014)) of suture mesenchyme CD90$^+$ populations in Young (yellow), Adult (blue), and Aged (grey) mice. (**E**) Percentage of CD90$^+$ categorized as 'proliferating' (inside red dashed ellipse) vs 'non-proliferating' (outside ellipse). Young: proliferating (n = 19 cells), nonproliferating (n = 20); Adult: proliferating (n = 5), non-proliferating (n = 57); Aged: proliferating (n = 5), nonproliferating (n = 56). (**F**) Normalized intensity staining for ATPB in CD90$^+$ cells. (**G**) Normalized intensity staining for phospho-AMPK in CD90$^+$ cells. (**H**) Proportion of CD90$^+$ cells that are Ki67$^+$. (**I**) Proportion of CD90$^+$ cells that are p16$^+$. (**J**) Ratio of Nuclear:Membrane β-catenin staining in CD90$^+$ cells. (**K**) Normalized intensity staining for MMP2 in CD90$^+$ cells. For all plots (**F**-**K**), Young (yellow), Adult (blue), Aged (grey), periosteum (3 left columns), suture mesenchyme (3 right columns), statistical testing: Welch's tests in n = 5 mice per condition. (**L**) Representative images depicting CD90 (magenta), DAPI (grey/blue as indicated by column), and functional markers (green) as indicated by column. Yellow arrows indicate marker-high/positive cells; red arrows indicate marker-low/negative cells.

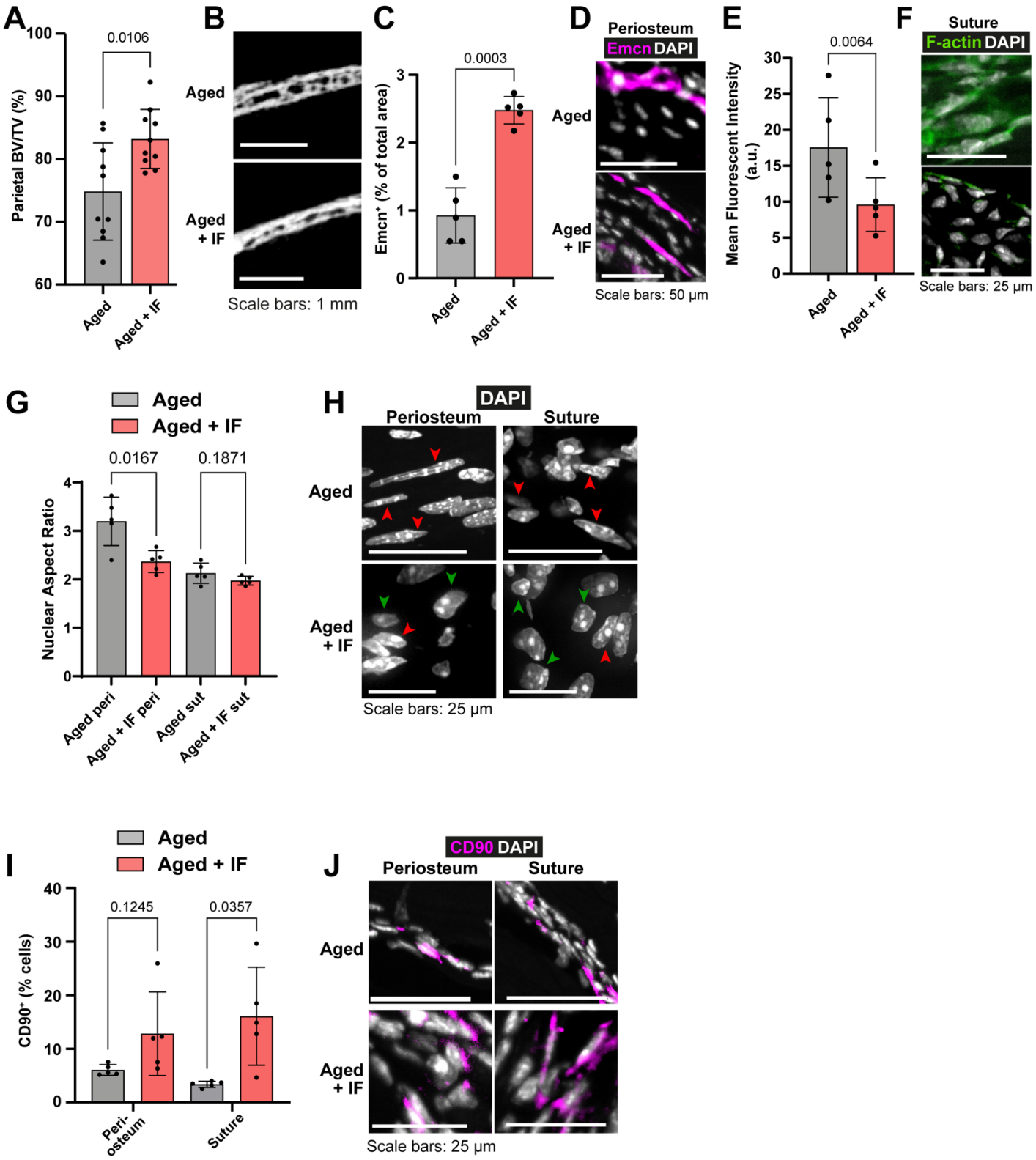

Figure 3 The impact of Intermittent Fasting on Aged bone structure and osteogenic tissues

(**A**) Parietal Bone Volume/Total Volume (BV/TV) and (**B**) representative transverse micro computed tomography (microCT) of Aged mice undergoing intermittent fasting. Statistical analysis: Welch's test in n = 10 mice per condition. (**C**) Mean cross sectional area taken up by Endomucin (Emcn)-positive vascular cells and (**D**) representative immunofluorescence staining of Emcn (magenta) and DAPI (grey) in the periosteum

650 of Aged mice undergoing intermittent fasting. Statistical analysis: Welch's tests in n = 5 mice per condition.
651 (**E**) Mean Phalloidin-488 fluorescence intensity and (**F**) representative images for filamentous actin (F-actin,
652 green) and DAPI (grey) in the suture mesenchyme of Aged mice undergoing intermittent fasting. Statistical
653 analysis: Welch's test in n = 5 mice per condition. (**G**) Nuclear aspect ratio (long axis divided by short axis) of
654 cells within the periosteum and suture mesenchyme and representative DAPI-stained nuclei (**H**) of Aged mice
655 undergoing intermittent fasting. Statistical analysis: Welch's tests in n = 5 mice per condition. Green and red
656 arrows highlight rounded and elongated nuclei, respectively. (**I**) Percentage of $CD90^+$ cells within the
657 periosteum (left columns) and suture (right columns), expressed relative to the total cellular number ($DAPI^+$)
658 in Aged mice undergoing intermittent fasting. Representative images (**J**) show CD90 immunostaining
659 (magenta) and DAPI (grey). Statistical analysis: Welch's tests in n = 5 mice.
660 In panels **A**, **C**, **E**, **G and I,** columns in grey are data previously shown in **Fig. 1**, reproduced here for reference.
661 In panels **B**, **D**, **F**, **H**, **J**, Aged control representative images previously shown in **Fig. 1** are reproduced here
662 for reference.
663

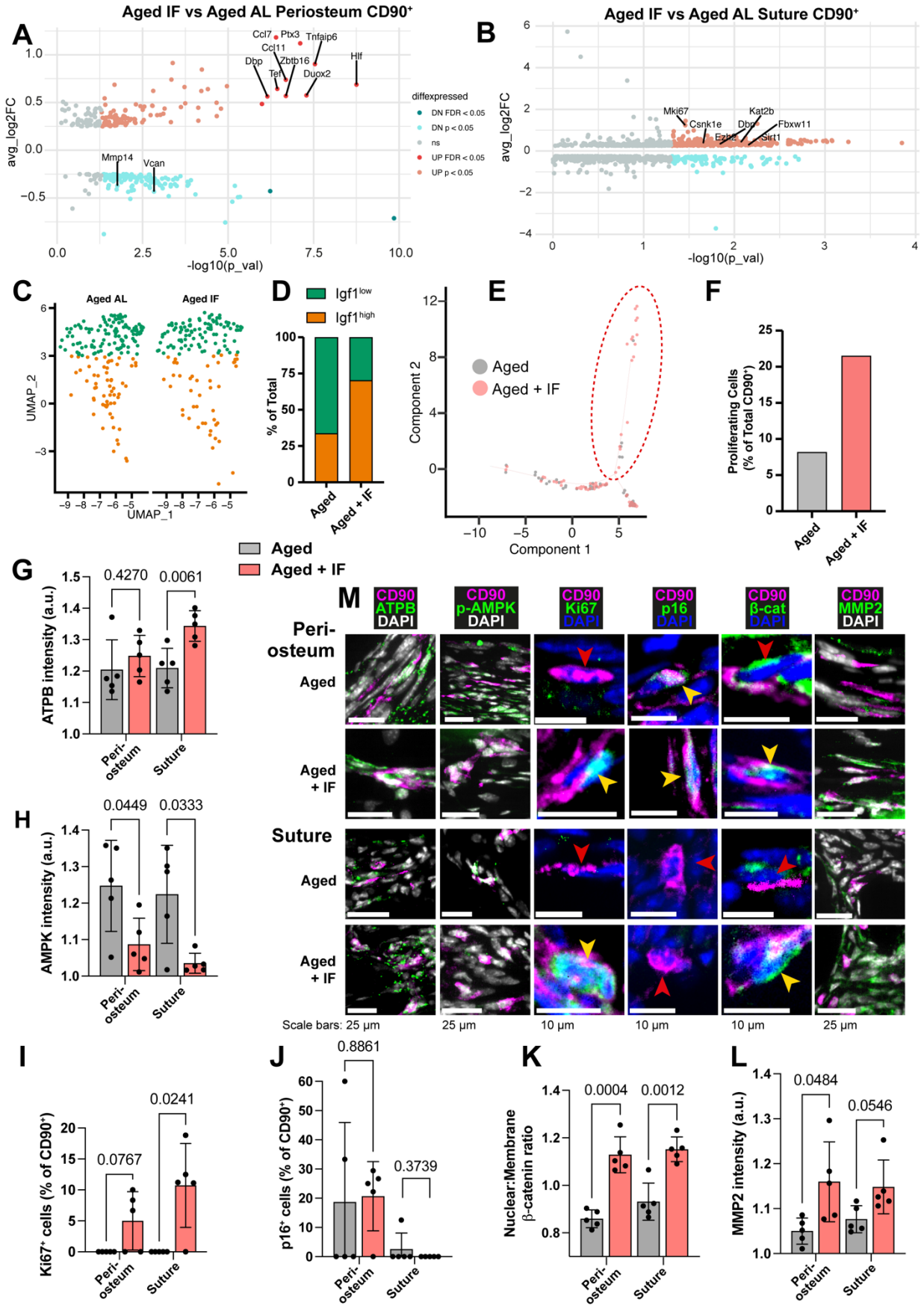
A
Aged IF vs Aged AL Periosteum CD90⁺
avg_log2FC
-log10(p_val)
Ccl7
Ptx3
Tnfaip6
Ccl11
Dbp
Zbtb16
Hlf
Tef
Duox2
Mmp14
Vcan
diffexpressed
DN FDR < 0.05
DN p < 0.05
ns
UP FDR < 0.05
UP p < 0.05
B
Aged IF vs Aged AL Suture CD90⁺
Mki67
Kat2b
Csnk1e
Dbp
Fbxw11
Ezh2
Sirt1
C
Aged AL
Aged IF
UMAP_2
UMAP_1
D
Igf1low
Igf1high
% of Total
Aged
Aged + IF
E
Aged
Aged + IF
Component 2
Component 1
F
Proliferating Cells (% of Total CD90⁺)
Aged
Aged + IF
G
ATPB intensity (a.u.)
0.4270
0.0061
Peri-osteum
Suture
H
AMPK intensity (a.u.)
0.0449
0.0333
Peri-osteum
Suture
M
CD90 ATPB DAPI
CD90 p-AMPK DAPI
CD90 Ki67 DAPI
CD90 p16 DAPI
CD90 β-cat DAPI
CD90 MMP2 DAPI
Peri-osteum
Aged
Aged + IF
Suture
Aged
Aged + IF
Scale bars: 25 μm
25 μm
10 μm
10 μm
10 μm
25 μm
I
Ki67⁺ cells (% of CD90⁺)
0.0767
0.0241
Peri-osteum
Suture
J
p16⁺ cells (% of CD90⁺)
0.8861
0.3739
Peri-osteum
Suture
K
Nuclear:Membrane β-catenin ratio
0.0004
0.0012
Peri-osteum
Suture
L
MMP2 intensity (a.u.)
0.0484
0.0546
Peri-osteum
Suture

Figure 4 Transcriptomic and protein expression characterization of Aged CD90$^+$ cells during intermittent fasting

(**A**) Volcano plot showing differentially-expressed genes in the comparison of the Aged CD90$^+$ population in the periosteum and (**B**) suture during intermittent fasting (IF) vs the ad libitum (AL) diet. Statistical analysis: Wilcoxon Rank Sum test via the FindMarkers function in the Seurat R package. Upregulated (pink: $p < 0.05$; red: FDR-adjusted $p < 0.05$), downregulated (cyan: $p < 0.05$; teal: FDR-adjusted $p < 0.05$), and nonsignificant (ns) genes are displayed on axes of log fold expression (IF over AL) (y, avg_log2FC) against p transformed as its negative log value. Periosteum: Aged IF (n = 194 cells); Aged AL (n = 242 cells). Suture: Aged IF (n = 79 cells); Aged AL (n = 61 cells). (**C**) UMAP-plot showing the distribution of a subpopulation of CD90+ periosteal cells during intermittent fasting in Adult and Aged mice. Ad libitum (AL) cells are data previously shown, reproduced here for reference. (**D**) Percentage of the total cells categorized as either Igf1^{high} or Igf1^{low}. Aged + IF: Igf1^{high} (n = 104), Igf1^{low} (n = 44). (**E**) Plot (Monocle package) of suture CD90$^+$ populations. (**F**) Percentage of CD90$^+$ categorized as 'proliferating' (inside red dashed ellipse) vs 'non-proliferating' (outside ellipse) in Aged mice undergoing intermittent fasting. Ad libitum (AL) cells and chart are data previously shown, reproduced here for reference. Statistical analysis: two-tailed binomial test based on expected observed proportions between groups. Adult + IF: proliferating (n = 30 cells), non-proliferating (n = 86); Aged + IF: proliferating (n = 17), non-proliferating (n = 62). (**G**) Normalized intensity staining for ATPB in CD90$^+$ cells. (**H**) Normalized intensity staining for phospho-AMPK in CD90$^+$ cells. (**I**) Proportion of CD90$^+$ cells that are Ki67$^+$. (**J**) Proportion of CD90$^+$ cells that are p16$^+$. (**K**) Ratio of Nuclear:Membrane β-catenin staining in CD90$^+$ cells. (**L**) Normalized intensity staining for MMP2 in CD90$^+$ cells. For all plots (**G**-**L**), Aged + IF (red), Aged control (grey), periosteum (2 left columns), suture mesenchyme (2 right columns), statistical testing: Welch's tests in n = 5 mice per condition. (**M**) Representative images depicting CD90 (magenta), DAPI (grey/blue as indicated by column), and functional markers (green) as indicated by column). Yellow arrows indicate marker-high/positive cells; red arrows indicate marker-low/negative cells. In panels **C**-**M,** data and representative images of Aged controls from previous figures are reproduced here for reference.

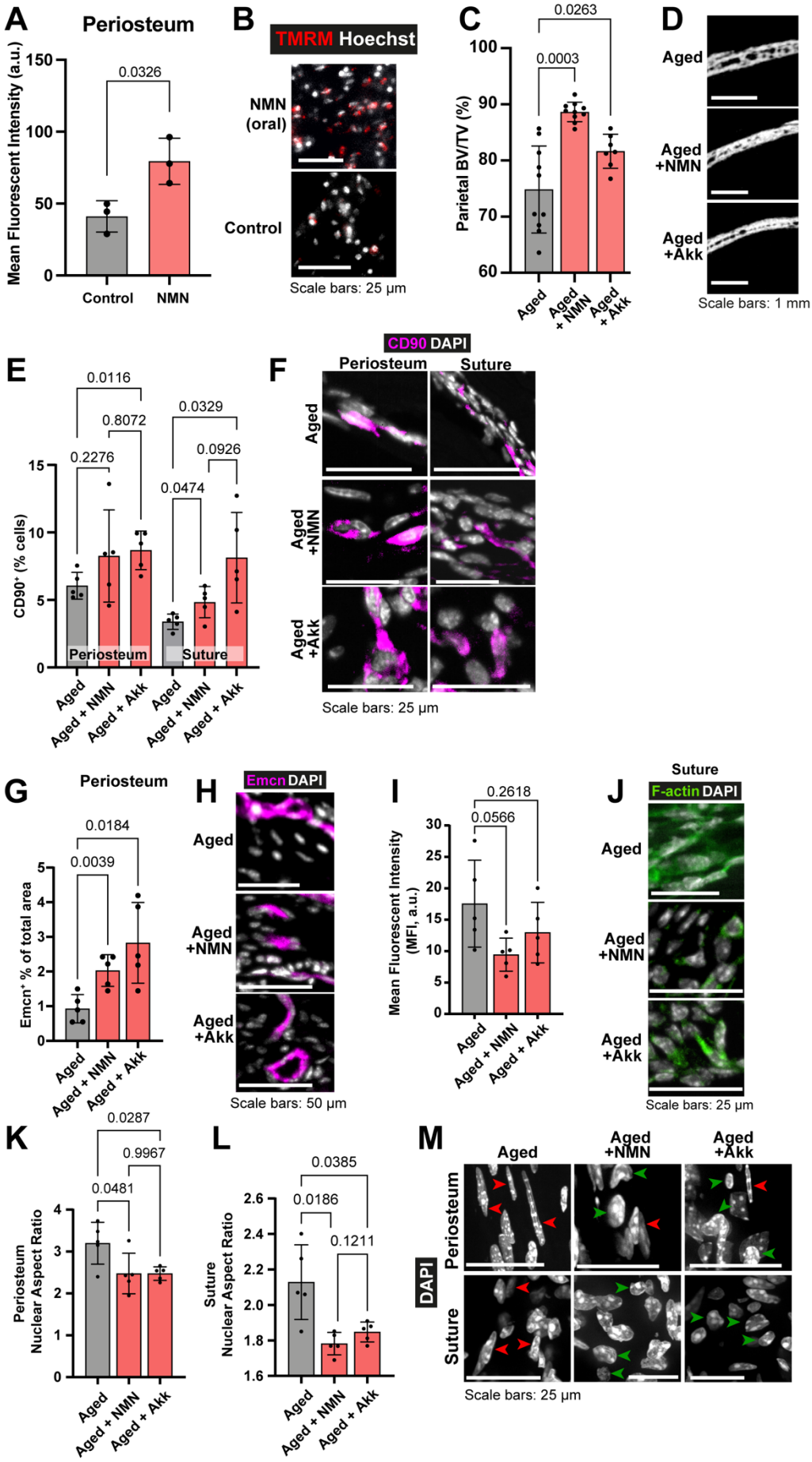
A
Periosteum
Mean Fluorescent Intensity (a.u.)
0.0326
Control
NMN
B
TMRM Hoechst
NMN (oral)
Control
Scale bars: 25 μm
C
Parietal BV/TV (%)
0.0263
0.0003
Aged
Aged + NMN
Aged + Akk
D
Aged
Aged +NMN
Aged +Akk
Scale bars: 1 mm
E
CD90⁺ (% cells)
0.0116
0.8072
0.2276
0.0329
0.0926
0.0474
Periosteum
Suture
Aged
Aged + NMN
Aged + Akk
F
CD90 DAPI
Periosteum
Suture
Aged
Aged +NMN
Aged +Akk
Scale bars: 25 μm
G
Periosteum
Emcn⁺ % of total area
0.0184
0.0039
Aged
Aged + NMN
Aged + Akk
H
Emcn DAPI
Aged
Aged +NMN
Aged +Akk
Scale bars: 50 μm
I
Mean Fluorescent Intensity (MFI, a.u.)
0.2618
0.0566
Aged
Aged + NMN
Aged + Akk
J
Suture
F-actin DAPI
Aged
Aged +NMN
Aged +Akk
Scale bars: 25 μm
K
Periosteum Nuclear Aspect Ratio
0.0287
0.9967
0.0481
Aged
Aged + NMN
Aged + Akk
L
Suture Nuclear Aspect Ratio
0.0385
0.0186
0.1211
Aged
Aged + NMN
Aged + Akk
M
Aged
Aged +NMN
Aged +Akk
Periosteum
Suture
DAPI
Scale bars: 25 μm
N
Akkermansia Abundance (%)
0.2392
Aged
Aged + IF

692

Figure 5 The impact of Nicotinamide mononucleotide (NMN) and Akkermansia muciniphila (Akk) supplementation on Aged bone structure and osteogenic tissues

(**A**) Mean intensity and (**B**) representative images of live TMRM staining (red) and Hoechst (grey) in Adult mice controls and Adult mice dosed with 600 mg/kg NMN by oral gavage, samples of periosteum *ex vivo*. Statistical analysis: Welch's test in tissue from n = 3 mice per condition. (**C**) Parietal Bone Volume/Total Volume (BV/TV) and (**D**) representative transverse micro-computed tomography (microCT) sections in Aged mice supplemented with NMN or Akkermansia. Statistical analysis: Welch's tests in n = 10 (Aged, Aged + NMN) and n = 7 (Aged + Akk) mice. (**E**) Percentage of $CD90^+$ cells within the periosteum (left columns) and suture (right columns), expressed relative to the total cellular number ($DAPI^+$) in Aged mice supplemented with NMN or Akkermansia. Representative images (**F**) show CD90 immunostaining (magenta) and DAPI (grey). Statistical analysis: Welch's tests in n = 5 mice per condition. (**G**) Mean cross sectional area taken up by Endomucin (Emcn)-positive vascular cells and (**H**) representative immunofluorescence staining of Emcn (magenta) and DAPI (grey) in the periosteum of Aged mice supplemented with NMN or Akkermansia. Statistical analysis: Welch's tests in n = 5 mice per condition. (**I**) Mean Phalloidin-488 fluorescence intensity and (**J**) representative images for filamentous actin (F-actin, green) and DAPI (grey) in the suture mesenchyme of Aged mice supplemented with NMN or Akkermansia. Statistical analysis: Welch's tests in n = 5 mice per condition. (**K-M**) nuclear aspect ratio (long axis divided by short axis) of cells within the (**K**) periosteum and (**L**) suture in Aged mice supplemented with NMN or Akkermansia, and (**M**) Representative DAPI-stained nuclei. Statistical analysis: Welch's tests in n = 5 mice per condition. Green and red arrows highlight rounded and elongated nuclei, respectively. (**N**) The relative abundance of bacteria identified as genus Akkermansia in 16S metagenomic profiling of Aged mice undergoing intermittent fasting vs. Aged controls. Statistical analysis: Welch's test in (Aged, n = 3; Aged + IF, n = 4) mice per condition. In panels **C-M**, data and representative images of Aged controls from previous figures are reproduced here for reference.

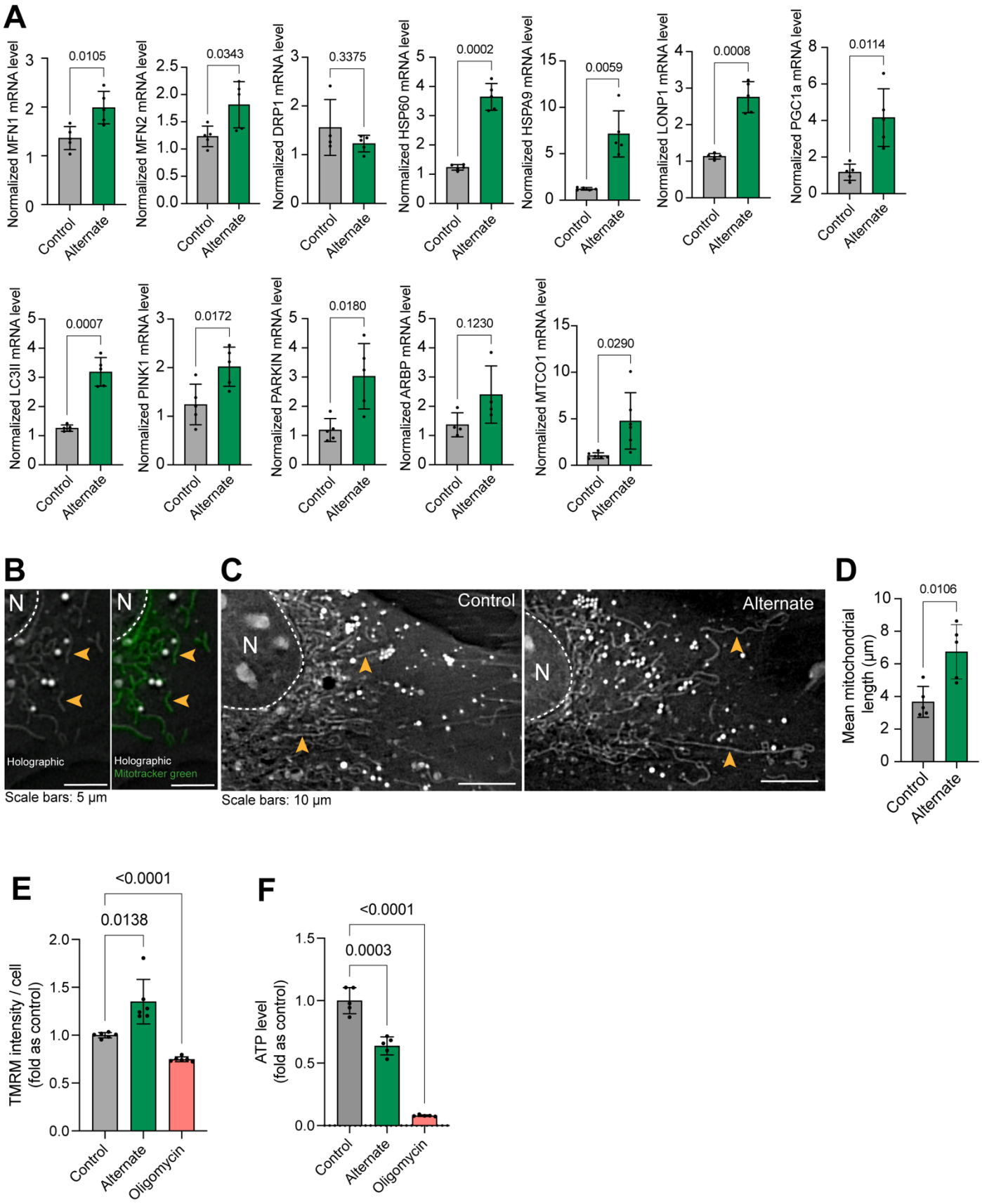
A
Normalized MFN1 mRNA level
0.0105
Normalized MFN2 mRNA level
0.0343
Normalized DRP1 mRNA level
0.3375
Normalized HSP60 mRNA level
0.0002
Normalized HSPA9 mRNA level
0.0059
Normalized LONP1 mRNA level
0.0008
Normalized PGC1a mRNA level
0.0114
Normalized LC3II mRNA level
0.0007
Normalized PINK1 mRNA level
0.0172
Normalized PARKIN mRNA level
0.0180
Normalized ARBP mRNA level
0.1230
Normalized MTCO1 mRNA level
0.0290
Control
Alternate
B
N
Holographic
Mitotracker green
Scale bars: 5 µm
C
Control
Alternate
Scale bars: 10 µm
D
Mean mitochondrial length (µm)
0.0106
E
TMRM intensity / cell (fold as control)
<0.0001
0.0138
Oligomycin
F
ATP level (fold as control)
<0.0001
0.0003

720 **Figure 6 Effect of hour-based alternate serum deprivation on mitochondria in MC3T3 cells in glucose-**
721 **free media.**
722 (**A**) Effect of alternate serum deprivation on gene expression implied in mitochondrial dynamics (MFN1, MFN2,
723 DRP1), unfolded protein response (mtUPR) (HSP60, HSPA9, LonP1), biogenesis (PGC1a), structure (ARBP),
724 mitophagy (LC3II PINK1, PARKIN), and mitochondrial respiratory complex IV (MTCO1). Statistical analysis:
725 Welch's test, n≥4/group. (**B**) Representative holographic images of mitochondrial shape (orange arrowheads),
726 confirmed by Mitotracker green staining. (**C-D**) Effect of alternate serum deprivation on mitochondrial length.
727 Statistical analysis: Welch's t-test of n=5/group, total mitochondria=425. (**E**) Effect of alternate serum
728 deprivation and oligomycin on mitochondrial membrane potential. Statistical analysis: Welch's t-test of
729 n=6/group with at least 481 cells/group. (**F**) Effect of alternate serum deprivation and oligomycin on ATP level.
730 Statistical analysis: Welch's t-test of n≥5/group.
731

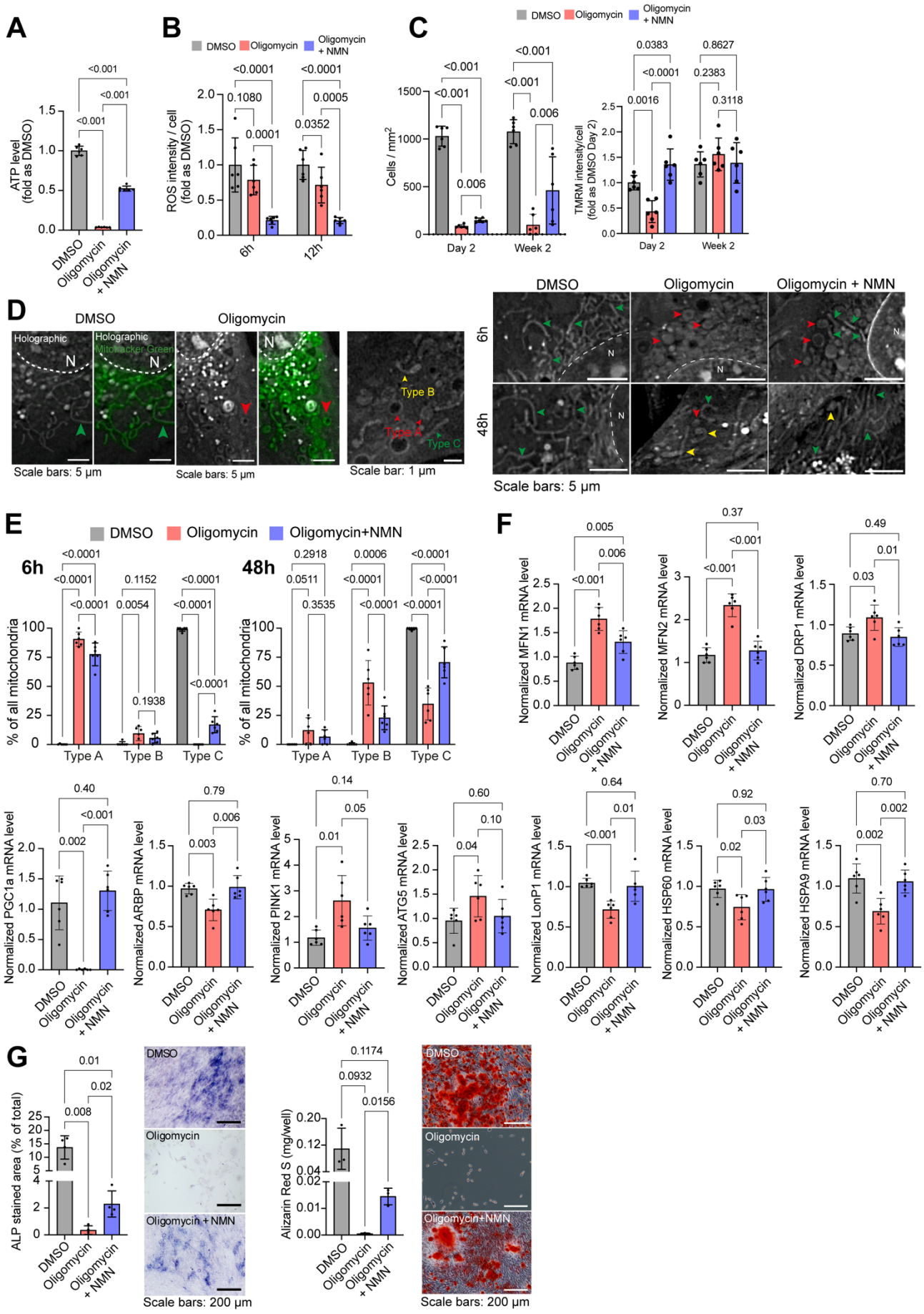
A
ATP level (fold as DMSO)
DMSO
Oligomycin
Oligomycin + NMN
B
ROS intensity / cell (fold as DMSO)
6h
12h
C
Cells / mm²
Day 2
Week 2
TMRM intensity/cell (fold as DMSO Day 2)
D
Holographic
Mitotracker Green
N
Type A
Type B
Type C
Scale bars: 5 µm
Scale bar: 1 µm
6h
48h
Scale bars: 5 µm
E
Oligomycin+NMN
% of all mitochondria
F
Normalized MFN1 mRNA level
Normalized MFN2 mRNA level
Normalized DRP1 mRNA level
Normalized PGC1a mRNA level
Normalized ARBP mRNA level
Normalized PINK1 mRNA level
Normalized ATG5 mRNA level
Normalized LonP1 mRNA level
Normalized HSP60 mRNA level
Normalized HSPA9 mRNA level
G
ALP stained area (% of total)
Alizarin Red S (mg/well)
Oligomycin + NMN
Scale bars: 200 µm

732

Figure 7 Effect of NMN on oligomycin-induced mitochondrial damage in glucose-free MC3T3 cells. (**A**) Effect of oligomycin ± NMN on ATP level in MC3T3 cells. Welch's test, n=6/group. (**B**) Effect of oligomycin ± NMN on ROS level MC3T3 cells. Welch's test, n=6/group. (**C**) Effect of oligomycin ± NMN on cell density (left) and mitochondrial membrane potential (right) over time in MC3T3. Welch's test, n=6/group. (**D**) Representative images of mitochondrial shape alteration by oligomycin exposure ± NMN supplementation. Dashed white line = nuclear membrane, N = nucleus. Observation by holotomography (grey levels) and confirmed with Mitotracker Green (green). Red arrowheads = Type A ("round"), yellow arrowheads = Type B ("intermediate"), and green arrowheads = Type C ("rod-like/filamentous") mitochondria. (**E**) Quantification of the effect of oligomycin ± NMN on mitochondrial shape. Each data point is a cell with at least 30 mitochondria. Welch's test n = 6 cells / group, total mitochondria=1821. (**F**) Effect of oligomycin ± NMN on gene expression implied in mitochondrial dynamics (MFN1, MFN2, DRP1), biogenesis (PGC1a), structure (ARBP), mitophagy (PINK1, ATG5), and unfolded protein response (mtUPR) (LonP1, HSP60, HSPA9). Welch's test, n≥5/group. (**G**) Effect of oligomycin ± NMN on osteoblastic differentiation. Staining of alkaline phosphatase (ALP) activity and mineralization (Alizarin Red S; ARS) of the matrix after two weeks of differentiation. Welch's test, n=4 (ALP) or 3 (ARS) / group.

Methods

Wnt3a bandage manufacture

Polycaprolactone (PCL)-based polymer film (Poly-Med) was plasma-treated using a plasma etching electrode in oxygen gas at a flow of 20 $cm^3 min^{-1}$ with a radio frequency plasma generator (frequency 13.56 MHz, power 50 W, Diener electronic Zepto-W6) at 0.2 mbar pressure for 3 min. Treated films were immediately incubated in 5% (3-Aminopropyl)triethoxysilane (APTES, Sigma, 440140) in ethanol (dark, room temperature, 2 hours), before washing twice with 100% ethanol (room temperature, 10 minutes), and allowed to air dry. Circular bandages were cut using a 5mm biopsy punch (Stiefel) and placed in 10 mg/ml succinic anhydride (Sigma Aldrich, 239690-50G) in 0.4M borate buffer (Sigma Aldrich, B7660) pH=9 (room temperature, 30 minutes). Bandages were twice washed in 25mM Morpholineethanesulfonic acid (MES) buffer pH 5 (Sigma Aldrich, M3671), then incubated in a MES buffer solution containing 50 mg/ml N(3Dimethylaminopropyl)-N′-ethylcarbodiimide hydrochloride (EDC, Sigma Aldrich, E7750) and 50 mg/ml NHydroxysuccinimide (NHS, Sigma Aldrich, 56480) (room temperature, 30 minutes), and washed twice again in MES buffer. Bandages are individually placed on a sterile flat surface and briefly allowed to air-dry. 300ng Wnt3a (R&D, 1324-WN-010) was diluted to 23 µL in MES buffer, and this liquid added as a droplet on top of the bandage for 1 hour at room temperature.

For inert control bandages (inactive-bandages), the bandages were then placed into a 96 well plate and washed with PBS. 20 mM Dithiothreitol (DTT, Roche, 10197777001) in 50 µL ddH_2O was then added and incubated (37℃, 30 minutes). Active Wnt3a-bandages were also placed in the 96 well plate, and then all bandages were washed with PBS, and quenched with 2% Fetal Bovine Serum (FBS, Sigma Aldrich, F7524) in Dulbecco's Modified Eagle Medium (DMEM, Thermo Fisher, 41966) (room temperature, 15 minutes) in preparation for their surgical implantation.

Wnt3a-bandage testing

The Wnt/β-catenin pathway activation of Wnt3a-bandages was confirmed as previously published (Lowndes et al. 2017). Wnt3a-bandages were tested for Wnt/β-catenin pathway activation using Comma-D Beta cells harboring GFP expression under the control of a TCF-LEF promoter (Lowndes et al. 2016) (**Supplementary Fig. 3a, c**). Similarly, LS/L cells harboring luciferase under control of a 7xTCF promoter were used to quantitatively test Wnt3a-bandages, as described previously (Okuchi et al. 2021) (**Supplementary Fig. 3b**).

780 **Animal husbandry/housing**
781 Female C57BL6/J mice (Charles River, strain 632) were housed in conditions that comply with the Animals
782 (Scientific) Procedures Act 1986 (ASPA). Mice were group housed (2-5 mice/cage) under 7am-7pm lighting
783 and fed with standard mouse food pellets (Lab diet Picolab Rodent Diet 20 EXT Irradiated). During intermittent
784 fasting, food was removed from cages at 10am on Monday, Wednesday, and Friday, and returned at 10am
785 on Tuesday, Thursday, and Saturday, such that the maximum time without food was 24 hours. Intermittent
786 fasting started the day after the surgery and was performed for 10 weeks.
787
788 **Calvarial Defect**
789 All steps of surgery were carried out under aseptic conditions. Mice were intraperitoneally anaesthetized with
790 10 µL/g bodyweight of anesthesia cocktail (7.5 mg/ml Ketamine hydrochloride (Ketavet) and 0.1 mg/ml
791 Medetomidine hydrochloride (Domitor) in 0.9% sterile saline). Loss of consciousness was confirmed with lack
792 of pedal and tail reflexes. The top of the head was shaved, cleaned, and prepared for surgery, before a ~8
793 mm central incision was made in the skin with surgical scissors. The periosteum was gently pushed towards
794 the outer edges of the calvaria, and the location of the sutures noted. A 2 mm diameter full thickness defect
795 was drilled into the middle of the parietal bone on both sides of the skull, ensuring irrigation was applied to
796 limit heat buildup. A small amount (~10 µL) of 1 mg/ml collagen gel (Corning, 354249) (diluted with DMEM
797 and set with 3 mM sodium hydroxide (Sigma Aldrich, S5881)) was placed into the defect to exclude trapped
798 air, and the required bandages were placed face down over the defect. Small dots of glue (3M, Vetbond) were
799 applied at the edges of the bandages to affix them to the surface of the skull. The skin was then approximated
800 and glued to ensure closure of the wound. Mice were administered 10 µL/g bodyweight of the recovery cocktail
801 intraperitoneally (0.125 mg/ml Atipamezole hydrochloride (Antisedan) and 0.01 mg/ml Buprenorphine
802 hydrochloride (Vetergesic) in 0.9% sterile saline) and placed in a warmed cage (35 ℃). Mice typically became
803 conscious within 20 minutes, began moving around the cage within 40 minutes, and were feeding within 2
804 hours. Mice showed no signs of distress or pain the following day and were externally monitored daily for the
805 healing of the skin wound. Following surgery, mice were maintained under standard conditions for 10 weeks,
806 and group housed (2-5 mice/cage) where possible.
807
808 **NMN supplementation**
809 600 mg/kg bodyweight doses of β-nicotinamide mononucleotide (NMN, APExBIO, B7878), dissolved in water
810 were given by flexible-tipped oral gavage 3 times per week, not on consecutive days, from 2 weeks before
811 surgery to 2 weeks after, a total of 4 weeks.
812
813 **Anaerobic Culture of *Akkermansia muciniphila***
814 Preserved *Akkermansia muciniphila* (Collection de l'Institut Pasteur, CIP107961T) was resuspended and
815 cultured in Gifu's Anaerobic Medium (GAM) broth (Nissui Pharmaceutical, 05422) in an anaerobic
816 environment (80% Nitrogen, 10% Carbon dioxide, 10% Hydrogen). Aliquots were cryopreserved in 50%
817 glycerol (Sigma Aldrich, G2025) in PBS. Post-thawing viability was determined by serial dilution of
818 cryopreserved aliquots, plating onto GAM-Agar (Sigma Aldrich, 01916) plates, and 24-hour anaerobic culture.
819
820 ***Akkermansia muciniphila* supplementation**
821 Cryopreserved doses of 2.0 x 10^8 C.F.U. *Akkermansia muciniphila* were warmed to ~ 30℃ and administered
822 to Aged mice by flexible-tipped oral gavage 3 times per week, not on consecutive days, from 2 weeks before
823 surgery to 6 weeks after, a total of 8 weeks.
824

825 **Microbiome Profiling**
826 Feces samples were freshly collected and snap-frozen in liquid nitrogen. Samples were submitted for full
827 length (V1-V9) 16S metagenomic profiling. Amplification with KAPA HiFi HotStart ReadyMix PCR Kit (KAPA)
828 and 16S barcode primers (PacBio) preceded library preparation SMRTbell Express Template Prep 2.0
829 (PacBio). Samples were sequenced via the Illumina MiSeq to generate amplicon sequence data specifying
830 the V3-V4 regions of the 16S rRNA ribosomal subunit. The metagenomic analysis was conducted using the
831 amplicon sequence variant (ASV) method of taxonomic classification facilitated by DADA2 (Callahan et al.
832 2016) incorporated by the Qiime2 package (Bolyen et al. 2019). Quality control metrics of the amplicon data
833 was visualized by FastQC (Andrews S. 2015). The data was cleaned, via removal of adapters and low quality
834 sequences, using Trimmomatic (Bolger et al. (2014)) and Qiime2.
835
836 **Ethical Approval for animal experimentation**
837 All procedures involving animals were carried out by holders of Personal Licences (PIL) under a Project
838 Licence (PPL, P8F273FDD, S.J.H.) shaped by ARRIVE and NC3Rs guidelines. The PPL was approved by
839 the Animal Welfare and Ethical Review Body (AWERB) at King's College London and granted by the Home
840 Office under the Animals (Scientific) Procedures Act 1986 (ASPA) and Amendment Regulations 2012.
841
842 **Micro-Computed Tomography**
843 Mice were culled by cervical dislocation and their tissues immediately collected. Whole calvarial samples were
844 fixed in 4% PFA (room temperature, overnight) and washed in PBS. Fixed samples were scanned on a μCT50
845 micro-CT scanner (Scanco) in 19 mm scanning tubes, using voxels of side length 10 μm, X-ray settings of
846 70 kVp and 114 μA and using a 0.5 mm aluminum filter to attenuate harder X-rays. Scans were reconstructed
847 and calibrated using known densities of hydroxyapatite (HA) between 0 and 790 mg HA cm^{-3}, with absorption
848 values expressed in Hounsfield Units (HU). 3D volumes were constructed from raw data in SCANCO
849 Visualizer 1.1, and signal of less than 250 mg HA cm^{-3} was considered non-mineralized and was set as the
850 black level in displayed images.
851
852 **Sample Processing and Cryosectionning**
853 Fixed samples were decalcified in 10% formic acid (room temperature, overnight), then washed in PBS.
854 Dehydration was carried out in 30% sucrose/PBS (room temperature, overnight), followed by 30%
855 sucrose/30% OCT/PBS (room temperature, overnight). Samples were embedded in 100% OCT solidified with
856 dry ice and stored at -80℃. Cryosections were cut at 14 μm thickness using a cryostat microtome at 23℃. Cut
857 sections were stored at -20℃.
858
859 **Fluorescence Immunostaining**
860 Sections were rehydrated to ddH_2O. Antigen retrieval was performed with 0.05% v/v Tween-20 (Sigma Aldrich,
861 P9416) in 10 mM Tris (Sigma Aldrich, 93362), 1 mM EDTA (Sigma Aldrich, E6758), pH=9.0 (40℃, 30 minutes).
862 Sections were then permeabilized with 0.1% Triton-X (Sigma Aldrich, X100) in 1% Bovine Serum Albumin
863 (BSA, Sigma Aldrich, A2153) in phosphate buffered saline (PBS, Sigma Aldrich, P4417) (1% BSA/PBS) (room
864 temperature, 5 minutes), washed with 1% BSA/PBS, and individual staining regions were designated with
865 hydrophobic delimiting pen (Agilent, S200230-2).
866 Primary antibodies were diluted in 0.05% Triton-X in 1% BSA/PBS and incubated in a humid chamber (4℃,
867 overnight). Triplicate washes of 0.1% Triton-X in 1% BSA/PBS were carried out (room temperature, 10
868 minutes). Secondary antibodies were diluted in 0.05% Triton-X in 1% BSA/PBS, with 5 μg/ml DAPI (Sigma
869 Aldrich, D9542), and 1:400 dilution Phalloidin-488 (Thermo Fisher, A12379) and incubated in a humid
870 chamber (room temperature, 1 hour). Triplicate washes of 0.1% Triton-X in 1% BSA/PBS were carried out
871 (room temperature, 10 minutes) before mounting with aqueous mounting media (Abcam, ab128982).

Immunostained sections were imaged with an inverted spinning disk confocal microscope (Nikon, NISElements Viewer 5.2 software). Optimal z-axis step size was determined according to the Nyquist criteria for sampling. Images were post-processed and analyzed through ImageJ/FIJI.

Primary antibodies

Anti-Endomucin (Emcn) 1:100 (Santa Cruz, sc-65495)
Anti-CD90/Thy1, 1:100 (Abcam, ab3105)
Anti-phosphoAMPK (Thr183, Thr172), 1:100 (Thermo Fisher, 44-1150G)
Anti-ATPB, 1:100 (Abcam, ab128743)
Anti-Ki67, 1:100 (Thermo Fisher, MA5-14520)
Anti-p16INK4a, 1:100 (Abcam, ab211542)
Anti-beta-catenin 1:100 (Abcam, ab32572)
Anti-MMP2, 1:100 (Abcam ab92536)
Anti-CD31, 1:100 (Novus Biologicals, NB100-2284)

Secondary antibodies

Chicken anti-Rat-647 1:1000 (Thermo Fisher, A21472)
Donkey anti-Rabbit-555 1:1000 (Thermo Fisher, A32816)

Fluorescence thresholding quantification

See *Supplementary Figure 1a*. Sample tissue sections were immunostained alongside controls that lacked primary antibody: the 'no primary control'. These control samples were imaged using the same microscope settings as the experimental samples, and maximum projections were calculated to reduce volumetric images to 2D. The maximum pixel intensity in the control images was used to threshold the experimental samples, thereby excluding signal arising from non-specific staining by fluorescent secondary antibodies. Cellular localization of the remaining signal allowed designation of cells positive and negative for the antibody targets of interest.

For quantitative measurements of F-actin/Phalloidin-488 signal intensity (e.g. Figure 1h), sum-projections were taken to reduce volumetric 3D images to 2D space. In these quantifications, mean sum pixel intensity was measured and the mean sum background pixel intensity subtracted for $N \geq 56$ cells in $n = 3$ mice.

Tetramethylrhodamine (TMRM) & Hoechst staining in live tissue *ex vivo*

Periosteum was dissected from n = 3 freshly killed mice, and immediately placed in warmed culture media (10% FBS in DMEM) containing 100 nM TMRM (Thermo Fisher, I34361) and 5 µg/mL Hoechst 33342 (Thermo Fisher, H3570) for 30 minutes at 37℃. Tissue was briefly washed with fresh warmed media and imaged on a Zeiss widefield microscope (Zeiss Zen Blue Edition 2.5 software). Explanted cell controls were allowed to migrate from minced suture mesenchyme and attach for 24 hours before identical TMRM/Hoechst staining.

MC3T3 cell culture

MC3T3 cells were cultured in MEMα (Thermofisher, A1049001) 10% foetal bovine serum (FBS; Thermofisher A5256701), 1% penicillin-streptomycin (PS; Thermofisher, 15140-122). Cells were used at passages 13-20 and seeded at 25,000 cells / cm^2 for further experiments in glucose- and pyruvate-free DMEM (Thermofisher, 11966025), 10% FBS, 1% PS. All experiments were conducted in differentiation medium, consisting of glucose- and pyruvate-free DMEM 10% FBS, 1% PS, 50 µM ascorbic acid (Merck, 5960), and 2 mM glycerophosphate (Merck, 50020). Alternate serum deprivation was performed by replacing the osteogenic media by serum-free osteogenic media every 1h for 6h. For oligomycin and NMN treatments, cells were treated by 0.1 µM oligomycin (Merck, 75351), with or without 1 mM β-nicotinamide mononucleotide (NMN;

APExBio, B7878), or with 0.1% DMSO (Merck, D2438), the vehicle of oligomycin. Cells were treated for 6h before switching to differentiation medium ("oligomycin" or "DMSO" condition)or differentiation medium + 1 mM NMN ("oligomycin + NMN" condition). The media were changed twice a day.

Inhibition of ATP production in MC3T3 and measure of Reactive Oxygen Species (ROS) production

ATP level in cells was measured in 96 well plates after 6h of the treatment induction, using the CellTiter-Glo® 2.0 Assay (Promega, G9241) according to manufacturer's instructions. ROS production was measured in live cells using the CellROX deep red staining kit (Thermofisher, C10422) using a spinning disk microscope (Nikon Ti2, Crest Optics X-Light V3), with the sum projection intensity normalized by the number of cells using Hoechst staining (Fisherscientific, 11544876).

MC3T3 count and mitochondrial activity

Cell count and mitochondrial activity were measured with Hoechst and TMRM staining (Thermofisher, I34361) respectively, using a spinning disk microscope and according to manufacturer's instructions. Z-stacks of 20 µm were acquired and the TMRM sum intensity was normalized to the cell number.

Holographic imaging

Mitochondrial morphology was observed using holotomography imaging on live cells (Tomocube, HT-X1), with a reference refractive index set at 1.337. After reconstruction of the images, mitochondria were categorized in three types according to their shape.The proportion of each morphology type was determined with Tomo Analysis and Fiji softwares. MitotrackerGreen (Thermofisher, M7514) was used to stain mitochondria and confirm the mitochondrial morphology obtained by holotomography.

RT-qPCR

RNA was extracted 12h after the treatment induction (Marchery-Nagel, M36006) according to manufacturer's instructions. Reverse transcription (Thermofisher, 4374966) and qPCR (Thermofisher, 4368706) were performed according to manufacturer's instruction and mRNA target levels were normalised by beta-Actin mRNA levels using the $2^{-\Delta\Delta Ct}$ method. The following primer have been used (5'→ 3'): *MFN1*: F-AACTTGATCGAATAGCATCCGAG, R-GCATTGCATTGATGACAGAGC; *MFN2*: F-CTGGGGACCGGATCTTCTTC, R-CTGCCTCTCGAAATTCTGAAACT; *DRP1*: F-GGGCACTTAAATTGGGCTCC, R-TGTATTCTGTTGGCGTGGAAC; *PGC1a*: F-AGTGGTGTAGCGACCAATCG, R-AATGAGGGCAATCCGTCTTCA; *ARBP*: F-AGATTCGGGATATGCTGTTGG , R-AAAGCCTGGAAGAAGGAGGTC; *PINK1*: F-CACACTGTTCCTCGTTATGAAGA, R- TTGAGATCCCGATGGGCAAT; *PARKIN*: F-GAGGTCCAGCAGTTAAACCCA; R-CACACTGAACTCGGAGCTTTC; *LC3II* F-TTATAGAGCGATACAAGGGGGAG, R-CGCCGTCTGATTATCTTGATGAG; *ATG5*: F-AAGTCTGTCCTTCCGCAGTC, R-TGAAGAAAGTTATCTGGGTAGCTCA; *LONP1*: F-ATGACCGTCCCGGATGTGT, R-CCTCCACGATCTTGATAAAGCG; *HSP60*: F-CACAGTCCTTCGCCAGATGAG, R-CTACACCTTGAAGCATTAAGGCT; *HPSA9*: FAATGAGAGCGCTCCTTGCTG, R-CTGTTCCCCAGTGCCAGAAC;; MTCO1: F-TATGTTCTATCAATGGGAGC, R-GTAGTCTGAGTAGCGTCGTG.

Evaluation of the osteoblastic differentiation

Cells were cultured for 2 weeks before the staining of the alkaline phosphatase (ALP; Abcam, ab284936) or mineralized matrix using alizarin red S (ARS; 2% solution in H_2O) (Merck, A5533). ALP staining was performed as per manufacturer's recommendation, and the stained area were quantified using Fiji on pictures taken under a light microscope. For ARS staining the cells were fixed with 4% paraformaldehyde in PBS, stained by ARS then imaged using a light microscope. The stained mineralized matrix was then dissolved with 10% (v/v) acetic acid in H_2O and optical density was measured at 405 nm to quantify the amount of dissolved ARS.

970 **Statistical analysis**
971 Statistical analysis was performed in Graphpad Prism 9. All data are plotted as mean, with error bars indicating
972 standard deviation. Typically, experimental data was analyzed from all mouse conditions together using one-
973 way ANOVA, with individual comparisons between conditions/regions of interest displayed on figures as
974 Welch's two-tailed unpaired tests. Welch's ANOVA was used instead of ordinary ANOVA because it is more
975 conservative and reduces the risk of false-positive p-values. Two-factors comparisons were analyzed with
976 two-way ANOVA with uncorrected Fisher's LSD test. Only the statistical values for the hypotheses being tested
977 are shown; multiple comparison corrections were not applied. Ratio-paired two-tailed t-test was used in
978 comparisons within the same mouse (i.e., comparisons of Wnt3a-bandage vs Inactive-bandage). Correction
979 of multiple comparison was not applied as each p-value was considered for itself. On some tested groups,
980 correction for multiple comparison did not change our general conclusions. Uncorrected Dunn's tests were
981 performed for the statistical analysis of UCell gene-expression signature scoring, as a non-parametric test for
982 non-Gaussian distributions of data.
983
984 **RNAseq sample processing**
985 Periosteum and suture mesenchyme was separately dissected and pooled from ≥ 3 live mice from each
986 condition, briefly minced with a scalpel blade, and immediately placed in 250 µL of a solution of 0.5 mg/ml
987 Liberase TL (Roche, 05401020001) and 0.1 mg/ml DNaseI (Sigma Aldrich, DN25) in Hanks' Balanced Salt
988 Solution (HBSS, Gibco, 14170-120) and incubated for 25 minutes at 37℃ with shaking (600 rpm). The
989 digestion was quenched with ice-cold 1mL buffer (3% FBS in PBS), passed through a 100 µm cell strainer
990 (Corning, 352360), and centrifuged (500 g, 5 minutes, 4℃). The supernatant was removed, and the cell pellet
991 gently resuspended in staining solution containing 0.1 µg 'hashtag' antibody, 50 µM DRAQ5 (Invitrogen, 65-
992 0880-92), and 1:4000 DAPI in ice-cold 3% FBS/PBS. Up to 4 samples were individually stained with
993 TotalSeq™ antibodies 1-4 (Biolegend 155801, 155803, 155805, 155807). Samples were centrifuged, washed
994 with 3% FBS/PBS, centrifuged again and resuspended in 3% FBS/PBS for single-cell FACS. The gating
995 strategy took single (by forward and side scatter), nucleated ($DRAQ^+$), live ($DAPI^-$) cells, and up to 4
996 individually-hashtagged samples were multiplexed together by sorting equal cell numbers into the same
997 collection tube, and stored on ice to preserve viability. Cells were loaded onto a 10X Chromium controllers
998 and the library generated through single cell 10X 3' v3.1 gene expression. All libraries were sequenced
999 together using NextSeq 2000 sequencing on a P3 flow cell.
1000
1001 **RNAseq data processing**
1002 Initial alignment and processing were performed through the CellRanger pipeline. Further quality control,
1003 processing, and analysis was carried out through the Seurat (v4) package (Hao et al. 2021) and additional
1004 packages in R software (R Core Team (2022), v4.2.1). Cells were graded for proportion of mitochondrial
1005 genes, and this metric regressed. The immune cell CD45+ populations in the samples ($Ptprc^{high}$) were
1006 removed from downstream analyses. $CD90^+/CD45^-$ ($Thy1^{high}/Ptprc^{low}$) clusters were considered the
1007 populations of interest. Differential expression of lincRNA Gm42418 was identified as an artefact and removed
1008 from the data, as has been done in other studies (Kimmel et al. 2019). For calculation of Gene Ontology (GO)
1009 and KEGG enrichment of sets of differentially expressed genes, ShinyGO 0.76.3 (Ge, Jung, and Yao 2020)
1010 was used to calculate false discovery rate (FDR) and fold enrichment (FE) values. Full details of differentially
1011 expressed genes in comparisons between ages, diets, and $CD90^+$ subpopulations are available in Source
1012 data_RNAseq tables.
1013 To construct the senescence signature, we obtained mouse aging-related genes from the GenAge database
1014 (https://genomics.senescence.info/genes/search.php?organism=Mus+musculus&show=4). The genes were
1015 categorized into two groups: positively regulated and negatively regulated. Positively regulated genes are
1016 defined as those with high expression levels associated with senescence, while negatively regulated genes

are defined as those with low expression levels associated with senescence. The genes were clustered based on their expression, then we selected the highly expressed cluster in the positively-regulated genes and the poorly expressed cluster in negatively-regulated genes in the Aged group.
For the glycolysis and lipid catabolic processes signatures, we obtained mouse metabolism-related genes from AmiGO2 database (https://amigo.geneontology.org/amigo) with Ontology ID: GO:0061621 (glycolysis) and GO:0050996 (positive regulation of lipid catabolic process), and we clustered the genes based on their expression levels. Heatmaps were drawn by R package pheatmap (version 1.0.12).

Data availability

Upon revision/publication all numerical data included in the production of figures, plots and statistical analysis will be found in the figures, main text, and Source Data. Additional statistical analysis values (F values, t values, degrees of freedom and p values) will be presented in the Source Data documents. Source data will be provided with this paper. Raw and processed single cell RNAseq data will be available under a GEO accession number during the revision/review process. Code used in the processing of RNAseq data will be made available upon request.

Authors and Affiliations

Department of Biomedical Sciences, University of Lausanne, Lausanne, Switzerland
Joshua Reeves, Pierre Tournier, Pierre Becquart & Shukry J. Habib

Centre for Gene Therapy and Regenerative Medicine, King's College London, London, UK
Joshua Reeves, Robert Carton & Alessandra Vigilante

Zhejiang Provincial Key Laboratory for Cancer Molecular Cell Biology, Life Sciences Institute, Zhejiang University, Hangzhou, Zhejiang 310058, China
Department of Medical Oncology, Key Laboratory of Cancer Prevention and Intervention, Ministry of Education, The Second Affiliated Hospital, Zhejiang University School of Medicine, Hangzhou, Zhejiang, China
Yin Tang & Dong Fang

Author Contributions

S.J.H. conceived the project and with J.R. designed the experiments. J.R. performed surgeries, *ex vivo* experiments, *in vitro* experiments, and collected all data. J.R. analyzed microCT data, and live *ex vivo* staining J.R and P.B analyzed histological staining. P.T and P.B performed experiments in Supplementary Figure 10 and 11. R.C. processed the metagenomic data. J.R., Y.T, A.V. and D.F. performed RNAseq analysis. J.R., P.T. and P.B. prepared the figures. J.R. and S.J.H. interpreted the data and wrote the initial manuscript draft. S.J.H revised the manuscript. All authors approved the manuscript. S.J.H. led the project and provided financial support for the project.

Acknowledgement

We thank Dr Nadège Zanou for discussions about the oligomycin experiments. We also thank Prof Mehdi Tafti and Dr Frédéric Schütz for discussions on statistics.
R.C. salary is supported by MRC MR/S023747/1. This research was supported by funds from the University of Lausanne, Switzerland (S.J.H). Additional financial support from the UK Regenerative Medicine Platform (MR/R015635/1, S.J.H.).

Competing interests:

S.J. H is listed as an inventor on a patent application (P6125GB00) on Tissue Regeneration Patch that includes the Wnt-bandage.

Materials and Methods References

Andrews S. 2015. Babraham Bioinformatics - FastQC A Quality Control tool for High Throughput Sequence Data. https://www.bioinformatics.babraham.ac.uk/projects/fastqc/

Bolger *et al.* 2014. Trimmomatic: a flexible trimmer for Illumina sequence data. *Bioinformatics*, 30(15); 21142120.

Bolyen *et al.* 2019. Reproducible, interactive, scalable and extensible microbiome data science using QIIME 2. *Nature Biotechnology*, 37; 852-857.

Callahan *et al.* 2016. DADA2: High-resolution sample inference from Illumina amplicon data. *Nature Methods*, 13; 581–583.

Ge, Steven Xijin *et al*. 2020. “ShinyGO: A Graphical Gene-Set Enrichment Tool for Animals and Plants.” *Bioinformatics* 36 (8): 2628–29.

Hao *et al.* 2021. “Integrated Analysis of Multimodal Single-Cell Data.” *Cell* 184 (13): 3573– 87.e29.

Kimmel *et al.* 2019. “Murine Single-Cell RNA-Seq Reveals Cell-Identity- and Tissue-Specific Trajectories of Aging.” *Genome Research* 29 (12): 2088–2103.

Lowndes *et al*. 2016. “Immobilized WNT Proteins Act as a Stem Cell Niche for Tissue Engineering”. *Stem Cell Reports*. 7(1):126-37

Lowndes *et al.* 2017. “Constructing Cellular Niche Properties by Localized Presentation of Wnt Proteins on Synthetic Surfaces.” *Nature Protocols* 12 (7): 1498–1512.

Okuchi *et al.* 2021. “Wnt-Modified Materials Mediate Asymmetric Stem Cell Division to Direct Human Osteogenic Tissue Formation for Bone Repair.” *Nature Materials* 20 (1): 108–18.

Main text Bibliography:

Agrawal Singh S, Lerdrup M, Gomes A-LR, van de Werken HJ, Vilstrup Johansen J, Andersson R, Sandelin A, Helin K, Hansen K. 2019. PLZF targets developmental enhancers for activation during osteogenic differentiation of human mesenchymal stem cells. *Elife* **8**. doi:10.7554/eLife.40364

Almalki SG, Agrawal DK. 2016. Effects of matrix metalloproteinases on the fate of mesenchymal stem cells. *Stem Cell Res Ther* **7**:129. doi:10.1186/s13287-016-0393-1

Almeida M. 2012. Aging mechanisms in bone. *Bonekey Rep* **1**. doi:10.1038/bonekey.2012.102

Ambriz X, de Lanerolle P, Ambrosio JR. 2018. The Mechanobiology of the Actin Cytoskeleton in Stem Cells during Differentiation and Interaction with Biomaterials. *Stem Cells Int* **2018**:2891957. doi:10.1155/2018/2891957

Andreatta M, Carmona SJ. 2021. UCell: Robust and scalable single-cell gene signature scoring. *Comput Struct Biotechnol J* **19**:3796–3798. doi:10.1016/j.csbj.2021.06.043

Archbold HC, Yang YX, Chen L, Cadigan KM. 2012. How do they do Wnt they do?: regulation of transcription by the Wnt/β-catenin pathway. *Acta Physiol* **204**:74–109. doi:10.1111/j.1748-1716.2011.02293.x

Beedham W, Peck G, Richardson SE, Tsang K, Fertleman M, Shipway DJ. 2019. Head injury in the elderly - an overview for the physician. *Clin Med* **19**:177–184. doi:10.7861/clinmedicine.19-2-177

Bianco P, Robey PG. 2015. Skeletal stem cells. *Development* **142**:1023–1027. doi:10.1242/dev.102210

Bok S, Yallowitz AR, Sun J, McCormick J, Cung M, Hu L, Lalani S, Li Z, Sosa BR, Baumgartner T, Byrne P, Zhang T, Morse KW, Mohamed FF, Ge C, Franceschi RT, Cowling RT, Greenberg BH, Pisapia DJ, Imahiyerobo TA, Lakhani S, Ross ME, Hoffman CE, Debnath S, Greenblatt MB. 2023. A multi-stem cell basis for craniosynostosis and calvarial mineralization. *Nature* **621**:804–812. doi:10.1038/s41586-023-06526-2

1112 Cappuzzello C, Doni A, Dander E, Pasqualini F, Nebuloni M, Bottazzi B, Mantovani A, Biondi A, Garlanda C,
1113 D'Amico G. 2016. Mesenchymal Stromal Cell-Derived PTX3 Promotes Wound Healing via Fibrin
1114 Remodeling. *J Invest Dermatol* **136**:293–300. doi:10.1038/JID.2015.346
1115 Carson HJ. 2009. Brain trauma in head injuries presenting with and without concurrent skull fractures. *J*
1116 *Forensic Leg Med* **16**:115–120. doi:10.1016/j.jflm.2008.08.013
1117 Catterson JH, Khericha M, Dyson MC, Vincent AJ, Callard R, Haveron SM, Rajasingam A, Ahmad M, Partridge
1118 L. 2018. Short-Term, Intermittent Fasting Induces Long-Lasting Gut Health and TOR-Independent
1119 Lifespan Extension. *Current Biology* **28**:1714-1724.e4. doi:10.1016/j.cub.2018.04.015
1120 Chan CKF, Lindau P, Jiang W, Chen JY, Zhang LF, Chen C-C, Seita J, Sahoo D, Kim J-B, Lee A, Park S, Nag
1121 D, Gong Y, Kulkarni S, Luppen CA, Theologis AA, Wan DC, DeBoer A, Seo EY, Vincent-Tompkins JD,
1122 Loh K, Walmsley GG, Kraft DL, Wu JC, Longaker MT, Weissman IL. 2013. Clonal precursor of bone,
1123 cartilage, and hematopoietic niche stromal cells. *Proc Natl Acad Sci U S A* **110**:12643–12648.
1124 doi:10.1073/pnas.1310212110
1125 Chan CKF, Seo EY, Chen JY, Lo D, McArdle A, Sinha R, Tevlin R, Seita J, Vincent-Tompkins J, Wearda T, Lu
1126 W-J, Senarath-Yapa K, Chung MT, Marecic O, Tran M, Yan KS, Upton R, Walmsley GG, Lee AS,
1127 Sahoo D, Kuo CJ, Weissman IL, Longaker MT. 2015. Identification and specification of the mouse
1128 skeletal stem cell. *Cell* **160**:285–298. doi:10.1016/j.cell.2014.12.002
1129 Chen J, Sivan U, Tan SL, Lippo L, De Angelis J, Labella R, Singh A, Chatzis A, Cheuk S, Medhghalchi M, Gil
1130 J, Hollander G, Marsden BD, Williams R, Ramasamy SK, Kusumbe AP. 2021. High-resolution 3D
1131 imaging uncovers organ-specific vascular control of tissue aging. *Sci Adv* **7**:eabd7819.
1132 doi:10.1126/sciadv.abd7819
1133 Cotofana S, Gotkin RH, Ascher B, Morozov SP, Gombolevsky VA, Laipan AS, Pyatintsky IA, Movsisyan TV,
1134 Koban KC, Hladik C, Frank K. 2018. Calvarial Volume Loss and Facial Aging: A Computed
1135 Tomographic (CT)-Based Study. *Aesthet Surg J* **38**:1043–1051. doi:10.1093/asj/sjy096
1136 Covarrubias AJ, Perrone R, Grozio A, Verdin E. 2021. NAD+ metabolism and its roles in cellular processes
1137 during ageing. *Nat Rev Mol Cell Biol* **22**:119–141. doi:10.1038/s41580-020-00313-x
1138 Creed S, McKenzie M. 2019. Measurement of Mitochondrial Membrane Potential with the Fluorescent Dye
1139 Tetramethylrhodamine Methyl Ester (TMRM). *Methods Mol Biol* **1928**:69–76. doi:10.1007/978-1-4939-
1140 9027-6_5
1141 Dahl KN, Ribeiro AJS, Lammerding J. 2008. Nuclear shape, mechanics, and mechanotransduction. *Circ Res*
1142 **102**:1307–1318. doi:10.1161/CIRCRESAHA.108.173989
1143 Dao MC, Everard A, Aron-Wisnewsky J, Sokolovska N, Prifti E, Verger EO, Kayser BD, Levenez F, Chilloux
1144 J, Hoyles L, MICRO-Obes Consortium, Dumas M-E, Rizkalla SW, Doré J, Cani PD, Clément K. 2016.
1145 Akkermansia muciniphila and improved metabolic health during a dietary intervention in obesity:
1146 relationship with gut microbiome richness and ecology. *Gut* **65**:426–436. doi:10.1136/gutjnl-2014-
1147 308778
1148 Debnath S, Yallowitz AR, McCormick J, Lalani S, Zhang T, Xu R, Li N, Liu Y, Yang YS, Eiseman M, Shim J-H,
1149 Hameed M, Healey JH, Bostrom MP, Landau DA, Greenblatt MB. 2018. Discovery of a periosteal stem
1150 cell mediating intramembranous bone formation. *Nature* **562**:133–139. doi:10.1038/s41586-018-0554-
1151 8
1152 Derrien M, Collado MC, Ben-Amor K, Salminen S, de Vos WM. 2008. The Mucin degrader Akkermansia
1153 muciniphila is an abundant resident of the human intestinal tract. *Appl Environ Microbiol* **74**:1646–
1154 1648. doi:10.1128/AEM.01226-07
1155 Devenish RJ, Prescott M, Boyle GM, Nagley P. 2000. [No title found]. *Journal of Bioenergetics and*
1156 *Biomembranes* **32**:507–515. doi:10.1023/A:1005621125812
1157 Ding L, Vezzani B, Khan N, Su J, Xu L, Yan G, Liu Y, Li R, Gaur A, Diao Z, Hu Y, Yang Z, Hardy WR, James
1158 AW, Sun H, Péault B. 2020. CD10 expression identifies a subset of human perivascular progenitor
1159 cells with high proliferation and calcification potentials. *Stem Cells* **38**:261–275. doi:10.1002/stem.3112
1160 Duchamp de Lageneste O, Julien A, Abou-Khalil R, Frangi G, Carvalho C, Cagnard N, Cordier C, Conway SJ,
1161 Colnot C. 2018. Periosteum contains skeletal stem cells with high bone regenerative potential
1162 controlled by Periostin. *Nat Commun* **9**:773. doi:10.1038/s41467-018-03124-z
1163 Dugina V, Zwaenepoel I, Gabbiani G, Clément S, Chaponnier C. 2009. Beta and gamma-cytoplasmic actins
1164 display distinct distribution and functional diversity. *J Cell Sci* **122**:2980–2988. doi:10.1242/jcs.041970

1165 Dutta S, Sengupta P. 2016. Men and mice: Relating their ages. *Life Sci* **152**:244–248.
1166 doi:10.1016/j.lfs.2015.10.025
1167 Ferrari S, Pesce M. 2021. Stiffness and Aging in Cardiovascular Diseases: The Dangerous Relationship
1168 between Force and Senescence. *Int J Mol Sci* **22**. doi:10.3390/ijms22073404
1169 Fletcher DA, Mullins RD. 2010. Cell mechanics and the cytoskeleton. *Nature* **463**:485–492.
1170 doi:10.1038/nature08908
1171 Garcin CL, Habib SJ. 2017. A Comparative Perspective on Wnt/β-Catenin Signalling in Cell Fate
1172 Determination. *Results Probl Cell Differ* **61**:323–350. doi:10.1007/978-3-319-53150-2_15
1173 Gillispie GJ, Sah E, Krishnamurthy S, Ahmidouch MY, Zhang B, Orr ME. 2021. Evidence of the Cellular
1174 Senescence Stress Response in Mitotically Active Brain Cells-Implications for Cancer and
1175 Neurodegeneration. *Life* **11**. doi:10.3390/life11020153
1176 Goligorsky MS. 2010. Microvascular rarefaction: The decline and fall of blood vessels. *Organogenesis* **6**:1–
1177 10. doi:10.4161/org.6.1.10427
1178 Goss AM, Tian Y, Tsukiyama T, Cohen ED, Zhou D, Lu MM, Yamaguchi TP, Morrisey EE. 2009. Wnt2/2b and
1179 beta-catenin signaling are necessary and sufficient to specify lung progenitors in the foregut. *Dev Cell*
1180 **17**:290–298. doi:10.1016/j.devcel.2009.06.005
1181 Gowans GJ, Hardie DG. 2014. AMPK: a cellular energy sensor primarily regulated by AMP. *Biochem Soc*
1182 *Trans* **42**:71–75. doi:10.1042/BST20130244
1183 Granéli C, Thorfve A, Ruetschi U, Brisby H, Thomsen P, Lindahl A, Karlsson C. 2014. Novel markers of
1184 osteogenic and adipogenic differentiation of human bone marrow stromal cells identified using a
1185 quantitative proteomics approach. *Stem Cell Res* **12**:153–165. doi:10.1016/j.scr.2013.09.009
1186 Grunewald M, Kumar S, Sharife H, Volinsky E, Gileles-Hillel A, Licht T, Permyakova A, Hinden L, Azar S,
1187 Friedmann Y, Kupetz P, Tzuberi R, Anisimov A, Alitalo K, Horwitz M, Leebhoff S, Khoma OZ, Hlushchuk
1188 R, Djonov V, Abramovitch R, Tam J, Keshet E. 2021. Counteracting age-related VEGF signaling
1189 insufficiency promotes healthy aging and extends life span. *Science* **373**:eabc8479.
1190 doi:10.1126/science.abc8479
1191 Haage A, Nam DH, Ge X, Schneider IC. 2014. Matrix metalloproteinase-14 is a mechanically regulated
1192 activator of secreted MMPs and invasion. *Biochem Biophys Res Commun* **450**:213–218.
1193 doi:10.1016/j.bbrc.2014.05.086
1194 Hirata H, Zhang N, Ueno M, Barati D, Kushioka J, Shen H, Tsubosaka M, Toya M, Lin T, Huang E, Yao Z, Wu
1195 JY, Zwingenberger S, Yang F, Goodman SB. 2022. Ageing attenuates bone healing by mesenchymal
1196 stem cells in a microribbon hydrogel with a murine long bone critical-size defect model. *Immun Ageing*
1197 **19**:14. doi:10.1186/s12979-022-00272-1
1198 Horowitz MC, Fields A, DeMeo D, Qian HY, Bothwell AL, Trepman E. 1994. Expression and regulation of Ly-
1199 6 differentiation antigens by murine osteoblasts. *Endocrinology* **135**:1032–1043.
1200 doi:10.1210/endo.135.3.7520861
1201 Huelke DF, Compton CP. 1983. Facial injuries in automobile crashes. *J Oral Maxillofac Surg* **41**:241–244.
1202 doi:10.1016/0278-2391(83)90266-5
1203 Jeffery EC, Mann TLA, Pool JA, Zhao Z, Morrison SJ. 2022. Bone marrow and periosteal skeletal
1204 stem/progenitor cells make distinct contributions to bone maintenance and repair. *Cell Stem Cell*
1205 **29**:1547-1561.e6. doi:10.1016/j.stem.2022.10.002
1206 Jilka RL. 2013. The relevance of mouse models for investigating age-related bone loss in humans. *J Gerontol*
1207 *A Biol Sci Med Sci* **68**:1209–1217. doi:10.1093/gerona/glt046
1208 Jin S, Guerrero-Juarez CF, Zhang L, Chang I, Ramos R, Kuan C-H, Myung P, Plikus MV, Nie Q. 2021.
1209 Inference and analysis of cell-cell communication using CellChat. *Nat Commun* **12**:1088.
1210 doi:10.1038/s41467-021-21246-9
1211 Jung Y-S, Jun S, Lee SH, Sharma A, Park J-I. 2015. Wnt2 complements Wnt/β-catenin signaling in colorectal
1212 cancer. *Oncotarget* **6**:37257–37268. doi:10.18632/oncotarget.6133
1213 Kang M-J, Ahn H-S, Lee J-Y, Matsuhashi S, Park W-Y. 2002. Up-regulation of PDCD4 in senescent human
1214 diploid fibroblasts. *Biochem Biophys Res Commun* **293**:617–621. doi:10.1016/S0006-291X(02)00264-
1215 4
1216 Khan AU, Qu R, Fan T, Ouyang J, Dai J. 2020. A glance on the role of actin in osteogenic and adipogenic
1217 differentiation of mesenchymal stem cells. *Stem Cell Res Ther* **11**:283. doi:10.1186/s13287-020-
1218 01789-2

1219 Kim H-N, Ponte F, Warren A, Ring R, Iyer S, Han L, Almeida M. 2021. A decrease in NAD+ contributes to the
1220 loss of osteoprogenitors and bone mass with aging. *NPJ Aging Mech Dis* **7**:8. doi:10.1038/s41514-
1221 021-00058-7
1222 Kim Y-K, Nakata H, Yamamoto M, Miyasaka M, Kasugai S, Kuroda S. 2016. Osteogenic Potential of Mouse
1223 Periosteum-Derived Cells Sorted for CD90 In Vitro and In Vivo. *Stem Cells Transl Med* **5**:227–234.
1224 doi:10.5966/sctm.2015-0013
1225 Kokabu S, Gamer L, Cox K, Lowery J, Tsuji K, Raz R, Economides A, Katagiri T, Rosen V. 2012. BMP3
1226 suppresses osteoblast differentiation of bone marrow stromal cells via interaction with Acvr2b. *Mol*
1227 *Endocrinol* **26**:87–94. doi:10.1210/me.2011-1168
1228 Lähteenvuo J, Rosenzweig A. 2012. Effects of Aging on Angiogenesis. *Circulation Research* **110**:1252–1264.
1229 doi:10.1161/CIRCRESAHA.111.246116
1230 Lawenius L, Scheffler JM, Gustafsson KL, Henning P, Nilsson KH, Colldén H, Islander U, Plovier H, Cani PD,
1231 de Vos WM, Ohlsson C, Sjögren K. 2020. Pasteurized Akkermansia muciniphila protects from fat mass
1232 gain but not from bone loss. *Am J Physiol Endocrinol Metab* **318**:E480–E491.
1233 doi:10.1152/ajpendo.00425.2019
1234 Leite G, Pimentel M, Barlow GM, Chang C, Hosseini A, Wang J, Parodi G, Sedighi R, Rezaie A, Mathur R.
1235 2021. Age and the aging process significantly alter the small bowel microbiome. *Cell Rep* **36**:109765.
1236 doi:10.1016/j.celrep.2021.109765
1237 Levine ME, Suarez JA, Brandhorst S, Balasubramanian P, Cheng C-W, Madia F, Fontana L, Mirisola MG,
1238 Guevara-Aguirre J, Wan J, Passarino G, Kennedy BK, Wei M, Cohen P, Crimmins EM, Longo VD.
1239 2014. Low Protein Intake Is Associated with a Major Reduction in IGF-1, Cancer, and Overall Mortality
1240 in the 65 and Younger but Not Older Population. *Cell Metabolism* **19**:407–417.
1241 doi:10.1016/j.cmet.2014.02.006
1242 Li B, Wang Y, Fan Y, Ouchi T, Zhao Z, Li L. 2021. Cranial Suture Mesenchymal Stem Cells: Insights and
1243 Advances. *Biomolecules* **11**. doi:10.3390/biom11081129
1244 Li H-S, Zhou Y-N, Li L, Li S-F, Long D, Chen X-L, Zhang J-B, Feng L, Li Y-P. 2019. HIF-1α protects against
1245 oxidative stress by directly targeting mitochondria. *Redox Biol* **25**:101109.
1246 doi:10.1016/j.redox.2019.101109
1247 Li L, Chen Xiangjuan, Chen Xian, Yang L, Zeng Y, Xu J. n.d. TNFAIP6 Defines the MSC Subpopulation with
1248 Enhanced Immune Suppression Activities. doi:10.21203/rs.3.rs-1469688/v1
1249 Li L, Su Y, Li F, Wang Y, Ma Z, Li Z, Su J. 2020. The effects of daily fasting hours on shaping gut microbiota
1250 in mice. *BMC Microbiol* **20**:65. doi:10.1186/s12866-020-01754-2
1251 Li R, Liang Y, Lin B. 2022. Accumulation of systematic TPM1 mediates inflammation and neuronal remodeling
1252 by phosphorylating PKA and regulating the FABP5/NF-κB signaling pathway in the retina of aged mice.
1253 *Aging Cell* **21**:e13566. doi:10.1111/acel.13566
1254 Li S, Zhan J-K, Wang Y-J, Lin X, Zhong J-Y, Wang Y, Tan P, He J-Y, Cui X-J, Chen Y-Y, Huang W, Liu Y-S.
1255 2019. Exosomes from hyperglycemia-stimulated vascular endothelial cells contain versican that
1256 regulate calcification/senescence in vascular smooth muscle cells. *Cell Biosci* **9**:1.
1257 doi:10.1186/s13578-018-0263-x
1258 Licciardi PV, Ververis K, Karagiannis TC. 2011. Histone deacetylase inhibition and dietary short-chain Fatty
1259 acids. *ISRN Allergy* **2011**:869647. doi:10.5402/2011/869647
1260 Lim CH, Ito M. 2022. Niche stiffness regulates stem cell aging. *Nature Aging* **2**:568–569. doi:10.1038/s43587-
1261 022-00259-z
1262 Liu G, Vijayakumar S, Grumolato L, Arroyave R, Qiao H, Akiri G, Aaronson SA. 2009. Canonical Wnts function
1263 as potent regulators of osteogenesis by human mesenchymal stem cells. *J Cell Biol* **185**:67–75.
1264 doi:10.1083/jcb.200810137
1265 Liu J-H, Yue T, Luo Z-W, Cao J, Yan Z-Q, Jin L, Wan T-F, Shuai C-J, Wang Z-G, Zhou Y, Xu R, Xie H. 2020.
1266 Akkermansia muciniphila promotes type H vessel formation and bone fracture healing by reducing gut
1267 permeability and inflammation. *Dis Model Mech* **13**. doi:10.1242/dmm.043620
1268 Liu M, Nakasaki M, Shih Y-RV, Varghese S. 2018. Effect of age on biomaterial-mediated in situ bone tissue
1269 regeneration. *Acta Biomater* **78**:329–340. doi:10.1016/j.actbio.2018.06.035
1270 Liu S, Matsui TS, Kang N, Deguchi S. 2022. Analysis of senescence-responsive stress fiber proteome reveals
1271 reorganization of stress fibers mediated by elongation factor eEF2 in HFF-1 cells. *Mol Biol Cell*
1272 **33**:ar10. doi:10.1091/mbc.E21-05-0229

1273 Liu TM, Lee EH. 2013. Transcriptional regulatory cascades in Runx2-dependent bone development. *Tissue*
1274 *Eng Part B Rev* **19**:254–263. doi:10.1089/ten.TEB.2012.0527
1275 Locatelli V, Bianchi VE. 2014. Effect of GH/IGF-1 on Bone Metabolism and Osteoporsosis. *Int J Endocrinol*
1276 **2014**:235060. doi:10.1155/2014/235060
1277 Loi F, Córdova LA, Pajarinen J, Lin T-H, Yao Z, Goodman SB. 2016. Inflammation, fracture and bone repair.
1278 *Bone* **86**:119–130. doi:10.1016/j.bone.2016.02.020
1279 Longo VD, Anderson RM. 2022. Nutrition, longevity and disease: From molecular mechanisms to
1280 interventions. *Cell* **185**:1455–1470. doi:10.1016/j.cell.2022.04.002
1281 Longo VD, Di Tano M, Mattson MP, Guidi N. 2021. Intermittent and periodic fasting, longevity and disease.
1282 *Nat Aging* **1**:47–59. doi:10.1038/s43587-020-00013-3
1283 Lovett DB, Shekhar N, Nickerson JA, Roux KJ, Lele TP. 2013. Modulation of Nuclear Shape by Substrate
1284 Rigidity. *Cell Mol Bioeng* **6**:230–238. doi:10.1007/s12195-013-0270-2
1285 Lowndes M, Rotherham M, Price JC, El Haj AJ, Habib SJ. 2016. Immobilized WNT Proteins Act as a Stem
1286 Cell Niche for Tissue Engineering. *Stem Cell Reports* **7**:126–137. doi:10.1016/j.stemcr.2016.06.004
1287 Luo M-J, Rao S-S, Tan Y-J, Yin H, Hu X-K, Zhang Y, Liu Y-W, Yue T, Chen L-J, Li L, Huang Y-R, Qian Y-X, Liu
1288 Z-Z, Cao J, Wang Z-X, Luo Z-W, Wang Y-Y, Xia K, Tang S-Y, Chen C-Y, Xie H. 2020. Fasting before
1289 or after wound injury accelerates wound healing through the activation of pro-angiogenic SMOC1 and
1290 SCG2. *Theranostics* **10**:3779–3792. doi:10.7150/thno.44115
1291 Lv J, Sun X, Ma J, Ma X, Xing G, Wang Y, Sun L, Wang J, Li F, Li Y. 2015. Involvement of periostin-sclerostin-
1292 Wnt/β-catenin signaling pathway in the prevention of neurectomy-induced bone loss by naringin.
1293 *Biochem Biophys Res Commun* **468**:587–593. doi:10.1016/j.bbrc.2015.10.152
1294 Magne F, Gotteland M, Gauthier L, Zazueta A, Pesoa S, Navarrete P, Balamurugan R. 2020. The
1295 Firmicutes/Bacteroidetes Ratio: A Relevant Marker of Gut Dysbiosis in Obese Patients? *Nutrients* **12**.
1296 doi:10.3390/nu12051474
1297 Maruyama T, Jeong J, Sheu T-J, Hsu W. 2016. Stem cells of the suture mesenchyme in craniofacial bone
1298 development, repair and regeneration. *Nat Commun* **7**:10526. doi:10.1038/ncomms10526
1299 Matsushita Y, Ono W, Ono N. 2020. Skeletal Stem Cells for Bone Development and Repair: Diversity Matters.
1300 *Curr Osteoporos Rep* **18**:189–198. doi:10.1007/s11914-020-00572-9
1301 Matsushita Y, Sakamoto K, Tamamura Y, Shibata Y, Minamizato T, Kihara T, Ito M, Katsube K-I, Hiraoka S,
1302 Koseki H, Harada K, Yamaguchi A. 2013. CCN3 Protein Participates in Bone Regeneration as an
1303 Inhibitory Factor *. *J Biol Chem* **288**:19973–19985. doi:10.1074/jbc.M113.454652
1304 McCarron JG, Wilson C, Sandison ME, Olson ML, Girkin JM, Saunter C, Chalmers S. 2013. From Structure
1305 to Function: Mitochondrial Morphology, Motion and Shaping in Vascular Smooth Muscle. *J Vasc Res*
1306 **50**:357–371. doi:10.1159/000353883
1307 Menon S, Salhotra A, Shailendra S, Tevlin R, Ransom RC, Januszyk M, Chan CKF, Behr B, Wan DC,
1308 Longaker MT, Quarto N. 2021. Skeletal stem and progenitor cells maintain cranial suture patency and
1309 prevent craniosynostosis. *Nat Commun* **12**:4640. doi:10.1038/s41467-021-24801-6
1310 Mills KF, Yoshida S, Stein LR, Grozio A, Kubota S, Sasaki Y, Redpath P, Migaud ME, Apte RS, Uchida K,
1311 Yoshino J, Imai S-I. 2016. Long-Term Administration of Nicotinamide Mononucleotide Mitigates Age-
1312 Associated Physiological Decline in Mice. *Cell Metab* **24**:795–806. doi:10.1016/j.cmet.2016.09.013
1313 Novoseletskaya E, Grigorieva O, Nimiritsky P, Basalova N, Eremichev R, Milovskaya I, Kulebyakin K,
1314 Kulebyakina M, Rodionov S, Omelyanenko N, Efimenko A. 2020. Mesenchymal Stromal Cell-
1315 Produced Components of Extracellular Matrix Potentiate Multipotent Stem Cell Response to
1316 Differentiation Stimuli. *Front Cell Dev Biol* **8**:555378. doi:10.3389/fcell.2020.555378
1317 Nusspaumer G, Jaiswal S, Barbero A, Reinhardt R, Ishay Ronen D, Haumer A, Lufkin T, Martin I, Zeller R.
1318 2017. Ontogenic Identification and Analysis of Mesenchymal Stromal Cell Populations during Mouse
1319 Limb and Long Bone Development. *Stem Cell Reports* **9**:1124–1138.
1320 doi:10.1016/j.stemcr.2017.08.007
1321 Okuchi Y, Reeves J, Ng SS, Doro DH, Junyent S, Liu KJ, El Haj AJ, Habib SJ. 2021. Wnt-modified materials
1322 mediate asymmetric stem cell division to direct human osteogenic tissue formation for bone repair. *Nat*
1323 *Mater* **20**:108–118. doi:10.1038/s41563-020-0786-5
1324 Ortinau LC, Wang H, Lei K, Deveza L, Jeong Y, Hara Y, Grafe I, Rosenfeld SB, Lee D, Lee B, Scadden DT,
1325 Park D. 2019. Identification of functionally distinct Mx1+αSMA+ periosteal skeletal stem cells. *Cell*
1326 *Stem Cell* **25**:784-796.e5. doi:10.1016/j.stem.2019.11.003

1327 Özkul C, Yalınay M, Karakan T. 2019. Islamic fasting leads to an increased abundance of Akkermansia
1328 muciniphila and Bacteroides fragilis group: A preliminary study on intermittent fasting. *Turk J*
1329 *Gastroenterol* **30**:1030–1035. doi:10.5152/tjg.2019.19185
1330 Paine A, Woeller CF, Zhang H, Luz Garcia-Hernandez M, Huertas N, Xing L, Phipps RP, Ritchlin CT. 2018.
1331 Thy1 is a positive regulator of osteoblast differentiation and modulates bone homeostasis in obese
1332 mice. *FASEB j* **32**:3174–3183. doi:10.1096/fj.201701379R
1333 Petersen C, Nielsen MD, Andersen ES, Basse AL, Isidor MS, Markussen LK, Viuff BM, Lambert IH, Hansen
1334 JB, Pedersen SF. 2017. MCT1 and MCT4 Expression and Lactate Flux Activity Increase During White
1335 and Brown Adipogenesis and Impact Adipocyte Metabolism. *Sci Rep* **7**:13101. doi:10.1038/s41598-
1336 017-13298-z
1337 Pongkitwitoon S, Uzer G, Rubin J, Judex S. 2016. Cytoskeletal Configuration Modulates Mechanically
1338 Induced Changes in Mesenchymal Stem Cell Osteogenesis, Morphology, and Stiffness. *Sci Rep*
1339 **6**:34791. doi:10.1038/srep34791
1340 Provost PR, Marcel YL, Milne RW, Weech PK, Rassart E. 1991. Apolipoprotein D transcription occurs
1341 specifically in nonproliferating quiescent and senescent fibroblast cultures. *FEBS Lett* **290**:139–141.
1342 doi:10.1016/0014-5793(91)81244-3
1343 Rafei M, Hsieh J, Fortier S, Li M, Yuan S, Birman E, Forner K, Boivin M-N, Doody K, Tremblay M, Annabi B,
1344 Galipeau J. 2008. Mesenchymal stromal cell–derived CCL2 suppresses plasma cell immunoglobulin
1345 production via STAT3 inactivation and PAX5 induction. *Blood* **112**:4991–4998. doi:10.1182/blood-
1346 2008-07-166892
1347 Ren L, Wang D, Liu X, Yu H, Jiang C, Hu Y. 2020. Influence of Skull Fracture on Traumatic Brain Injury Risk
1348 Induced by Blunt Impact. *Int J Environ Res Public Health* **17**. doi:10.3390/ijerph17072392
1349 Ren X, Li B, Xu C, Zhuang H, Lei T, Jiang F, Zhou P. 2022. High expression of Piezo1 induces senescence in
1350 chondrocytes through calcium ions accumulation. *Biochem Biophys Res Commun* **607**:138–145.
1351 doi:10.1016/j.bbrc.2022.03.119
1352 Reunanen J, Kainulainen V, Huuskonen L, Ottman N, Belzer C, Huhtinen H, de Vos WM, Satokari R. 2015.
1353 Akkermansia muciniphila Adheres to Enterocytes and Strengthens the Integrity of the Epithelial Cell
1354 Layer. *Appl Environ Microbiol* **81**:3655–3662. doi:10.1128/AEM.04050-14
1355 Ries C, Egea V, Karow M, Kolb H, Jochum M, Neth P. 2007. MMP-2, MT1-MMP, and TIMP-2 are essential for
1356 the invasive capacity of human mesenchymal stem cells: differential regulation by inflammatory
1357 cytokines. *Blood* **109**:4055–4063. doi:10.1182/blood-2006-10-051060
1358 Safwan-Zaiter H, Wagner N, Wagner K-D. 2022. P16INK4A—More Than a Senescence Marker. *Life* **12**:1332.
1359 doi:10.3390/life12091332
1360 Segel M, Neumann B, Hill MFE, Weber IP, Viscomi C, Zhao C, Young A, Agley CC, Thompson AJ, Gonzalez
1361 GA, Sharma A, Holmqvist S, Rowitch DH, Franze K, Franklin RJM, Chalut KJ. 2019. Niche stiffness
1362 underlies the ageing of central nervous system progenitor cells. *Nature* **573**:130–134.
1363 doi:10.1038/s41586-019-1484-9
1364 Shiozawa Y, Pedersen EA, Patel LR, Ziegler AM, Havens AM, Jung Y, Wang J, Zalucha S, Loberg RD, Pienta
1365 KJ, Taichman RS. 2010. GAS6/AXL axis regulates prostate cancer invasion, proliferation, and survival
1366 in the bone marrow niche. *Neoplasia* **12**:116–127. doi:10.1593/neo.91384
1367 Simiczyjew A, Mazur AJ, Popow-Woźniak A, Malicka-Błaszkiewicz M, Nowak D. 2014. Effect of
1368 overexpression of β- and γ-actin isoforms on actin cytoskeleton organization and migration of human
1369 colon cancer cells. *Histochem Cell Biol* **142**:307–322. doi:10.1007/s00418-014-1199-9
1370 Smith H, Whittall C, Weksler B, Middleton J. 2012. Chemokines stimulate bidirectional migration of human
1371 mesenchymal stem cells across bone marrow endothelial cells. *Stem Cells Dev* **21**:476–486.
1372 doi:10.1089/scd.2011.0025
1373 Song J, Li J, Yang F, Ning G, Zhen L, Wu L, Zheng Y, Zhang Q, Lin D, Xie C, Peng L. 2019. Nicotinamide
1374 mononucleotide promotes osteogenesis and reduces adipogenesis by regulating mesenchymal
1375 stromal cells via the SIRT1 pathway in aged bone marrow. *Cell Death Dis* **10**:336. doi:10.1038/s41419-
1376 019-1569-2
1377 Stein GH, Drullinger LF, Soulard A, Dulić V. 1999. Differential roles for cyclin-dependent kinase inhibitors p21
1378 and p16 in the mechanisms of senescence and differentiation in human fibroblasts. *Mol Cell Biol*
1379 **19**:2109–2117. doi:10.1128/MCB.19.3.2109

1380 Stein LR, Imai S-I. 2012. The dynamic regulation of NAD metabolism in mitochondria. *Trends Endocrinol*
1381 *Metab* **23**:420–428. doi:10.1016/j.tem.2012.06.005
1382 Stricker J, Falzone T, Gardel ML. 2010. Mechanics of the F-actin cytoskeleton. *J Biomech* **43**:9–14.
1383 doi:10.1016/j.jbiomech.2009.09.003
1384 Tang Y, Rowe RG, Botvinick EL, Kurup A, Putnam AJ, Seiki M, Weaver VM, Keller ET, Goldstein S, Dai J,
1385 Begun D, Saunders T, Weiss SJ. 2013. MT1-MMP-dependent control of skeletal stem cell commitment
1386 via a β1-integrin/YAP/TAZ signaling axis. *Dev Cell* **25**:402–416. doi:10.1016/j.devcel.2013.04.011
1387 Torimitsu S, Nishida Y, Takano T, Koizumi Y, Makino Y, Yajima D, Hayakawa M, Inokuchi G, Motomura A,
1388 Chiba F, Otsuka K, Kobayashi K, Odo Y, Iwase H. 2014. Statistical analysis of biomechanical properties
1389 of the adult skull and age-related structural changes by sex in a Japanese forensic sample. *Forensic*
1390 *Sci Int* **234**:185.e1–9. doi:10.1016/j.forsciint.2013.10.001
1391 Trapnell C, Cacchiarelli D, Grimsby J, Pokharel P, Li S, Morse M, Lennon NJ, Livak KJ, Mikkelsen TS, Rinn
1392 JL. 2014. The dynamics and regulators of cell fate decisions are revealed by pseudotemporal ordering
1393 of single cells. *Nat Biotechnol* **32**:381–386. doi:10.1038/nbt.2859
1394 Tsai Y-C, Rau C-S, Huang J-F, Chang Y-M, Chia K-J, Hsieh T-M, Chou S-E, Su W-T, Hsu S-Y, Hsieh C-H.
1395 2022. The Association between Skull Bone Fractures and the Mortality Outcomes of Patients with
1396 Traumatic Brain Injury. *Emerg Med Int* **2022**:1296590. doi:10.1155/2022/1296590
1397 Tyurin-Kuzmin PA, Zhdanovskaya ND, Sukhova AA, Sagaradze GD, Albert EA, Ageeva LV, Sharonov GV,
1398 Vorotnikov AV, Tkachuk VA. 2016. Nox4 and Duox1/2 Mediate Redox Activation of Mesenchymal Cell
1399 Migration by PDGF. *PLoS One* **11**:e0154157. doi:10.1371/journal.pone.0154157
1400 van den Bos T, Speijer D, Bank RA, Brömme D, Everts V. 2008. Differences in matrix composition between
1401 calvaria and long bone in mice suggest differences in biomechanical properties and resorption: Special
1402 emphasis on collagen. *Bone* **43**:459–468. doi:10.1016/j.bone.2008.05.009
1403 Veronese N, Reginster J-Y. 2019. The effects of calorie restriction, intermittent fasting and vegetarian diets on
1404 bone health. *Aging Clin Exp Res* **31**:753–758. doi:10.1007/s40520-019-01174-x
1405 Villa CR, Ward WE, Comelli EM. 2017. Gut microbiota-bone axis. *Crit Rev Food Sci Nutr* **57**:1664–1672.
1406 doi:10.1080/10408398.2015.1010034
1407 Volonte D, Galbiati F. 2020. Caveolin-1, a master regulator of cellular senescence. *Cancer Metastasis Rev*
1408 **39**:397–414. doi:10.1007/s10555-020-09875-w
1409 Wagner W, Bork S, Horn P, Krunic D, Walenda T, Diehlmann A, Benes V, Blake J, Huber F-X, Eckstein V,
1410 Boukamp P, Ho AD. 2009. Aging and replicative senescence have related effects on human stem and
1411 progenitor cells. *PLoS One* **4**:e5846. doi:10.1371/journal.pone.0005846
1412 Wanandi SI, Purnamawati P, Tamara A, Putri KT, Simadibrata DM. 2018. Analysis of ALDH1A1 and ALDH1A3
1413 Gene mRNA Expressions in Adipose-Derived Stem Cells (ASCs) and Umbilical Cord Stem Cells
1414 (UCSCs). *The Indonesian Biomedical Journal* **10**:290–296. doi:10.18585/inabj.v10i3.477
1415 Wang D, Christensen K, Chawla K, Xiao G, Krebsbach PH, Franceschi RT. 1999. Isolation and
1416 characterization of MC3T3-E1 preosteoblast subclones with distinct in vitro and in vivo
1417 differentiation/mineralization potential. *J Bone Miner Res* **14**:893–903.
1418 doi:10.1359/jbmr.1999.14.6.893
1419 Westermann B. 2012. Bioenergetic role of mitochondrial fusion and fission. *Biochimica et Biophysica Acta*
1420 *(BBA) - Bioenergetics* **1817**:1833–1838. doi:10.1016/j.bbabio.2012.02.033
1421 Wiese DM, Ruttan CC, Wood CA, Ford BN, Braid LR. 2019. Accumulating Transcriptome Drift Precedes Cell
1422 Aging in Human Umbilical Cord-Derived Mesenchymal Stromal Cells Serially Cultured to Replicative
1423 Senescence. *Stem Cells Transl Med* **8**:945–958. doi:10.1002/sctm.18-0246
1424 Wilk K, Yeh S-CA, Mortensen LJ, Ghaffarigarakani S, Lombardo CM, Bassir SH, Aldawood ZA, Lin CP, Intini
1425 G. 2017. Postnatal Calvarial Skeletal Stem Cells Expressing PRX1 Reside Exclusively in the Calvarial
1426 Sutures and Are Required for Bone Regeneration. *Stem Cell Reports* **8**:933–946.
1427 doi:10.1016/j.stemcr.2017.03.002
1428 Xie S-A, Zhang T, Wang J, Zhao F, Zhang Y-P, Yao W-J, Hur SS, Yeh Y-T, Pang W, Zheng L-S, Fan Y-B, Kong
1429 W, Wang X, Chiu J-J, Zhou J. 2018. Matrix stiffness determines the phenotype of vascular smooth
1430 muscle cell in vitro and in vivo: Role of DNA methyltransferase 1. *Biomaterials* **155**:203–216.
1431 doi:10.1016/j.biomaterials.2017.11.033

Yang J, Bi X, Li M. 2019. Osteoclast Differentiation Assay In: Su GH, editor. Pancreatic Cancer, Methods in Molecular Biology. New York, NY: Springer New York. pp. 143–148. doi:10.1007/978-1-4939-8879-2_12

Yang J, Liu K, Yang J, Jin B, Chen H, Zhan X, Li Z, Wang L, Shen X, Li M, Yu W, Mao Z. 2017. PIM1 induces cellular senescence through phosphorylation of UHRF1 at Ser311. *Oncogene* **36**:4828–4842. doi:10.1038/onc.2017.96

Yang Y, Sauve AA. 2016. NAD+ metabolism: Bioenergetics, signaling and manipulation for therapy. *Biochimica et Biophysica Acta (BBA) - Proteins and Proteomics* **1864**:1787–1800. doi:10.1016/j.bbapap.2016.06.014

Yates LB, Karasik D, Beck TJ, Cupples LA, Kiel DP. 2007. Hip structural geometry in old and old-old age: similarities and differences between men and women. *Bone* **41**:722–732. doi:10.1016/j.bone.2007.06.001

Ye Y, Hu W, Guo F, Zhang W, Wang J, Chen A. 2012. Glycosaminoglycan chains of biglycan promote bone morphogenetic protein-4-induced osteoblast differentiation. *Int J Mol Med* **30**:1075–1080. doi:10.3892/ijmm.2012.1091

Zhang F, Luo K, Rong Z, Wang Z, Luo F, Zhang Z, Sun D, Dong S, Xu J, Dai F. 2017. Periostin Upregulates Wnt/β-Catenin Signaling to Promote the Osteogenesis of CTLA4-Modified Human Bone Marrow-Mesenchymal Stem Cells. *Sci Rep* **7**:41634. doi:10.1038/srep41634

Zhang J, Ma Z, Yan K, Wang Y, Yang Y, Wu X. 2019. Matrix Gla Protein Promotes the Bone Formation by Up-Regulating Wnt/β-Catenin Signaling Pathway. *Front Endocrinol* **10**:891. doi:10.3389/fendo.2019.00891

Zhang W, Chen E, Chen M, Ye C, Qi Y, Ding Q, Li H, Xue D, Gao X, Pan Z. 2018. IGFBP7 regulates the osteogenic differentiation of bone marrow-derived mesenchymal stem cells via Wnt/β-catenin signaling pathway. *FASEB J* **32**:2280–2291. doi:10.1096/fj.201700998RR

Zhao H, Feng J, Ho T-V, Grimes W, Urata M, Chai Y. 2015. The suture provides a niche for mesenchymal stem cells of craniofacial bones. *Nat Cell Biol* **17**:386–396. doi:10.1038/ncb3139

Zhong-Sheng Z, Nuo Y, Xiao-Yan H, Liang D, Rui F, Hai-Jun X. 2022. MMP2 promotes osteoblast differentiation and calcification of muscle-derived mesenchymal stem cells by interaction with miR-29b-3p. *Tissue Cell* **76**:101807. doi:10.1016/j.tice.2022.101807

Zhu L, Tang Y, Li X-Y, Keller ET, Yang J, Cho J-S, Feinberg TY, Weiss SJ. 2020. Osteoclast-mediated bone resorption is controlled by a compensatory network of secreted and membrane-tethered metalloproteinases. *Sci Transl Med* **12**. doi:10.1126/scitranslmed.aaw6143

Zorova LD, Popkov VA, Plotnikov EY, Silachev DN, Pevzner IB, Jankauskas SS, Babenko VA, Zorov SD, Balakireva AV, Juhaszova M, Sollott SJ, Zorov DB. 2018. Mitochondrial membrane potential. *Anal Biochem* **552**:50–59. doi:10.1016/j.ab.2017.07.009

Supplementary Information

Supplementary Materials and Methods

TRAP activity staining

Sections were rehydrated with ddH_2O and then processed for TRAP activity staining using a commercial kit (Takara, MK300), according to manufacturer's instruction. Briefly, sections were fixed for 5 min using the fixation solution from the kit, washed 3 times with sterile distilled water and then incubated for 45 min at 37 °C with the ACP substrate containing sodium tartrate. Sections were then washed 3 times with sterile distilled water, counterstained using Mayer's hematoxylin (Sigma Aldrich, MHS) for 1 min, washed again 3 times with tap water before mounting using glycerol. Tissue sections were imaged using a Zeiss Axioscan Z1 slide scanner and analyzed through the Zen software. The number of TRAP positive multinuclear cells normalized per bone tissue surface was reported.

Supplementary Figures and Legends

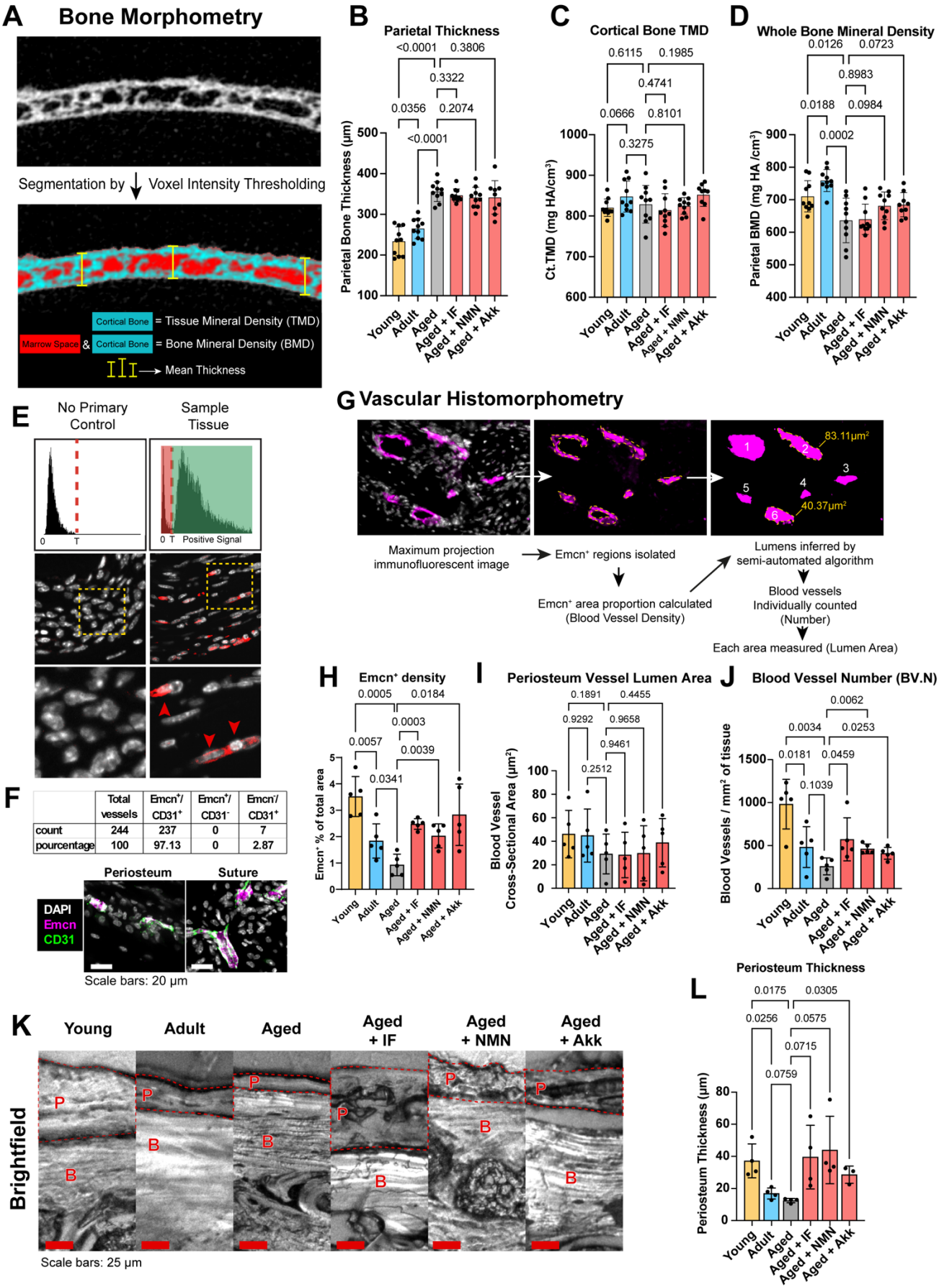

	Total vessels	Emcn⁺/ CD31⁺	Emcn⁺/ CD31⁻	Emcn⁻/ CD31⁺
count	244	237	0	7
pourcentage	100	97.13	0	2.87

Supplementary Figure 1

(**A**) Methodology for segmentation of micro-computed tomography (microCT) images for calculation of bone morphometry metrics: (**B)** Parietal Thickness (**C**) Cortical Tissue Mineral Density (Ct.TMD), (**D**) Parietal Whole Bone Mineral Density (BMD). Statistical analysis: Welch's tests, n = 10 mice per condition, except Aged + Akk (n = 9). (**E**) The method for quantifying immunofluorescence-positive (red) cells. The maximum pixel intensity is determined in control tissues lacking primary antibody (no primary control). This value is used to threshold the stained sample tissue, with the remaining signal distinguishing positive cells (red arrows). DAPI (grey) is also shown for reference of cellular locations. (**F**) Number and percentage of blood vessels positive for Emcn and/or CD31 with representative images in the periosteum and suture mesenchyme. (**G**) Methodology for segmentation of Endomucin (Emcn) immunofluorescent staining in fixed tissue sections, for calculation of vascular histomorphometry metrics: (**H**) $Emcn^+$ staining density (proportion of total tissue area). Data are shown previously in main Figures 1, 3, and 5, and are reproduced here for reference, (**I**) Mean lumen area per blood vessel, (**J**) Number of blood vessels per area tissue (BV.N). Statistical analysis: Welch's tests, n = 5 mice per condition.

(**K**) Representative brightfield images of unstained tissue sections highlighting the overlying periosteum (red P, red dashed line) and parietal bone (red B). (**L**) Mean periosteal thickness. Statistical analysis: Welch's tests, n = 4 mice per condition, except Aged + Akk (n = 3).

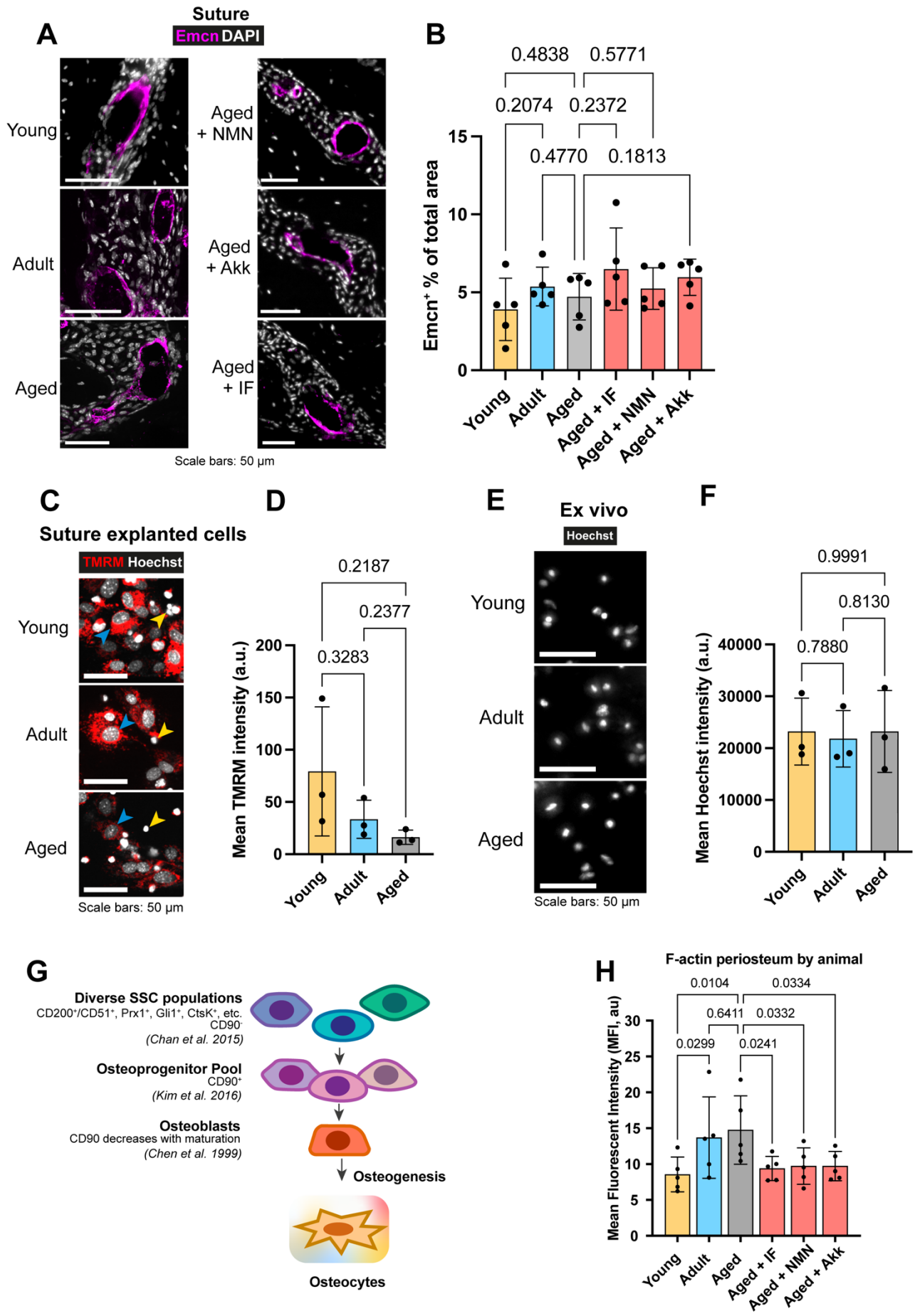
A
Suture
Emcn DAPI
Young
Adult
Aged
Aged + NMN
Aged + Akk
Aged + IF
Scale bars: 50 µm
B
0.4838
0.5771
0.2074
0.2372
0.4770
0.1813
Emcn+ % of total area
Young
Adult
Aged
Aged + IF
Aged + NMN
Aged + Akk
C
Suture explanted cells
TMRM Hoechst
Young
Adult
Aged
Scale bars: 50 µm
D
0.2187
0.2377
0.3283
Mean TMRM intensity (a.u.)
Young
Adult
Aged
E
Ex vivo
Hoechst
Young
Adult
Aged
Scale bars: 50 µm
F
0.9991
0.8130
0.7880
Mean Hoechst intensity (a.u.)
Young
Adult
Aged
G
Diverse SSC populations
CD200+/CD51+, Prx1+, Gli1+, CtsK+, etc.
CD90-
(Chan et al. 2015)
Osteoprogenitor Pool
CD90+
(Kim et al. 2016)
Osteoblasts
CD90 decreases with maturation
(Chen et al. 1999)
Osteogenesis
Osteocytes
H
F-actin periosteum by animal
0.0104
0.0334
0.6411
0.0332
0.0299
0.0241
Mean Fluorescent Intensity (MFI, au)
Young
Adult
Aged
Aged + IF
Aged + NMN
Aged + Akk

Supplementary Figure 2

(**A**) representative immunofluorescence staining of Emcn (magenta) and DAPI (grey) and (**B**) mean cross sectional area of Endomucin (Emcn)-positive vascular cells in mouse sutures. Statistical analysis: Welch's tests in n = 5 mice. (**C**) Representative images and (**D**) mean intensity of live TMRM staining (red) and Hoechst (grey) in adherent cells allowed to explant from suture mesenchyme tissue for 24 hours *in vitro*. Remaining mesenchyme tissue was removed prior to staining. Statistical analysis: Welch's tests in tissue from n = 3 mice per condition. (**E**) Representative images and (**F**) mean intensity of live Hoechst staining (grey) from the TMRM experiment in **Fig. 1i-j**. Statistical analysis: Welch's tests in tissue from n = 3 mice per condition. (**G**) Schematic demonstrating the hierarchy and selected markers of Skeletal Stem Cells (SSCs), leading to the $CD90^+$ cell pool, which ultimately differentiates into osteoblasts and osteocytes during osteogenesis. (**H**) Mean Phalloidin-488 staining intensity for F-actin in the periosteum. Statistical analysis: Welch's tests in n = 5 mice.

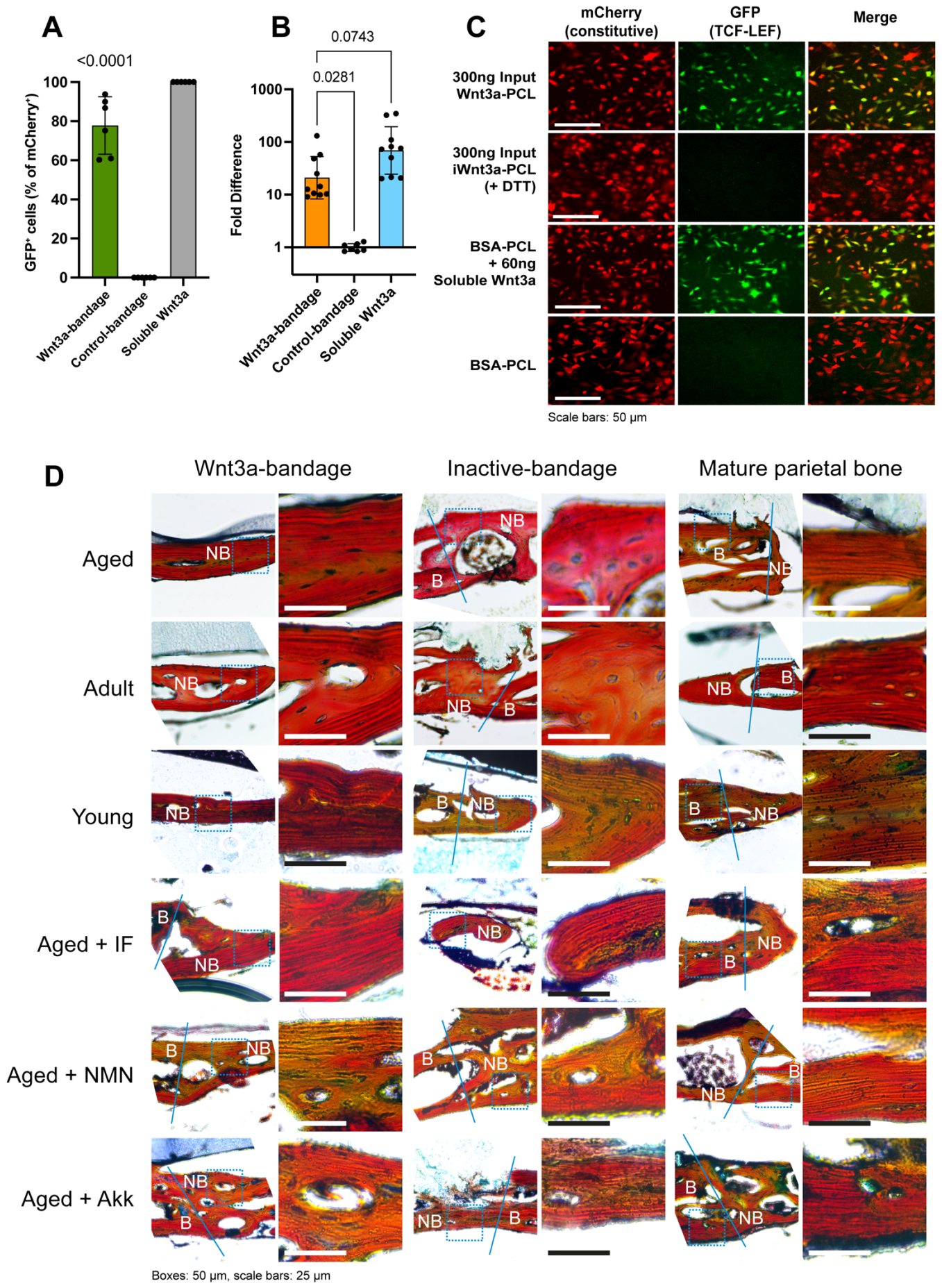
A
<0.0001
GFP⁺ cells (% of mCherry⁺)
100
80
60
40
20
0
Wnt3a-bandage
Control-bandage
Soluble Wnt3a
B
0.0743
0.0281
Fold Difference
1000
100
10
1
Wnt3a-bandage
Control-bandage
Soluble Wnt3a
C
mCherry (constitutive)
GFP (TCF-LEF)
Merge
300ng Input Wnt3a-PCL
300ng Input iWnt3a-PCL (+ DTT)
BSA-PCL + 60ng Soluble Wnt3a
BSA-PCL
Scale bars: 50 µm
D
Wnt3a-bandage
Inactive-bandage
Mature parietal bone
Aged
Adult
Young
Aged + IF
Aged + NMN
Aged + Akk
NB
B
Boxes: 50 µm, scale bars: 25 µm

Supplementary Figure 3

(**A**) Characterization of Wnt3a-bandage activation of the Wnt/β-catenin pathway with Comma-D Beta cells *in vitro*. Presented as the proportion of GFP^+ cells, normalized to the proportion of GFP^+ responsive to soluble Wnt3a. Statistical analysis: two-tailed one-sample t test against the inactive control-bandage (mean = 0); n = 6 for each condition. (**B**) Characterization of Wnt3a-bandage activation of the Wnt/β-catenin pathway with LS/L cells *in vitro*. Presented as fold change of Luciferase signal over control-bandage. Statistical analysis: Welch's test, n = 10 for each Wnt3a-bandage and Soluble Wnt3a, n = 7 for Control-bandage.

(**C**) Representative images for Comma-D Beta cells quantified in (**A**). mCherry (red) is constitutively expressed, GFP (green) is expressed during Wnt/β-catenin pathway activation. Wnt3a is treated with DTT, resulting in complete chemical inactivation (iWnt3a). Bovine Serum Albumin (BSA) is used as an additional negative control. Polycaprolactone (PCL) is the polymeric material that Wnt3a is bound to during Wnt3abandage manufacture. (**D**) Representative Movat's pentachrome staining of bone tissues showing the lamellar/striated structures. Blue line designates the drilled defect edge, thereby separating original intact bone B from new bone NB. The dashed blue box shows the enlarged region.

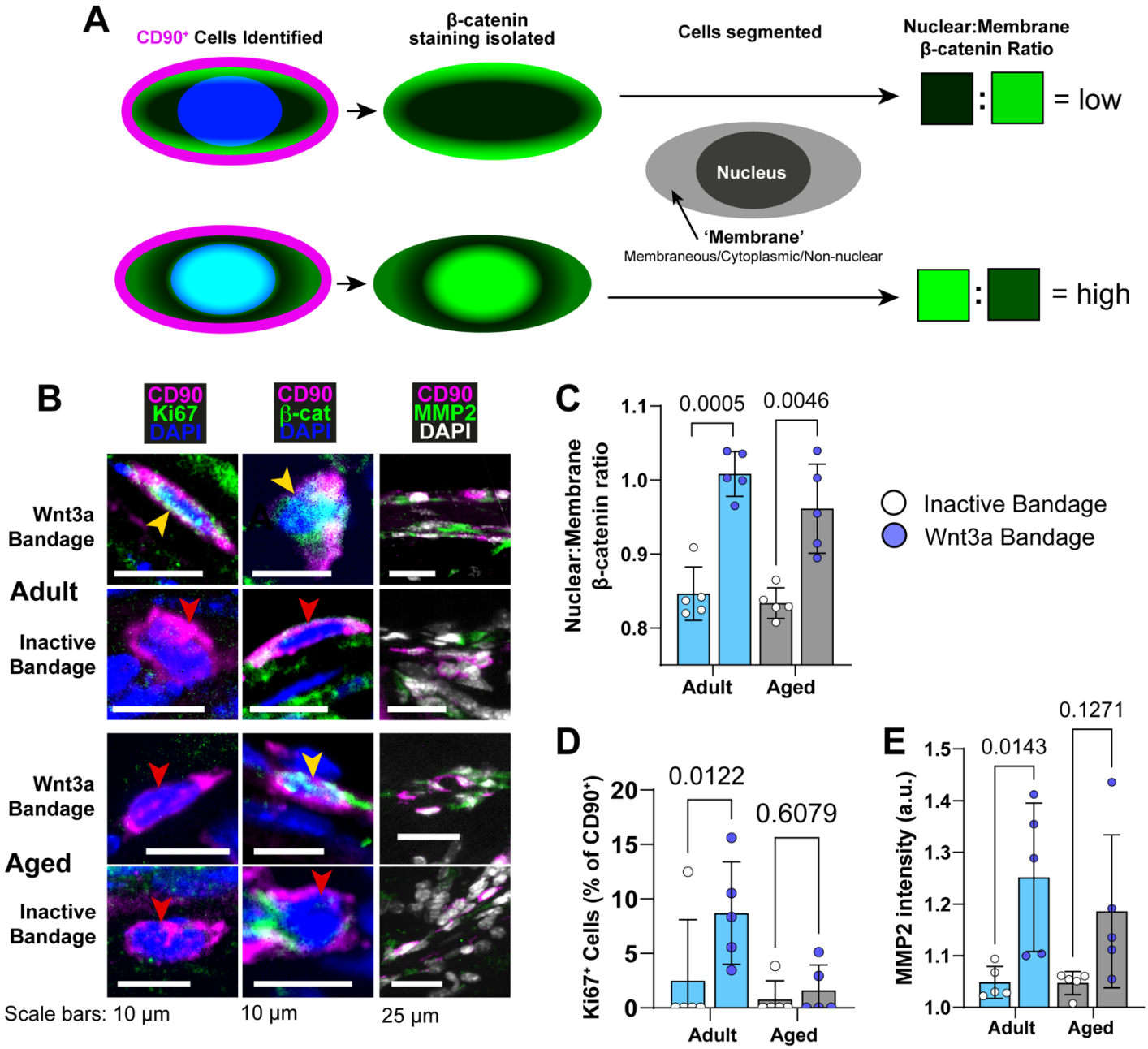

Supplementary Figure 4

(**A**) Schematic depicting the methodology for measuring the ratio of Nuclear:Membrane β-catenin in single CD90$^+$ cells. (**B**) Representative images depicting CD90 (magenta), DAPI (grey/blue as indicated by column), and functional markers (green) as indicated by column). Yellow arrows indicate marker-high/positive cells; red arrows indicate marker-low/negative cells. (**C**) Proportion of CD90$^+$ cells that are Ki67$^+$ by age. Statistical testing: paired, two-tailed t tests in n = 5 mice per condition. (**D**) Ratio of Nuclear:Membrane β-catenin staining in CD90$^+$ cells by age. Statistical testing: ratio paired, two-tailed t tests in n = 5 mice per condition. (**E**) Normalized intensity staining for MMP2 in CD90$^+$ cells by age. Statistical testing: ratio paired, two tailed t tests in n = 5 mice per condition. For all plots (**C-E**), Wnt3a-bandage (dark blue points), inactive bandage (white points), Adult (blue), Aged (grey).

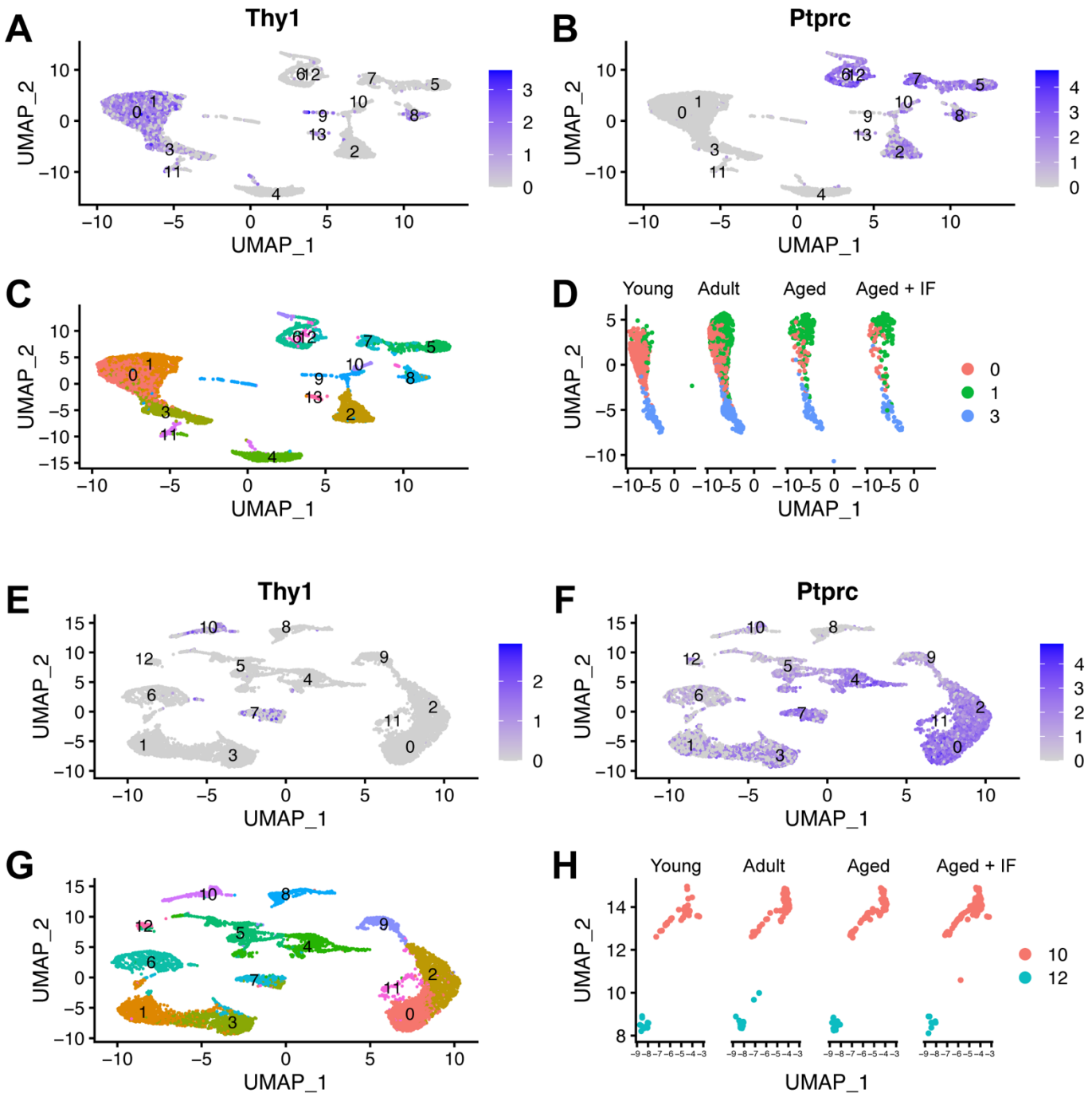

Supplementary Figure 5

UMAP-coordinate plot of Thy1 (CD90, **A**) and Ptprc (CD45, **B**) expression in clusters of cells within the periosteum. (**C**) Periosteum cell populations (clusters) as identified through unbiased clustering (**D**) The $CD90^{+}/CD45^{-}$ clusters of interest (0, 1, 3), separated by mouse condition. UMAP-coordinate plot of Thy1 (CD90, **E**) and Ptprc (CD45, **F**) expression in clusters of cells within the suture. (**G**) Suture mesenchyme cell populations (clusters) as identified through unbiased clustering (**H**) The $CD90^{+}/CD45^{-}$ cluster of interest (10), and also the small endothelial cluster (12), separated by mouse condition.

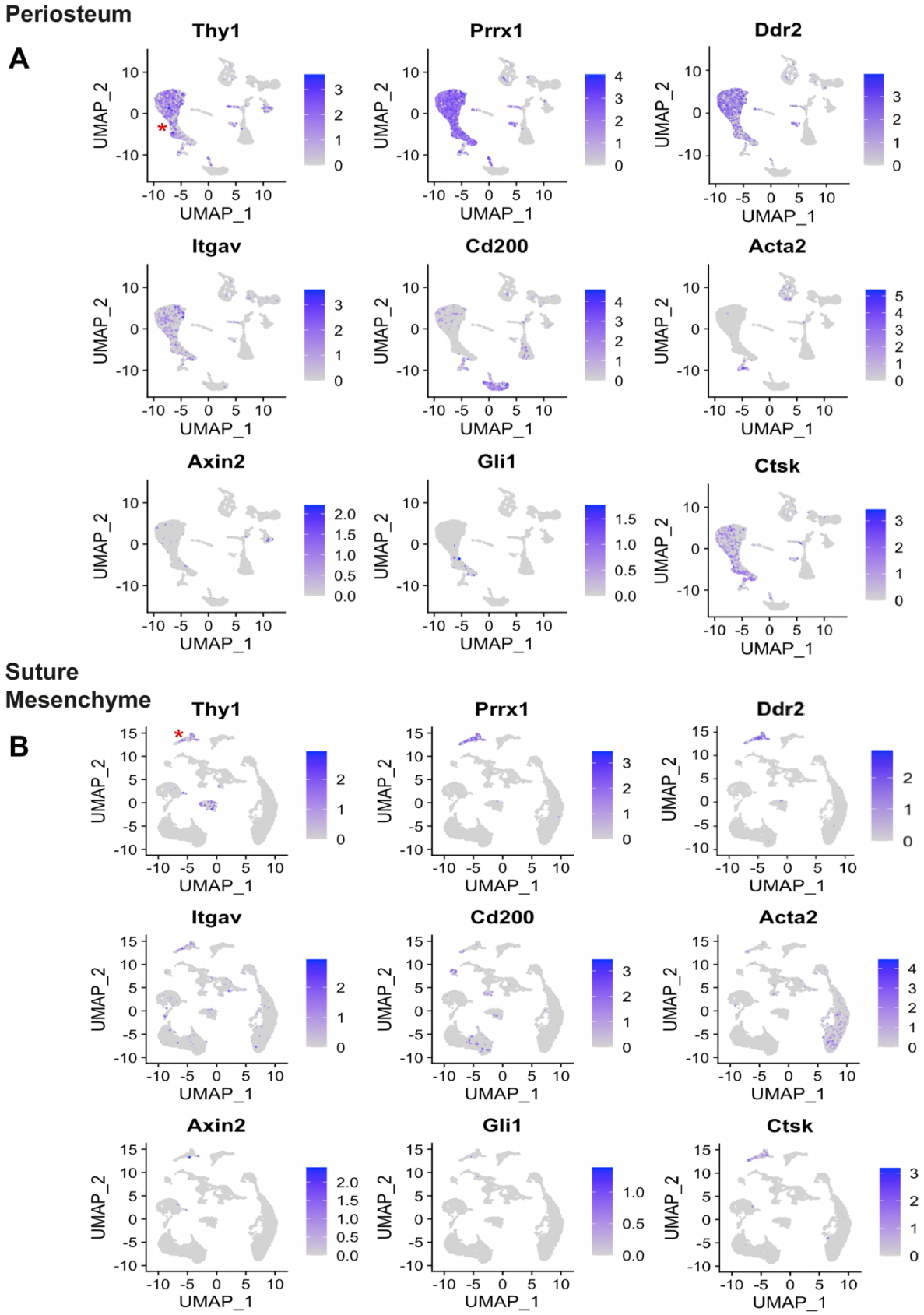
Periosteum
A
Thy1
Prrx1
Ddr2
Itgav
Cd200
Acta2
Axin2
Gli1
Ctsk
UMAP_1
UMAP_2
Suture Mesenchyme
B
Thy1
Prrx1
Ddr2
Itgav
Cd200
Acta2
Axin2
Gli1
Ctsk
UMAP_1
UMAP_2

Supplementary Figure 6

UMAP-coordinate plot of the entire cell populations from Periosteum (**A**) and Suture Mesenchyme (**B**). Expression of SSC markers (purple) highlights clusters of transcriptomically-similar cells. The red asterisk is adjacent to the group of cells referred to as the $CD90^{+}$ (Thy1) population, which is also $CD45^{-}$ ($Ptprc^{-}$) (**Supplementary Fig. 5a-h**). Prrx1 (Prx1), Ddr2, Itgav (CD51), Cd200 (CD200), Acta2(a-SMA), Axin2, Gli1 and Ctsk (Cathepsin K) are shown.

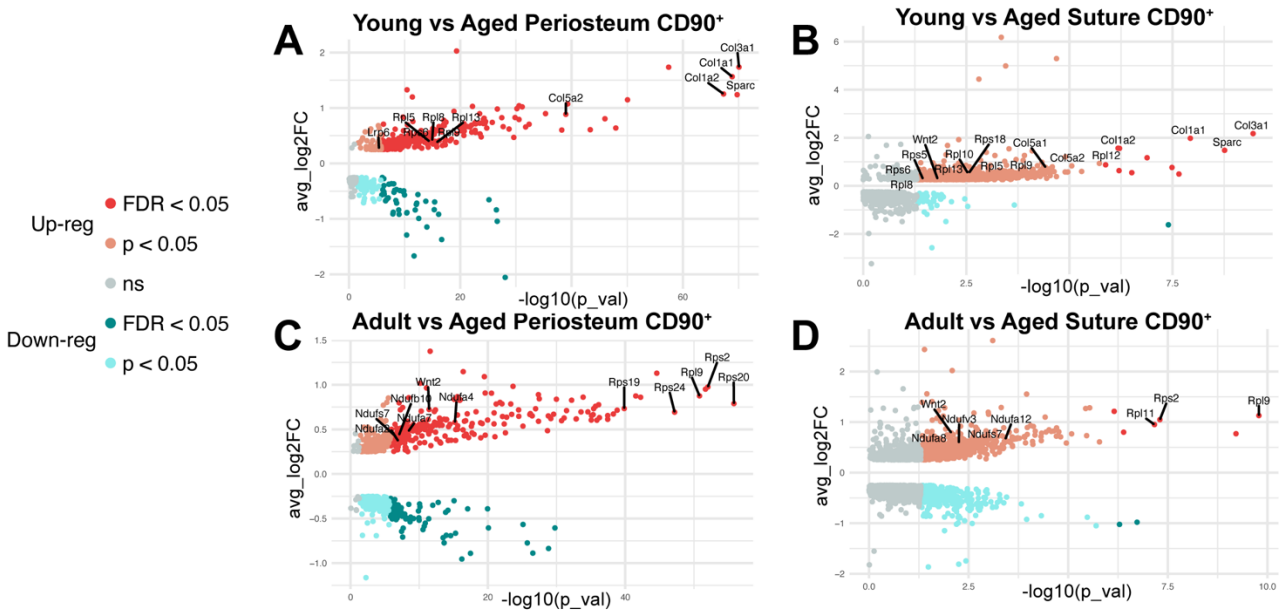
A
Young vs Aged Periosteum CD90+
B
Young vs Aged Suture CD90+
C
Adult vs Aged Periosteum CD90+
D
Adult vs Aged Suture CD90+
avg_log2FC
-log10(p_val)
Up-reg
FDR < 0.05
p < 0.05
ns
Down-reg
FDR < 0.05
p < 0.05

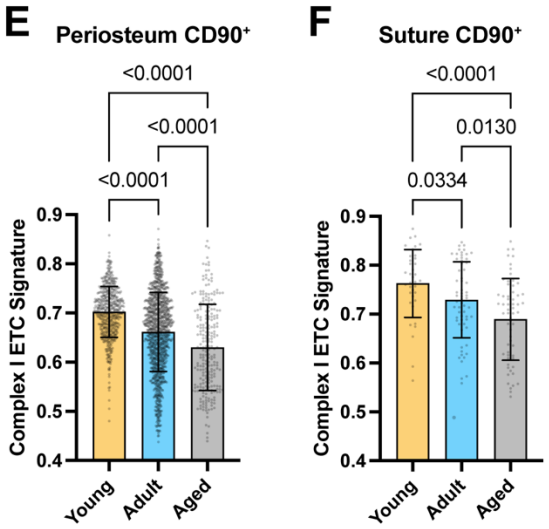
E
Periosteum CD90+
F
Suture CD90+
<0.0001
<0.0001
<0.0001
<0.0001
0.0130
0.0334
Complex I ETC Signature
Young
Adult
Aged

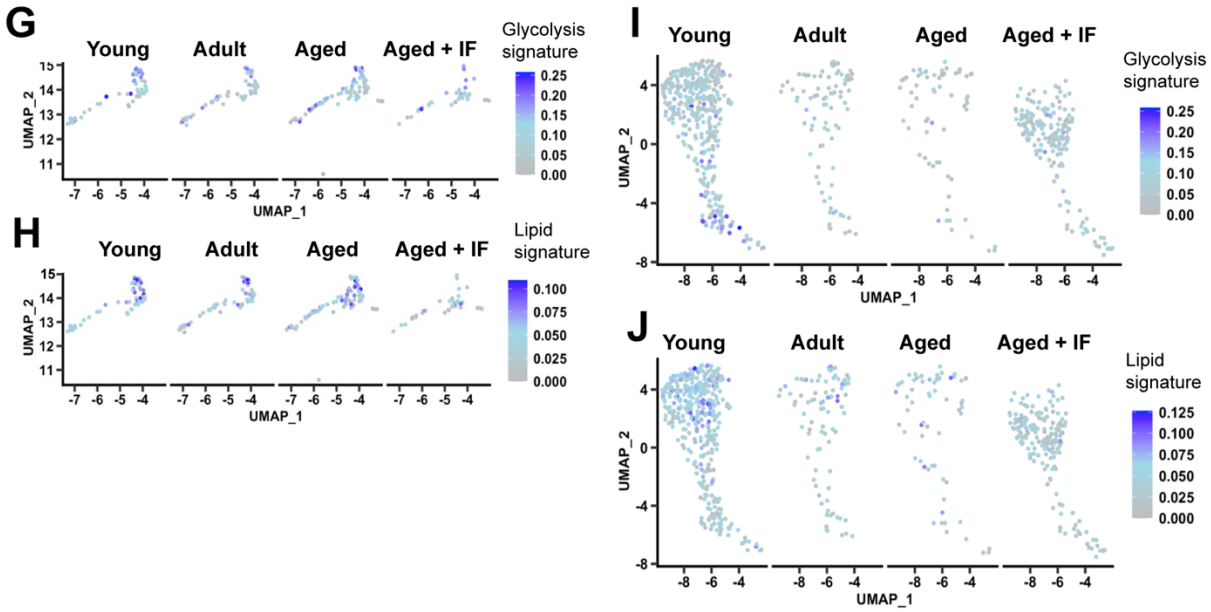
G
H
I
J
Young
Adult
Aged
Aged + IF
Glycolysis signature
Lipid signature
UMAP_1
UMAP_2

Supplementary Figure 7

(**A**) Volcano plot showing differentially-expressed genes in the comparison of the $CD90^+$ population in Young vs Aged periosteum; (**B**) Young vs Aged suture; (**C**) Adult vs Aged periosteum and (**D**) Adult vs Aged Suture. Statistical analysis: Wilcoxon Rank Sum test via the FindMarkers function in the Seurat R package. Upregulated (pink: $p < 0.05$; red: FDR-adjusted $p < 0.05$), downregulated (cyan: $p < 0.05$; teal: FDR-adjusted $p < 0.05$), and non-significant (ns) genes are displayed on axes of log fold expression (y, avg_log2FC) against p transformed as its negative log value. (**E**) UCell Signature Scoring of transcript expression of genes relating to Complex I electron transport chain (GO-term: 0005747) in the CD90+ clusters of the periosteum and (**F**) suture. Statistical analysis: Uncorrected Dunn's tests; $n \geq 242$ cells in periosteum per age group, $n \geq 39$ cells in suture per age group. (**G-J**) UMAP-coordinate plot of the $CD90^+$ cells in the periosteum (**G, H**) and suture mesenchyme (**I, J**) for the glycolysis and lipid UCell Signature scoring.

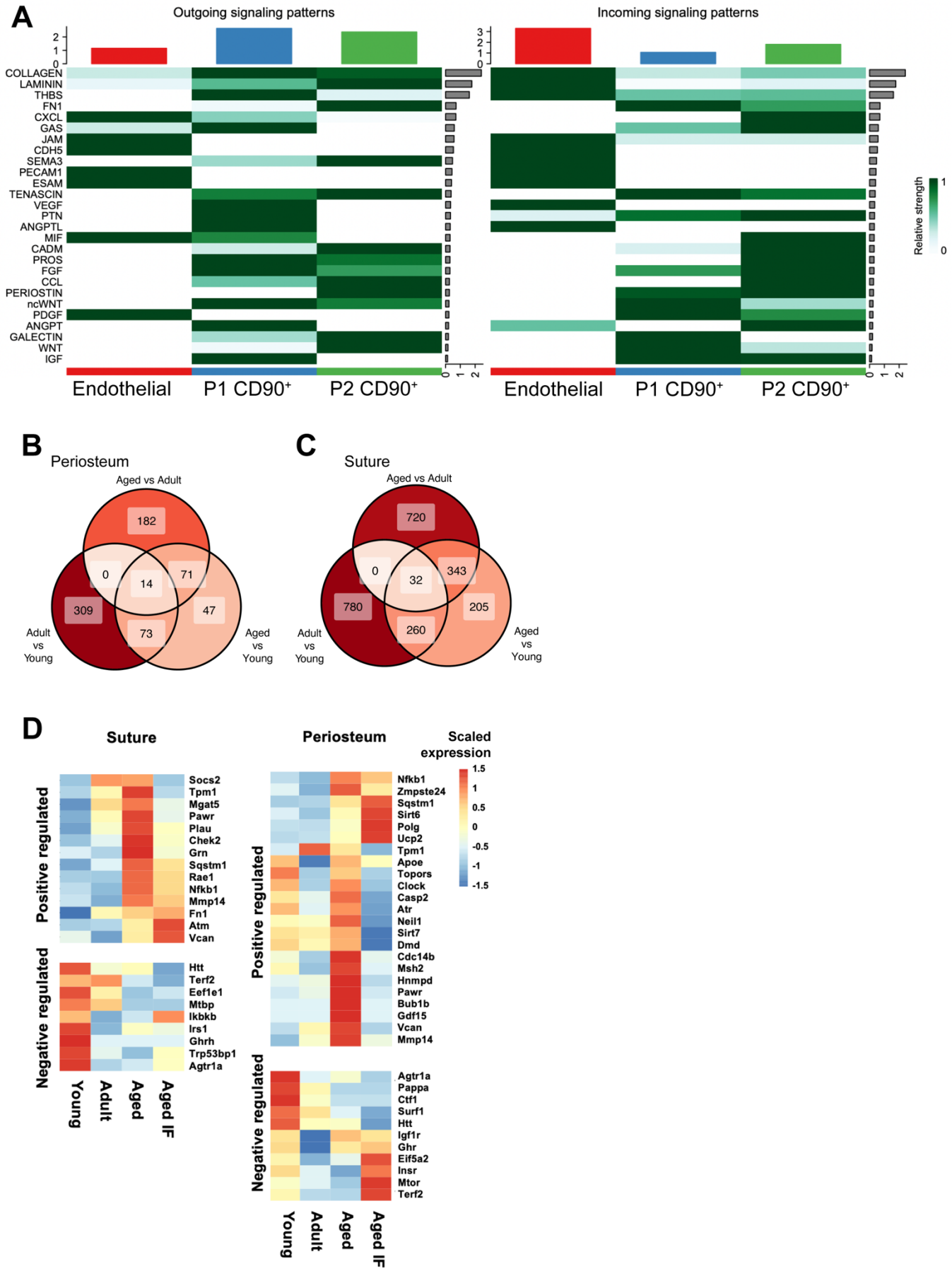
A
Outgoing signaling patterns
Incoming signaling patterns
COLLAGEN
LAMININ
THBS
FN1
CXCL
GAS
JAM
CDH5
SEMA3
PECAM1
ESAM
TENASCIN
VEGF
PTN
ANGPTL
MIF
CADM
PROS
FGF
CCL
PERIOSTIN
ncWNT
PDGF
ANGPT
GALECTIN
WNT
IGF
Endothelial
P1 CD90+
P2 CD90+
Relative strength
B
Periosteum
Aged vs Adult
182
0
14
71
309
47
73
Adult vs Young
Aged vs Young
C
Suture
Aged vs Adult
720
0
32
343
780
205
260
Adult vs Young
Aged vs Young
D
Suture
Periosteum
Scaled expression
Positive regulated
Negative regulated
Socs2
Tpm1
Mgat5
Pawr
Plau
Chek2
Grn
Sqstm1
Rae1
Nfkb1
Mmp14
Fn1
Atm
Vcan
Htt
Terf2
Eef1e1
Mtbp
Ikbkb
Irs1
Ghrh
Trp53bp1
Agtr1a
Nfkb1
Zmpste24
Sqstm1
Sirt6
Polg
Ucp2
Tpm1
Apoe
Topors
Clock
Casp2
Atr
Neil1
Sirt7
Dmd
Cdc14b
Msh2
Hnmpd
Pawr
Bub1b
Gdf15
Vcan
Mmp14
Agtr1a
Pappa
Ctf1
Surf1
Htt
Igf1r
Ghr
Eif5a2
Insr
Mtor
Terf2
Young
Adult
Aged
Aged IF

112 **Supplementary Figure 8**
113 (**A**) CellChat analysis of the relative inferred levels of outgoing and incoming signaling between subsets of
114 periosteal cells, grouped into pathways. P2 contains the Igf1^{high} and Igf1^{low} populations. Green color scale
115 shows relative intensity in outgoing (left) and incoming (right) inferred signaling patterns for pathways shown
116 at the left edge. Red/blue/green boxes at the top show the relative sum of all pathways. (**B**) Three-way Venn
117 diagrams showing the overlap of statistically-significant positively-upregulated differentially-expressed genes
118 ($p < 0.05$) in comparisons between the CD90^{+} clusters in the periosteum and (**C**) suture of Young, Adult, and
119 Aged mice. Color of shading and label shows number of genes shared. The central section shows the number
120 of genes conserved throughout all comparisons. (**D**) Heatmaps of gene expression in CD90^{+} cells from suture
121 and periosteum mesenchyme of young, adult, aged and aged + IF mice. Scaled expression of genes positively
122 regulated and negatively regulated in senescent cells.
123

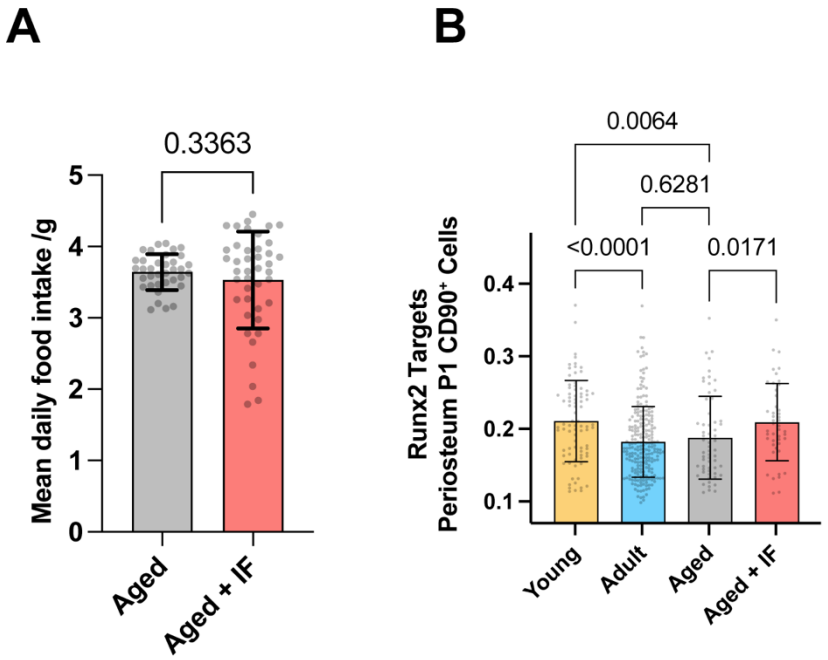

Supplementary Figure 9

(**A**) The mean daily food intake of Aged mice on ad libitum (AL) diet vs intermittent fasting (IF), averaged over the course of measurements of n ≥ 10 mice. Statistical analysis: Welch's t-test of n ≥ 36 total food measurements taken. (**B**) UCell Signature Scoring of transcript expression of transcriptional targets of Runx2 in the P1 CD90$^+$ cluster subset of the periosteum. Statistical analysis: Uncorrected Dunn's tests; n ≥ 46 cells per condition.

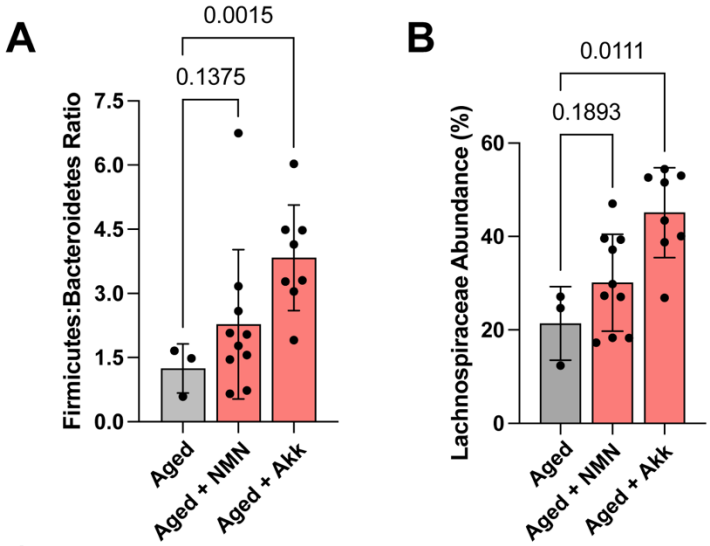

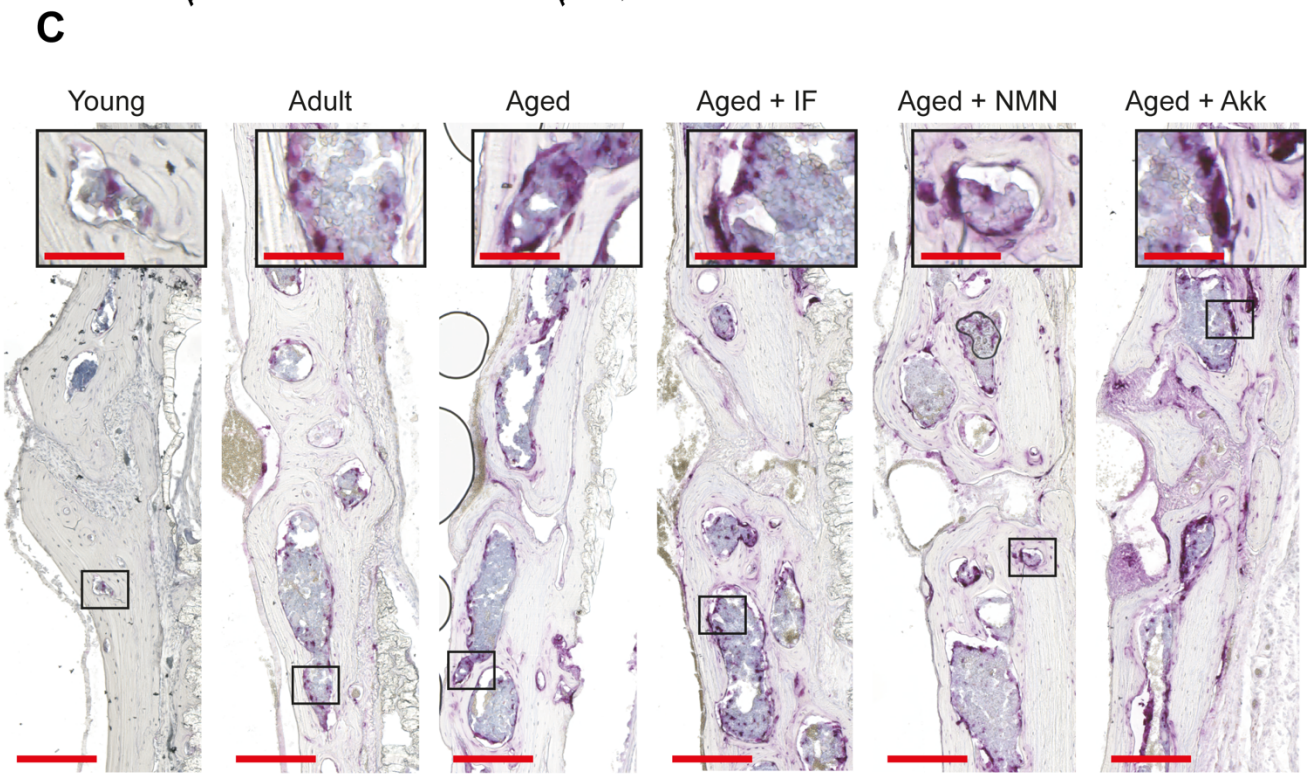

Scale main image: 200 µm. Scale insert: 50 µm.

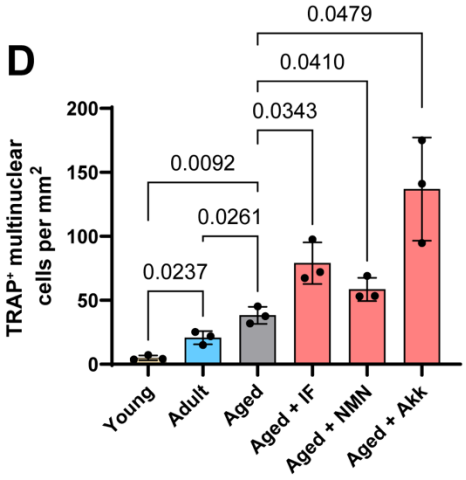

134

135 **Supplementary Figure 10**
136 (**A**) The relative abundance of Firmicutes to Bacterioides bacteria and (**B**) Lachnospiraceae bacteria, as
137 measured by 16S metagenomic profiling. Statistical analysis: Welch's tests on n = 3 (Aged), n = 10 (Aged +
138 NMN), n = 8 (Aged + Akk). (**C**) Representative calvarial TRAP activity staining images. (**D**) Number of TRAP
139 positive multinuclear cells normalized per bone tissue surface. Statistical analysis: Welch's tests n = 3 mice
140 per group. The black box shows the enlarged region.
141

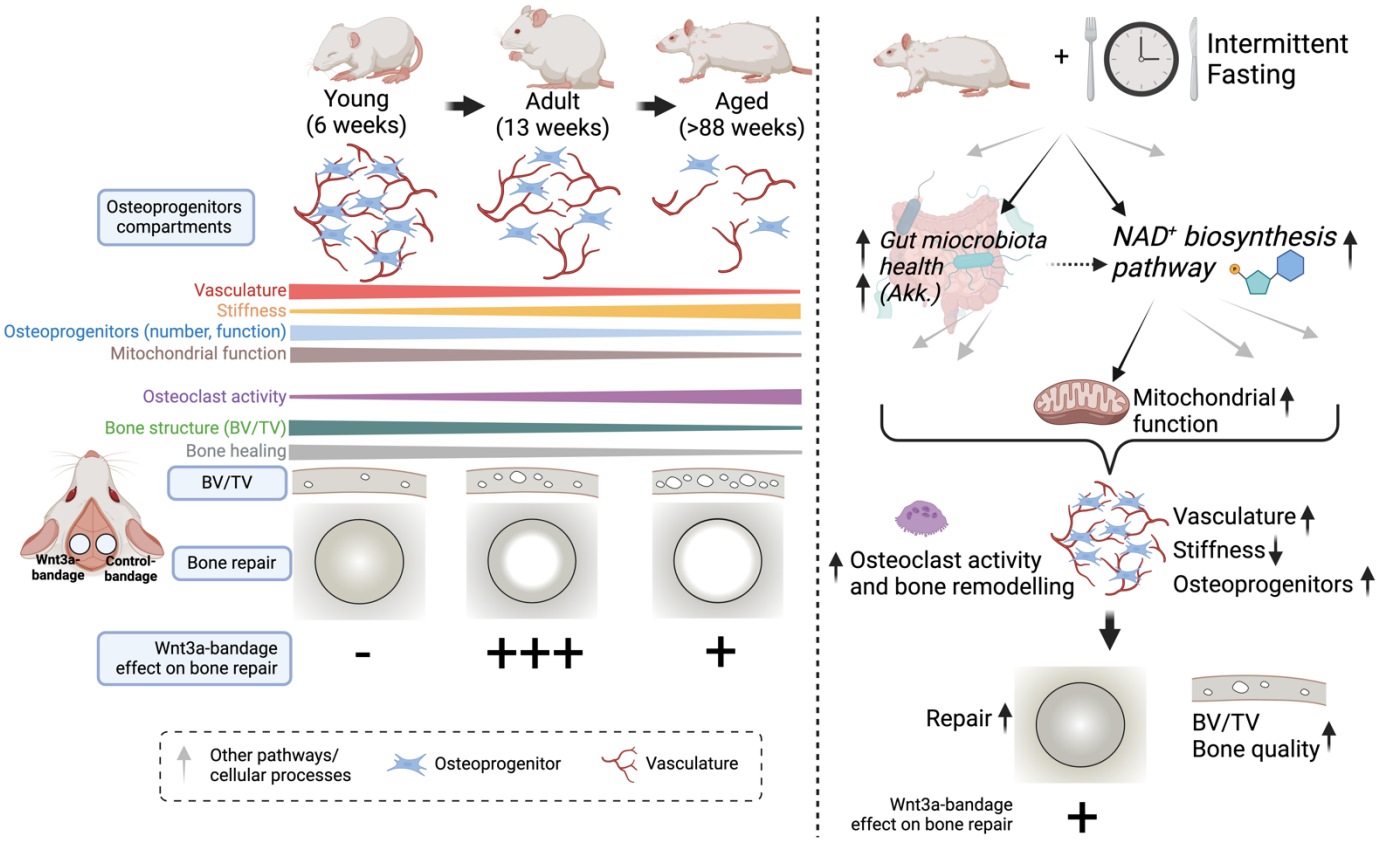

Supplementary Figure 11

Schematic that recapitulates the mains findings of the study.

		Inactive						Active					
		Young	Adult	Aged	Aged + IF	Aged + NMN	Aged + Akk	Young	Adult	Aged	Aged + IF	Aged + NMN	Aged + Akk
Inactive	Young												
	Adult	*											
	Aged	****	*										
	Aged + IF	*	ns	****									
	Aged + NMN	*	ns	****	ns								
	Aged + Akk	***	ns	****	*	ns							
Active	Young	ns	*	****	*	*	***						
	Adult	ns	*	****	*	*	***	ns					
	Aged	****	*	*	***	**	*	****	****				
	Aged + IF	ns	ns	****	ns	ns	**	ns	ns	***			
	Aged + NMN	ns	ns	****	ns	ns	**	ns	ns	***	ns		
	Aged + Akk	ns	ns	****	ns	ns	**	ns	ns	****	ns	ns	

Supplementary Table 1: Statistical analysis of Fig. 1o. Stars and symbols indicate statistical significance calculated by one-way ANOVA followed by unpaired t-test with Welch's correction, or by ratio paired t-test (non-significant, $p>0.05$) when comparing inactive vs active within the same group (e.g. Young inactive vs Young active). Ns: non significant, *$p<0.05$, **$p<0.01$, ***$p<0.001$, ****$p<0.0001$.

Comparison	Tissue	Number of genes significantly impacted	Effect	Gene or pathway impacted (GO term)	Figure
CD90^{+} cells Young vs Aged	Periosteum	38	upregulated in Young	Cytosolic ribosome (GO: 0022626), FDR: 1.0E-30, FE: 14.2	Supplementary Fig. 7a
		59		Collagen-containing extracellular matrix (GO: 0062023), FDR: 2.0E-29, FE: 6.8	Supplementary Fig. 7a
	Suture mesenchyme	879		Structural constituent of ribosome (GO: 0003735), FDR: 2.45E-3, FE: 8.15	Supplementary Fig. 7b
				Extracellular matrix structural constituent (GO: 0005201), FDR: 7.65E-08, FE: 4.58	Supplementary Fig. 7b
CD90+ cells Adult vs Aged	Periosteum	1	down regulated in Aged	Wnt2 transcripts downregulated (FDR adjusted p value (q) = 1.16E-07)	Supplementary Fig. 7c
CD90+ cells Young vs Adult	Periosteum	1	down regulated in Adult	Wnt2 transcripts downregulated (FDR adjusted p value (q) = 1.01E-09	RNA-seq Table 5
CD90+ cells Young vs Aged	Suture mesenchyme	1	down regulated in Aged	Wnt2 transcripts downregulated (non-adjusted p value (p) = 1.58E-02)	Supplementary Fig. 7b
CD90+ cells Adult vs Aged	Suture mesenchyme	1	down regulated in Aged	Wnt2 transcripts downregulated (p = 8.58E-03)	Supplementary Fig. 7d
CD90+ cells Young vs Adult	Periosteum	1	down regulated in Adult	Lrp6 declined Adult vs Young (p = 4.14E-18)	Supplementary Table 5
CD90+ cells Young vs Aged	Periosteum	1	down regulated in Aged	Lrp6 declined Aged vs Young (p = 4.01E-06)	Supplementary Fig. 7a
CD90+ cells Adult vs Aged	Periosteum	637	upregulated in Adult	NADH dehydrogenase complex assembly (GO:0010257), FDR: 9.9E-16, FE: 12.8	(Supplementary Fig. 7c)
				NADH dehydrogenase (ubiquinone) activity (GO: 0008137), FDR: 7.1E-09, FE: 14.4	(Supplementary Fig. 7c)
				Oxidative phosphorylation (GO: 0006119), FDR: 7.2E-20, FE: 9.6	(Supplementary Fig. 7c)
	Suture mesenchyme	610		Mitochondrial ATP synthesis coupled proton transport (GO:0042776), FDR: 2.7E-09, FE: 9.3	Supplementary Fig. 7d
				Oxidative phosphorylation (GO: 0006119), FDR: 5.6E-16, FE: 8.7	Supplementary Fig. 7d
CD90+ cells Adult vs Aged	Periosteum		downregulated in Aged	Complex I gene (GO: 0005747) (p < 0.0001)	Supplementary Fig. 9b-c
CD90+ cells Young vs Adult	Periosteum		downregulated in Adult	Complex I gene (GO: 0005747) (p < 0.0001)	Supplementary Fig. 9b-c
CD90+ cells Igf1 low vs Igf1 high	Periosteum	85	upregulation in Igf1 low	Cell motility (GO: 0048870), FDR: 2.58E-08, FE: 4.40	Fig. 2c
		204	upregulation in Igf1 high	Collagen-containing extracellular matrix (GO: 0062023), FDR: 6.18E-38, FE: 14.41	Fig. 2c
				Oxidative phosphorylation (KEGG: mmu00190, FDR: 2.08E-03, FE: 5.97	Fig. 2c
				Respiratory chain complex (GO: 0098803), FDR: 1.43E-03, FE: 8.61	Fig. 2c
CD90+ cells proliferating vs non proliferating	Suture mesenchyme	855	upregulation in proliferating cells	Mitotic cell cycle (GO: 0000278), FDR: 1.0E-47, FE: 4.5	Fig. 2d-e
				ATP-dependent activity (GO: 0140657), FDR: 4.8E-08, FE: 2.6	Fig. 2d-e
CD90+ cells Aged vs Aged IF	Periosteum	98	upregulation in Aged IF	Response to cytokine (GO: 0034097), FDR: 2.91E-08, FE: 5.63	Fig. 4a
	Suture mesenchyme	297		Mitotic cell cycle (GO: 0000278), FDR: 1.2E-05, FE: 3.2	Fig. 4b
				Protein phosphorylation (GO: 0006468), FDR: 1.7E-05, FE: 2.4	Fig. 4b
	Periosteum	3		Dbp, Hlf, and Tef (each q < 0.05)	Supplementary Fig. 7e-f
	Suture mesenchyme	1		Dbp (p < 0.05)	Supplementary Fig. 7e-f
	Suture mesenchyme	>5		Genes under circadian control (e.g., Sirt1, Kat2b, Csnk1e, Ezh2, Fbxw11, Ucp2; all p < 0.05)	Fig. 4b
	Suture mesenchyme	7		transcriptional targets of Clock/Per2/Arntl (FDR: 6.42E-04, 2.95E-03, 1.23E-02 respectively)	RNA-seq Table 12

Supplementary Table 2: RNAseq comparison data summary